A MECHANICS BASED ANALYTICAL MODEL OF VITREOUS MOTION AND VITREOUS DETACHMENT IN THE HUMAN EYE WHEN SUBJECTED TO SACCADIC MOVEMENT

by

MICHAEL J. PAVLOU

A dissertation submitted to the

School of Graduate Studies

Rutgers, The State University of New Jersey

in partial fulfillment of the requirements

for the degree of

Doctor of Philosophy

Graduate Program in Mechanical & Aerospace Engineering

Written under the direction of

Prof. William J. Bottega

and approved by

____

____

____

____

New Brunswick, New Jersey

May, 2018

ABSTRACT OF THE DISSERTATION

A Mechanics Based Analytical Model of Vitreous Motion and Vitreous Detachment in the Human Eye When Subjected to Saccadic Movement

by MICHAEL J. PAVLOU

Dissertation Director:

Prof. William J. Bottega

In the human eye, the detachment behavior of the vitreous cortex from the sensory retina is clinically significant as this pathology is highly correlated with rhegmatogenous retinal detachment, a serious eye condition that can result in vision loss. A mechanics based mathematical model for vitreo-retinal detachment in the human eye when subjected to saccadic eye motion is presented in this dissertation. The problem is formulated as a two-dimensional propagating boundary value viscoelasticity problem in the calculus of variations. This formulation yields the governing equations of the vitreous body, boundary conditions, matching conditions and a transversality condition which, in turn, yields the detachment criterion during a saccade.

The first part of the dissertation studies a constrained two-dimensional model where only the dominant motion of the vitreous is considered. Closed form analytical solutions of the coupled set of partial differential equations are obtained via modal analysis of a vibrating two-dimensional continuum with non-periodic loading. Results of numerical simulations are presented, ultimately revealing the evolution of the detachment of the vitreo-retinal interface.

In the second part of the dissertation, fully two-dimensional motion of the vitreous is considered. A semi-analytical solution is obtained via the Rayleigh-Ritz method in combination with modal analysis. Results are compared to the constrained two-dimensional model, as well as to clinically observed data and previously published experimental and numerical studies. The material properties of the human vitreous are both difficult to study, and change significantly with age and other factors. The effects of these properties on the motion of the vitreous and the detachment behavior of the vitreo-retinal interface are studied. The results of the present study indicate that if a saccade is large enough to cause further detachment of the vitreous from the retina, then the detachment will progress until it reaches a point of abnormal vitreo-retinal adhesion.

Acknowledgements

I have been a student at Rutgers University for nearly eleven years, where I started as a freshman in the School of Engineering in September of 2007. I have learned so much in that time from some of the brightest and kindest people I have ever met. I would like to express my sincere thanks and appreciation for all of these who have helped make the writing of this dissertation a possibility. I would first like to thank my research advisor, Dr. William J. Bottega. He has helped with every step of the research along the way, and his guidance has helped me to grow as an individual. Many long discussions about the subject in his office have led to the biggest breakthroughs along the way. I also wish to thank Dr. Haym Benaroya, Dr. Haim Baruh, and Dr. Howard Fine for their assistance, as well as their willingness to serve as members of my committee. My peers at Rutgers have been nothing short of amazing, and have contributed so much to this work. Many discussions about this research with Joe Lakawicz has helped make the work much stronger. Also thanks to Peinan Ge, Pete Balogh, and Dan Cordasco for their insight and help.

I also want to thank my parents, Barbara Jean and Bill. Without their hard work and motivating ways, higher education could never have been a possibility for me. Their constant support along the way has been incredible. Thanks to my two older brothers, Bill and Andrew. They have set the bar very high, both personally and professionally. They are my role models, and I thank them for helping shape me into the person I am today. Finally, I would like to thank Yuliya for being there for me all the time. Without her unconditional love and support, I would never have been able to complete this dissertation and achieve my goals.

Table of Contents

Abstract . . . ii

Acknowledgements . . . iv

List of Tables . . . vii

List of Figures . . . viii

1. The Problem of Vitreous Detachment . . . 1

1.1. Anatomy of the Vitreous Body . . . 1

1.2. Posterior Vitreous Detachment (PVD) . . . 3

1.3. Saccadic Motion . . . 4

1.4. Outline of the Dissertation . . . 5

2. Model of the Vitreous Body . . . 8

2.1. Geometry of the Model . . . 9

2.2. Normalization of Parameters . . . 11

2.3. Kinematic and Constitutive Relations . . . 11

2.4. Typical Saccades . . . 14

2.5. Problem Formulation . . . 16

3. Constrained 2D Model . . . 25

3.1. Constraint on Motion . . . 25

3.2. Solution Procedure . . . 28

3.2.1. Undamped Free Vibration Analysis . . . 29

3.2.2. Modal Analysis . . . 31

3.3. Results and Discussion . . . 34

3.3.1. Selection of Geometric and Material Properties 34

3.3.2. Natural Frequencies 36

3.3.3. Mode Shapes 38

3.3.4. Relative Contribution of Modes 39

3.3.5. Vitreous Response Fields 41

3.3.6. Detachment Progression 45

3.3.7. Parameter Study 49

3.4. Conclusions 55

4. Full 2D Solution 56

4.1. Solution Procedure 56

4.1.1. Undamped Free Vibration Response Using the Rayleigh-Ritz Method 61

4.1.2. Modal Analysis 65

4.2. Results and Discussion 67

4.2.1. Natural Frequencies 67

4.2.2. Mode Shapes 69

4.2.3. Relative Contribution of Modes 78

4.2.4. Vitreous Response Fields 80

4.2.5. Detachment Progression 86

4.2.6. Parameter Study 90

4.3. Conclusions 97

5. Concluding Remarks 98

References 101

Appendix A. Constants as Determined by the Rayleigh-Ritz Method . . . 105

List of Tables

A.1. Trial function constants for small detachment size: $R_0 - R_d = 0.036$. 106

A.2. Trial function constants for medium detachment size: $R_0 - R_d = 0.236$. . . 107

A.3. Trial function constants for large detachment size: $R_0 - R_d = 0.436$. 108

List of Figures

1.1. Horizontal cross-section of the human eye. 1

2.1. Model of Region S_2 as a homogeneous medium. 8

2.2. Geometry of the problem statement. 9

2.3. Evolution of the detachment boundaries. 10

2.4. Angular displacement and angular velocity for a variety of saccades. 15

3.1. Natural frequencies as a function of detachment size. 36

3.2. Symmetric and anti-symmetric natural frequencies. 37

3.3. Lowest nine symmetric mode shapes. 38

3.4. Lowest nine anti-symmetric mode shapes. 39

3.5. Modal contribution as a function of dimensional time for small detachment. 40

3.6. Modal contribution as a function of dimensional time for medium detachment. 40

3.7. Modal contribution as a function of dimensional time for large detachment. 40

3.8. Displacement of vitreous during a 20° saccade with detachment size, $R_0 - R_d = 0.236$. 41

3.9. Normal stress, $\sigma_{\phi\phi}$, of the vitreous during a 20° saccade with detachment size, $R_0 - R_d = 0.236$. 42

3.10. Normal stress, σ_{rr}, of the vitreous during a 20° saccade with detachment size, $R_0 - R_d = 0.236$. 42

3.11. Shear stress, $\sigma_{r\phi}$, of vitreous during a 20° saccade with detachment size, $R_0 - R_d = 0.236$. 43

3.12. Inherent force per unit volume, λ, necessary to constrain the radial motion of the vitreous to vanish during a 20° saccade with detachment size, $R_0 - R_d = 0.236$. 43

3.13. Maximum stress fields during a saccade of amplitude 10° with detachment size, $R_0 - R_d = 0.236$. 44
3.14. Maximum stress fields during a saccade of amplitude 20° with detachment size, $R_0 - R_d = 0.236$. 44
3.15. Maximum stress fields during a saccade of amplitude 30° with detachment size, $R_0 - R_d = 0.236$. 45
3.16. Maximum stress fields during a saccade of amplitude 40° with detachment size, $R_0 - R_d = 0.236$. 45
3.17. Energy release rate per unit depth as a function of time for small, medium, and large detachment sizes. 47
3.18. Maximum energy release rate per unit depth as a function of detachment size for saccades of nine different amplitudes. 48
3.19. Critical saccade amplitude per unit bond energy as a function of detachment size. 49
3.20. Lowest nine symmetric natural frequencies for different values of shear modulus. 51
3.21. Maximum stress fields during a saccade of amplitude 20° with detachment size, $R_0 - R_d = 0.236$ where $G_1 = G_2 = 0.5$. 52
3.22. Maximum stress fields during a saccade of amplitude 20° with detachment size, $R_0 - R_d = 0.236$ where $G_1 = G_2 = 1.0$. 52
3.23. Maximum stress fields during a saccade of amplitude 20° with detachment size, $R_0 - R_d = 0.236$ where $G_1 = G_2 = 2.0$. 52
3.24. Energy release rate per unit depth as a function of detachment size for three different values of shear modulus. 53
3.25. Critical saccade amplitude per unit bond energy as a function of detachment size for different values of shear modulus. 54
4.1. Comparison of the natural frequencies as determined by the two models. . . 68
4.2. Circumferential component of Modes 1 - 9. 69
4.3. Circumferential component of Modes 10 - 18. 70
4.4. Radial component of Modes 1 - 9. 71

4.5. Radial component of Modes 10 - 18. 72
4.6. Comparison of Mode 1 of the full 2D model with Mode (1,1) of the circumferential model for detachment size $R_0 - R_d = 0.236$. 73
4.7. Comparison of Mode 2 of the full 2D model with Mode (2,1) of the circumferential model for detachment size $R_0 - R_d = 0.236$. 73
4.8. Comparison of Mode 3 of the full 2D model with Mode (3,1) of the circumferential model for detachment size $R_0 - R_d = 0.236$. 74
4.9. Comparison of Mode 4 of the full 2D model with Mode (4,1) of the circumferential model for detachment size $R_0 - R_d = 0.236$. 74
4.10. Comparison of Mode 5 of the full 2D model with Mode (5,1) of the circumferential model for detachment size $R_0 - R_d = 0.236$. 74
4.11. Comparison of Mode 6 of the full 2D model with Mode (6,1) of the circumferential model for detachment size $R_0 - R_d = 0.236$. 74
4.12. Comparison of Mode 7 of the full 2D model with Mode (1,2) of the circumferential model for detachment size $R_0 - R_d = 0.236$. 75
4.13. Comparison of Mode 8 of the full 2D model with Mode (2,2) of the circumferential model for detachment size $R_0 - R_d = 0.236$. 75
4.14. Comparison of Mode 9 of the full 2D model with Mode (3,2) of the circumferential model for detachment size $R_0 - R_d = 0.236$. 75
4.15. Comparison of Mode 10 of the full 2D model with Mode (4,2) of the circumferential model for detachment size $R_0 - R_d = 0.236$. 75
4.16. Comparison of Mode 11 of the full 2D model with Mode (5,2) of the circumferential model for detachment size $R_0 - R_d = 0.236$. 76
4.17. Comparison of Mode 12 of the full 2D model with Mode (6,2) of the circumferential model for detachment size $R_0 - R_d = 0.236$. 76
4.18. Comparison of Mode 13 of the full 2D model with Mode (1,3) of the circumferential model for detachment size $R_0 - R_d = 0.236$. 76
4.19. Comparison of Mode 14 of the full 2D model with Mode (2,3) of the circumferential model for detachment size $R_0 - R_d = 0.236$. 76

4.20. Comparison of Mode 15 of the full 2D model with Mode (3,3) of the circumferential model for detachment size $R_0 - R_d = 0.236$. 77
4.21. Comparison of Mode 16 of the full 2D model with Mode (4,3) of the circumferential model for detachment size $R_0 - R_d = 0.236$. 77
4.22. Comparison of Mode 17 of the full 2D model with Mode (5,3) of the circumferential model for detachment size $R_0 - R_d = 0.236$. 77
4.23. Comparison of Mode 18 of the full 2D model with Mode (6,3) of the circumferential model for detachment size $R_0 - R_d = 0.236$. 77
4.24. Modal contribution as a function of dimensional time for small detachment. 79
4.25. Modal contribution as a function of dimensional time for medium detachment. 79
4.26. Modal contribution as a function of dimensional time for large detachment. 79
4.27. Comparison of the modal contribution between the two models for a 20° saccade with detachment size $R_0 - Rd = 0.236$. 80
4.28. Comparison of maximum displacement of the vitreous during a 20° saccade with detachment size $R_0 - R_d = 0.236$ for the constrained 2D model to the full 2D model. 81
4.29. Comparison of maximum normal stress, $\sigma_{\phi\phi}$, during a 20° saccade with detachment size, $R_0 - R_d = 0.236$ for the constrained 2D model to the full 2D model. 82
4.30. Comparison of normal stress, σ_{rr}, during a 20° saccade with detachment size, $R_0 - R_d = 0.236$ for the constrained 2D model to the full 2D model. 83
4.31. Comparison of shear stress, $\sigma_{r\phi}$, during a 20° saccade with detachment size, $R_0 - R_d = 0.236$ for the constrained 2D model to the full 2D model. 84
4.32. Maximum stress fields during a saccade of amplitude 10° with detachment size, $R_0 - R_d = 0.236$ as predicted by the full 2D model. 85
4.33. Maximum stress fields during a saccade of amplitude 20° with detachment size, $R_0 - R_d = 0.236$ as predicted by the full 2D model. 85
4.34. Maximum stress fields during a saccade of amplitude 30° with detachment size, $R_0 - R_d = 0.236$ as predicted by the full 2D model. 85

4.35. Maximum stress fields during a saccade of amplitude $40°$ with detachment size, $R_0 - R_d = 0.236$ as predicted by the full 2D model. 85
4.36. Comparison of energy release rate per unit depth as a function of time between the constrained 2D model and the full 2D model for small, medium, and large detachment size. 87
4.37. Comparison of the maximum energy release rate per unit depth as a function of detachment size between the two models for saccades of nine different amplitudes. 88
4.38. Comparison of the critical saccade amplitude per unit bond energy as a function of detachment size between the two models. 89
4.39. Comparison of natural frequencies for different values of shear modulus for the two models. 91
4.40. Comparison of maximum stress fields during a saccade of amplitude $20°$ with detachment size, $R_0 - R_d = 0.236$ where $G_1 = G_2 = 0.5$ for the two models. 92
4.41. Comparison of maximum stress fields during a saccade of amplitude $20°$ with detachment size, $R_0 - R_d = 0.236$ where $G_1 = G_2 = 1.0$ for the two models. 93
4.42. Comparison of maximum stress fields during a saccade of amplitude $20°$ with detachment size, $R_0 - R_d = 0.236$ where $G_1 = G_2 = 2.0$ for the two models. 93
4.43. Comparison of energy release rate per unit depth as a function of detachment size for three different values of shear modulus for the two models. 95
4.44. Comparison of critical saccade amplitude per unit bond energy as a function of detachment size for different values of shear modulus for the two models. 96

Chapter 1

The Problem of Vitreous Detachment

1.1 Anatomy of the Vitreous Body

The vitreous humor is a clear connective gel-like tissue that occupies the majority of the central portion of the human eye, as shown in Figure 1.1. It is composed of at least $98 - 99\%$ water by mass [24]. The rest is primarily composed of collagen and hyaluronic acid, a stabilizing hydrophilic polymer and complex sugar [3] [45] [47]. About 65% of the

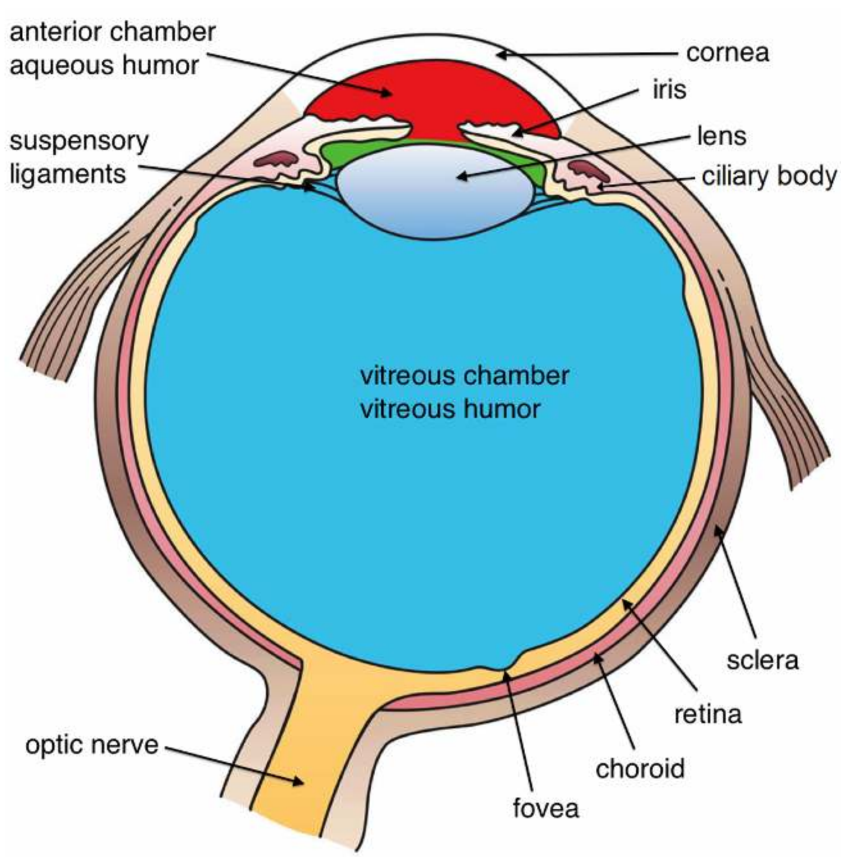

Figure 1.1: Horizontal cross-section of the human eye. Artwork by Holly Fischer [CC BY 3.0 (http://creativecommons.org/licenses/by/3.0)], via Wikimedia Commons.

collagen exists as a hydrated double-network of randomly oriented type II collagen fibrils, while type IX non-fibril collagen accounts for up to 25% of the collagen in the vitreous [8] [13]. The vitreous humor is encased in a membrane known as the vitreous cortex or hyaloid membrane. This membrane is composed of high concentrations of the collagen fibrils within the vitreous, in addition to other cells not found in the rest of the vitreous that are associated exclusively with the interface of the posterior vitreous cortex and the inner limiting layer of the sensory retina [46]. In young healthy eyes, the vitreous fills the entire vitreous cavity and the vitreous cortex is fully attached to the retina, suspensory ligaments, ciliary body, and posterior portion of the crystalline lens.

The vitreous has several functions. It maintains a constant pressure, and thus provides added structural stability for the entire eye, particularly for the surrounding layers including the retina, choroid, and sclera [21]. This pressure also helps regulate the growth and shape of the eye during development [26]. The gel-like vitreous also serves as a barrier preventing the diffusion of large macromolecules, which also helps to maintain its transparency [9]. This transparent nature of the vitreous humor allows 90% of light with wavelengths between 300 and 1400 nm to pass through from the lens and become focused on the posterior retina allowing the eye to see [10]. In addition, the gel-like vitreous regulates oxygen levels in the retina and lens, which protects against cataracts [28]. It is also hypothesized that the vitreous regulates fluid levels as some portion of aqueous solution secreted by the ciliary body diffuses into the vitreous cavity, at which point it is flushed out posteriorly across the retina to the choroid [21].

The vitreous is most firmly attached to its surrounding structures at the vitreous base, a circumferential area that straddles the anterior edge of the retina, as well as the pars plana, a portion of the ciliary body. The vitreous base is generally 2 to 6 mm wide. The fibrils inside the vitreous firmly attach themselves in an interwoven manner to the cells in the adjacent retina and ciliary body. The vitreous base is not a fixed region. It grows with advancing age, and the posterior edge of the vitreous base continually extends toward the equator of the eye [49].

1.2 Posterior Vitreous Detachment (PVD)

It is well documented that the structure of the vitreous body changes with age among other factors such as trauma, high myopia, ocular disease, and irregular vascular passageways [1] [31]. Le Goff and Bishop (2008) [36] provide a detailed summary of the age related biochemical changes in the vitreous body. Due to a loss of type IX collagen from the surface of the type II collagen fibrils, the fibrils begin to aggregate in a mostly anteroposterior orientation resulting in the development of aqueous pockets, as well as other regions more densely packed with fibrils. The volume of the liquid portion of the vitreous increases over time (synchisis), while the volume of the gel-like portion decreases and shrinks (syneresis) [44].

It has been long been observed clinically that there exists a correlation between vitreous liquefaction and posterior vitreous detachment (PVD), in which the vitreous cortex first detaches from the inner layer of the sensory retina in the posterior portion of the eye, after which the detachment progresses. Foos and Wheeler (1982) [20] first documented the statistical correlation between the two phenomena. Sebag (1987) [44] describes two possible mechanisms by which syneresis causes PVD: (1) shortening and condensation of the vitreous fibrils causing separation of the vitreous cortex from the retina; (2) dissolution of the posterior vitreous cortex adhesion to the retina at the posterior pole.

Some form of vitreous detachment is seen in at least one eye in 27% of people in their seventh decade, and in 63% of people over the age of 70 [20]. It is often unaccompanied by easily detected symptoms, nor does it cause serious side effects. PVD, however, can progress either suddenly or over a longer time scale until it reaches a point of abnormally strong vitreo-retinal adhesion. Retinal detachment, a very serious condition associated with possible vision loss, is strongly correlated to PVD of this type [42] [45] [49]. Complete PVD has occurred once the vitreo-retinal detachment extends to the posterior edge of the vitreous base. The vitreo-retinal attachment is much stronger in this region, and only in cases of trauma will separation occur at, or anterior to, the vitreous base. The more common scenario is one where the traction from the vitreous during an eye movement is not strong enough to break this bond, but is strong enough to cause a tear in the retina.

Rhegmatogenous retinal detachment (RRD) then occurs, whereby the liquefied vitreous enters the subretinal space via the retinal tear. Fluid pressure between the layers of the retina then contributes to propagation of retinal detachment.

1.3 Saccadic Motion

It has been hypothesized that saccadic eye movements can be responsible for causing large enough traction from the detached vitreous on the retina to cause a retinal tear. David et al. (1997) [17] used thin isotropic spherical shell theory to model the eye wall in order to analyze the anti-symmetric response of the eye due to saccadic motion. In this study, the extraocular muscles responsible for moving the eye during a saccade were modeled as an axisymmetric band centered on the equator, and the forcing was modeled as a step function. Their results showed that the resultant stress on the eye wall increased for larger eyes and thinner eye walls. A further study by David et al. (1998) [18], which used both analytical and numerical techniques, advanced upon the prior model by filling the vitreous cavity with a viscoelastic fluid. These results suggest that a time-dependent shear force due to saccadic motion of the eye could be responsible for retinal tears.

Repetto et al. (2004) [40] and Repetto et al. (2005) [41] sought to experimentally validate the results determined by David et al. (1998). Studying small sinusoidal saccades, the 2004 work represented the vitreous by an incompressible Newtonian fluid, restricted from rotational motion in a spherical cavity representing the vitreous cavity, whereas the 2005 experiment expanded on the model and filled the cavity with a highly viscous Newtonian fluid using both sinusoidal and polynomial excitation. The polynomial forcing was chosen to more accurately represent the motion of the eye during a saccade. The experiments showed that maximum shear stress on the retinal wall did not strongly correspond to saccade size. The authors therefore hypothesize that small saccades can be just as damaging in the sense of the prevalence of them causing a retinal tear.

In order to further quantify the traction caused by saccadic motion on the retinal walls, Repetto et al. (2011) [42] developed a two-dimensional planar model of the vitreous with PVD. The gel-like vitreous was modeled as a hybrid Neo-Hookean incompressible solid with

Newtonian fluid-like dissipation, while the liquefied vitreous was modeled as a Newtonian incompressible fluid. Finite element simulations showed that, even for saccades as small as 10°, both the normal and tangential components of traction on the retina at the attachment point of the vitreous achieve a maximum value on the same order of magnitude as the retinal adhesive force measured by Kita and Marmor (1992) [32].

More recently, Bonfiglio et al. (2015) [12] conducted an experimental study on the rotation of a spherical cavity filled with an artificial vitreous humor, which has viscoelastic mechanical properties similar to the real vitreous. The spherical cavity was subject to sinusoidal motion. Results showed that resonant excitation of the fluid can occur within the range of possible saccades. The authors, therefore, suggest that saccades which cause resonant excitation of the vitreous fluid will in turn cause large stresses on the retina that lead to tears.

While it is now largely agreed that saccadic motion in the case of total PVD can be responsible for retinal tears, little is known about the effects saccadic motion can have on the detachment progression in the case of partial PVD. To this point, the progression of PVD has been studied from bio-chemical and rheological standpoints [27] [44]. In these studies, the amount of detachment is thought to be correlated with the amount of synchysis. Another hypothesis suggests that the bond between the vitreous and retina dissolves with synchysis, and that liquid vitreous enters the retrocortical space (between the vitreous cortex and the retina) causing further detachment between the vitreous cortex and the inner layer of the retina [19] [44].

In contrast, the fundamental hypothesis of the present study is that saccadic movement of the eye can play a role in the evolution of vitreo-retinal detachment, progressing from partial to total PVD. To the author's knowledge, no analytical study addressing the effects of saccadic movement on the progression of PVD exists in the literature to date.

1.4 Outline of the Dissertation

The dissertation is presented in five chapters. Chapter 2 describes a mechanics based mathematical model for vitreo-retinal detachment based on energy conditions. The problem is formulated as a two-dimensional propagating boundary value problem in the calculus of variations, in the spirit of Bottega (1983) [14], as well as for an eye encircled by a scleral buckle as seen in Ge et al. (2016) [22] and Ge et al. (2017) [23]. This type of formulation has been proven to be successful for predicting the behavior and evolution of retinal detachment as seen in Bottega et al. (2013) [16] and Lakawicz et al. (2015) [33]. The variational formulation yields self-consistent governing equations and boundary conditions for the motion of the vitreous body under saccadic movement. By allowing the boundaries of detachment to propagate, the variational formulation also yields a self-consistent energy release rate that governs detachment of the vitreous from the retina, as well as yielding an iterative formula for determining a critical saccade amplitude that will cause detachment to progress.

In Chapter 3, the model presented in Chapter 2 is simplified so as to only consider circumferential motion of the vitreous, as it is anticipated that this will be the dominant motion of the vitreous when subject to a horizontal saccade, as this is the direction of rotation. The corresponding coupled partial differential equations of motion are solved exactly using modal analysis. The resultant displacement and stress-fields are then presented and analyzed. Detachment behavior is predicted by the transversality condition containing the energy release rate of the detaching vitreous cortex, which comes about as a consequence of the variational principle when allowing the detachment boundaries to propagate. Threshold paths are presented, which determine the minimum saccade amplitude necessary to cause vitreo-retinal detachment to progress as a function of detachment size. This allows for prediction of evolution of vitreo-retinal detachment.

Chapter 4 presents the solution to the full 2D model developed in Chapter 2. The radial constraint on the response of the vitreous implicitly imposed in Chapter 3 is relaxed. The governing equations of motion are solved quasi-analytically via the Rayleigh-Ritz Method and modal analysis. Results for the vitreous response fields are presented and compared to those for the circumferential motion model of Chapter 3. Detachment behavior is determined and again compared to that of the circumferential motion model. Results show that the full model solution is more susceptible to saccade driven vitreo-retinal detachment.

Chapter 5 summarizes the results of the present study. The results of the two models are compared to each other, and to clinically observed behavior. Implications of these models are then presented. Finally, further problems involving the behavior of the retina in which this model is applicable are presented.

Chapter 2

Model of the Vitreous Body

In this chapter, a two-dimensional dynamic mathematical model for determining the motion and detachment progression of an eye with partial PVD subject to saccadic eye movement is formulated. The vitreous is comprised of two separate phases as shown in Figure 2.1a. The lighter shade represents the gel-like vitreous, while the darker shade represents the liquefied vitreous. The boundary between them represents the detached vitreous cortex. When subject to a single saccade, the gel-like portion will swing while the liquefied portion will slosh. The shape of the detached vitreous cortex will be changing and evolving constantly. Kakehashi et al. (1997) [31] noted the detached shape of the vitreous cortex can vary significantly. Accordingly, they classify the detachment as PVD with collapse and PVD without collapse, where collapse implies a change in the concavity of the detached vitreous cortex. Since it is impossible to know the exact shape of the detached vitreous at all points

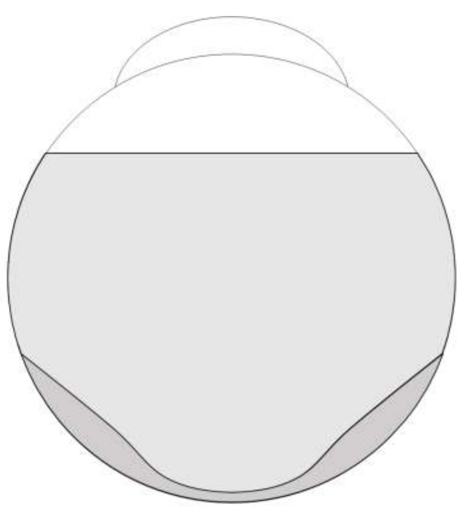

(a) One such possible configuration of the vitreous cavity.

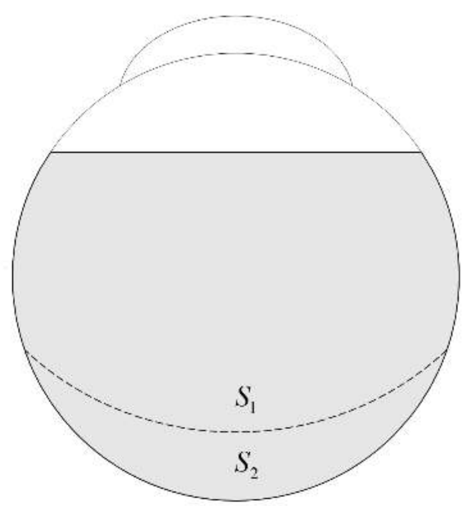

(b) Model of the vitreous cavity.

Figure 2.1: Model of Region S_2 as a homogeneous medium.

in time, in the present work, the properties are dispersed uniformly as shown in Figure 2.1b. It is felt that the bulk motion of the vitreous will predominate in its detachment from the sensory retina, and this model will capture the same inertial effect without having to assume a shape for the detached vitreous cortex.

2.1 Geometry of the Model

The vitreous detachment is assumed to be symmetric about the anteroposterior center-line of the eye. The vitreous is divided into two regions, S_1 and S_2, as shown in Figure 2.1b. Region S_1 is composed of the gel-like portion of the vitreous body. The anterior portion of this region is adhered to the ciliary body and crystalline lens, while on its lateral and medial edges it is adhered to the retinal walls. Region S_2 is comprised of gel-like vitreous, the detached vitreous cortex, and the liquefied portion of the vitreous represented as a homogeneous region. Region S_2 represents the portion of the vitreous inside the vitreous cavity beyond the point where the vitreous cortex has detached from the retina.

Figure 2.2 shows the relevant geometry of the model. The eye of radius R is subject to horizontal saccadic motion, whereby the eye rotates about its geometric center. Polar coordinates (r, ϕ) emanate from the posterior surface of the crystalline lens, point O, in the

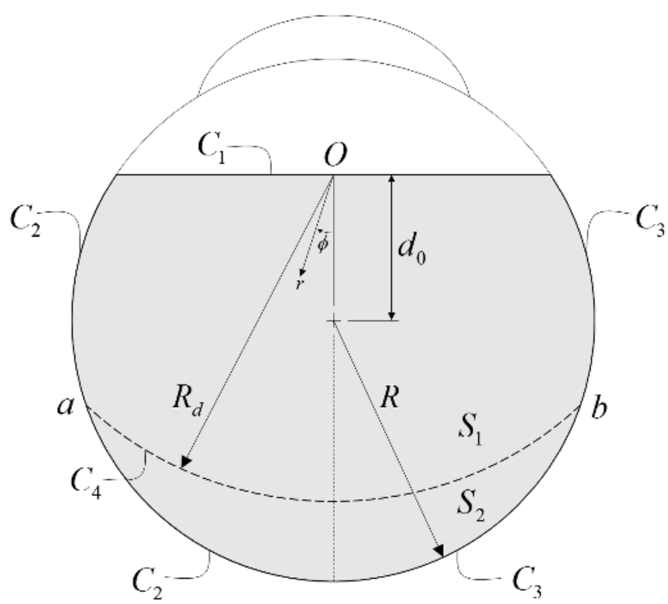

Figure 2.2: Geometry of the problem statement.

horizontal plane passing through the center of the eye whose normal vector points in the superior direction. The distance between the geometric center of the eye and the origin of the coordinate system, point O, is denoted as d_0. Region S_1, the gel-like portion, is fixed to the ciliary body and crystalline lens along boundary C_1, while it is adhered to the retinal walls along boundaries C_2 and C_3. Region S_2 is bounded by surfaces C_2 and C_3, which represent the retinal wall.

The two regions are separated by the boundary C_4, which is located a uniform radial distance, R_d from point O. The maximum radius of boundary C_4 allowable is denoted $R_0 = R + d_0$, which is the radius that corresponds to a fully intact vitreous. As the vitreous detachment from the sensory retina progresses in the anterior direction, Region S_1 shrinks, while region S_2 grows. Detachment occurs along the boundaries C_2 and C_3. The boundary C_4 will therefore recede while, for the current idealization, preserving a uniform radial shape. In Figure 2.2, point a represents the detachment point along boundary C_2, while point b represents the detachment point along boundary C_3. These points are not fixed but, rather, propagate in the anterior direction as detachment progresses, as shown in Figure 2.3. Further justification and limitations of this geometry will be explained when discussing the kinematic and constitutive relations later in this chapter.

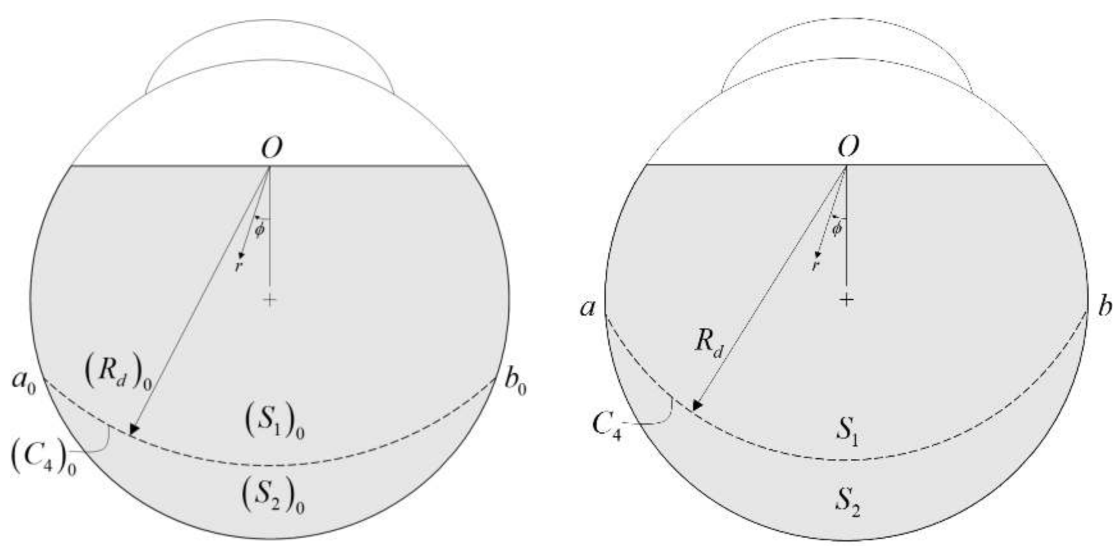

(a) Geometry of the vitreous at some time, t_0. (b) Geometry of the vitreous at a later time, $t_0 + \Delta t$, after vitreous detachment has progressed.

Figure 2.3: Evolution of the detachment boundaries.

2.2 Normalization of Parameters

Human eyes vary in size. They grow with age, and an individual can have two eyes of different size at any given time. To this end, it is advantageous to formulate the model for vitreous detachment in non-dimensional units. This allows the model to predict essential qualitative behavior that is applicable to a wide range of configurations.

Length scales and displacements are normalized by the dimensional radius of the eye, $\overline{R}$. Material properties in either region, namely the elastic and shear moduli, are normalized with respect to the dimensional shear modulus in Region S_1, $\overline{G}_1$. In addition, the mass density in either region is normalized by the dimensional mass density in Region S_1, $\overline{\rho}_1$. In a manner consistent with the above normalization, time is non-dimensionalized with respect to the dimensional shear wave speed, $\sqrt{\overline{G}_1/\overline{\rho}_1}$, in Region S_1, as well as the dimensional radius of the eye, $\overline{R}$. The normalized time is thus expressed as

$$t = \frac{\bar{t}}{\overline{R}}\sqrt{\frac{\overline{G}_1}{\overline{\rho}_1}}, \tag{2.1}$$

where $\bar{t}$ is the dimensional time.

2.3 Kinematic and Constitutive Relations

Small deformations are assumed for the model, and thus the (infinitesimal) strain-displacement equations take the form

$$\varepsilon_{rr}^{(j)} = \frac{\partial u_j}{\partial r} \qquad (j = 1, 2)\,, \tag{2.2a}$$

$$\varepsilon_{\phi\phi}^{(j)} = \frac{1}{r}\left(\frac{\partial v_j}{\partial \phi} + u_j\right) \qquad (j = 1, 2)\,, \tag{2.2b}$$

$$\varepsilon_{r\phi}^{(j)} = \frac{1}{2}\left(\frac{1}{r}\frac{\partial u_j}{\partial \phi} + \frac{\partial v_j}{\partial r} - \frac{v_j}{r}\right) \qquad (j = 1, 2)\,, \tag{2.2c}$$

where u_j and v_j represent normalized radial and circumferential displacement of the vitreous, respectively, in Region S_j, $\varepsilon_{rr}^{(j)}$ and $\varepsilon_{\phi\phi}^{(j)}$ are the normal strains in the radial and circumferential directions in Region S_j, respectively, and $\varepsilon_{r\phi}^{(j)}$ is the in-plane shear strain in Region S_j for $j = 1, 2$.

The vitreous is modeled as randomly-oriented elastic fibrils embedded in a fluid matrix. Since the fibrils are mostly randomly-oriented (though some have bound together during syneresis), they are modeled as an elastic isotropic solid. The aqueous solution is modeled as a fluid matrix, which imposes a hydrodynamic drag, effectively dampening the motion of the vitreous. This damping factor is naturally proportional to the elastic parameter. Therefore, the state of stress at any point in the vitreous can be decomposed into two parts: elastic stress associated with the fibrils, and viscous stress associated with the damping due to the fluid matrix. The elastic portion of the constitutive relations are further broken down into two components: one that is due to the dynamic motion of the system, and another that is due to the intraocular pressure (IOP) in the vitreous. The IOP is due to the hydrostatic pressure of the aqueous solution in the eye. The state of stress within the vitreous can thus be expressed as

$$\sigma_{rr}^{(T;j)} = \sigma_{rr}^{(K;j)} + \sigma_{rr}^{(V;j)} - p \qquad (j = 1, 2)\,, \tag{2.3a}$$

$$\sigma_{\phi\phi}^{(T;j)} = \sigma_{\phi\phi}^{(K;j)} + \sigma_{\phi\phi}^{(V;j)} - p \qquad (j = 1, 2)\,, \tag{2.3b}$$

$$\sigma_{r\phi}^{(T;j)} = \sigma_{r\phi}^{(K;j)} + \sigma_{r\phi}^{(V;j)} \qquad (j = 1, 2)\,, \tag{2.3c}$$

where $\sigma_{rr}^{(T;j)}$ and $\sigma_{\phi\phi}^{(T;j)}$ are the normalized total normal stresses in the radial and circumferential directions, respectively, and $\sigma_{r\phi}^{(T;j)}$ is the normalized total shear stress in either region. $\sigma_{rr}^{(K;j)}$ and $\sigma_{\phi\phi}^{(K;j)}$ are the normalized dynamic normal stresses in the radial and circumferential directions, respectively, and $\sigma_{r\phi}^{(K;j)}$ is the normalized dynamic shear stress in either region. $\sigma_{rr}^{(V;j)}$ and $\sigma_{\phi\phi}^{(V;j)}$ are the normalized components of normal stresses in the radial and circumferential directions due solely to the hydrodynamic drag of the fluid matrix, respectively, and $\sigma_{r\phi}^{(V;j)}$ is the normalized component of shear stress due to the hydrodynamic drag of the fluid matrix, in either region. Lastly, p represents the IOP in the vitreous.

The dynamic components of stress in Region S_1 are related to the strain by the isotropic plane strain constitutive equations, which take the following form

$$\begin{aligned}\sigma_{rr}^{(K;1)} &= \frac{E_1}{(1+\nu_1)(1-2\nu_1)}\left[(1-\nu_1)\,\varepsilon_{rr}^{(1)} + \nu_1\varepsilon_{\phi\phi}^{(1)}\right] \\ &= \frac{2G_1}{(1-2\nu_1)}\left[(1-\nu_1)\,\varepsilon_{rr}^{(1)} + \nu_1\varepsilon_{\phi\phi}^{(1)}\right],\end{aligned} \tag{2.4a}$$

$$\begin{aligned}\sigma_{\phi\phi}^{(K;1)} &= \frac{E_1}{(1+\nu_1)(1-2\nu_1)}\left[(1-\nu_1)\,\varepsilon_{\phi\phi}^{(1)} + \nu_1\varepsilon_{rr}^{(1)}\right] \\ &= \frac{2G_1}{(1-2\nu_1)}\left[(1-\nu_1)\,\varepsilon_{\phi\phi}^{(1)} + \nu_1\varepsilon_{rr}^{(1)}\right],\end{aligned} \tag{2.4b}$$

$$\sigma_{r\phi}^{(K;1)} = 2G_1\varepsilon_{r\phi}^{(1)}, \tag{2.4c}$$

where E_1 is the normalized elastic modulus, G_1 is the normalized shear modulus, and ν_1 is Poisson's ratio in Region S_1.

As stated earlier, Region S_2 consists of three phases: the gel-like vitreous, the detached vitreous cortex, and the liquefied vitreous. Physically, these portions move with greater freedom than Region S_1, as there are no longer any fibrils that are embedded into the sensory retina in this region. Thus it is a hypothesis of this work that the inertia of this region during a saccade that will contribute to the spreading of PVD. Region S_2 is therefore modeled in such a way that it captures the inertial effects of the vitreous beyond $r = R_d$. This is accounted for by using an analogous constitutive model to that for Region S_1 but with vanishing elastic modulus, E_2, as the fibrils are not constrained to be embedded into the sensory retina in this region. This causes Region S_2 to be less constrained than Region S_1 (but still allows for an analytical solution for the governing equations). The dynamic components of stress in Region S_2 are therefore related to the strain as follows

$$\sigma_{rr}^{(K;2)} = 0, \tag{2.5a}$$

$$\sigma_{\phi\phi}^{(K;2)} = 0, \tag{2.5b}$$

$$\sigma_{r\phi}^{(K;2)} = 2G_2\varepsilon_{r\phi}^{(2)}. \tag{2.5c}$$

The viscous portion of stress is due to the hydrodynamic drag caused by the fluid medium. Therefore, the viscous stress is modeled as being proportional to the velocity of the vitreous continuum, and take the following forms in each region

$$\sigma_{rr}^{(V;j)} = \frac{c_j}{(1+\nu_j)(1-2\nu_j)} \left[(1-\nu_j) \frac{\partial \varepsilon_{rr}^{(j)}}{\partial t} + \nu_j \frac{\partial \varepsilon_{\phi\phi}^{(j)}}{\partial t} \right] \qquad (j = 1, 2)\,, \tag{2.6a}$$

$$\sigma_{\phi\phi}^{(V;j)} = \frac{c_j}{(1+\nu_j)(1-2\nu_j)} \left[(1-\nu_j) \frac{\partial \varepsilon_{\phi\phi}^{(1)}}{\partial t} + \nu_j \frac{\partial \varepsilon_{rr}^{(j)}}{\partial t} \right] \qquad (j = 1, 2)\,, \tag{2.6b}$$

$$\sigma_{r\phi}^{(V;1)} = \frac{c_j}{(1+\nu_1)} \frac{\partial \varepsilon_{r\phi}^{(1)}}{\partial t} \qquad (j = 1, 2)\,, \tag{2.6c}$$

where c_1 and c_2 are the damping coefficients in Regions S_1 and S_2, respectively.

2.4 Typical Saccades

This study considers the dynamic response of the vitreous subject to a single horizontal saccade. To characterize saccadic motion, the present study adopts the model employed by Repetto et al. (2005) [41], and originally developed by Becker (1989) [5]. In this model, the angular displacement of a typical saccade in the range of 10° to 50° as a function of time is modeled as a fifth-order polynomial that depends on three factors: (1) the amplitude, A, of the saccade, (2) the duration of the saccade, t_s, and (3) the peak angular velocity of the saccade, Ω_p.

In the range of saccades considered here (10° to 50°), the duration of the saccade, t_s, is described accurately by the following linear function of the saccade amplitude

$$t_s = 0.0025A + 0.025. \tag{2.7}$$

Equation (2.7) is based on experimental studies including those of Bahill, Brockenbrough, and Troost (1981) [2], Baloh et al. (1975) [4], and Robinson (1964) [43]. It has also been shown experimentally by the aforementioned studies, as well as Boghen et al. (1974) [11] and Inchingolo and Spanio (1985)[30], that the time to peak velocity, t_p, depends on the saccade amplitude and the duration of the saccade as given by the formula

$$\frac{t_p}{t_s} = 0.5 - 0.005A. \tag{2.8}$$

Since the saccade duration was shown to be solely dependent on the saccade amplitude, the saccadic motion of the eye can be characterized solely by the amplitude, A.

The angular displacement, ψ, of the eye during a typical $10°$ to $50°$ saccade is given as a function of time by the relation

$$\psi(t) = \left(c_0 + c_1 t + c_2 t^2 + c_3 t^3 + c_4 t^4 + c_5 t^5\right)\left[\mathcal{H}\left(t\right) - \mathcal{H}\left(t - t_s\right)\right] + A\mathcal{H}\left(t - t_s\right), \tag{2.9}$$

where $\mathcal{H}\left(t\right)$ is the Heaviside step function, and the coefficients c_0 through c_5 are determined by the following conditions:

$$\psi(0) = 0, \tag{2.10a}$$

$$\psi(t_s) = A, \tag{2.10b}$$

$$\frac{\partial}{\partial t}\psi(0) = 0, \tag{2.10c}$$

$$\frac{\partial}{\partial t}\psi(t_s) = 0, \tag{2.10d}$$

$$\frac{\partial}{\partial t}\psi(t_p) = \Omega_p, \tag{2.10e}$$

$$\frac{\partial^2}{\partial t^2}\psi(t_p) = 0. \tag{2.10f}$$

The dimensional angular displacement and dimensional angular velocity of the eye during the saccade are shown in Figure 2.4 (a reproduction of Figure 1 from Repetto et al. (2005) [41] but extended herein to include $50°$ saccades) as functions of the dimensional time during saccades ranging from $10°$ to $50°$.

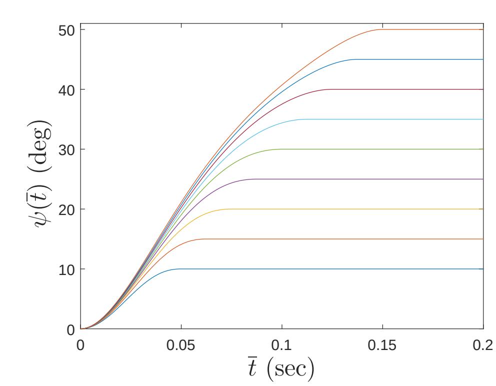

(a) Dimensional angular displacement of the eye as a function of time during various saccades.

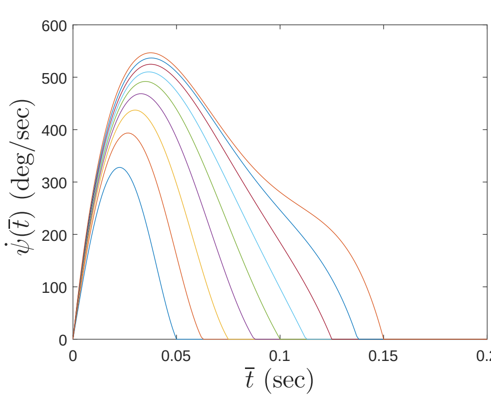

(b) Dimensional angular velocity of the eye as a function of time during various saccades.

Figure 2.4: Angular displacement and angular velocity for a variety of saccades.

As shown by Equation (2.8), and as seen in Figure 2.4b, the angular velocity is not symmetric with respect to time, especially for larger saccades. Therefore, the polynomial gives a more accurate representation of true saccadic motion as opposed to modeling the angular velocity as a sinusoidal wave, as is common practice such as in the works of David (1998) [18], Meskauskas et al. (2012) [37], Bonfiglio et al. (2015) [12], and Modarreszadeh and Abouali (2014) [38] among others.

2.5 Problem Formulation

The problem of the vitreous dynamics and the evolution of vitreous detachment during saccadic motion is approached as a moving boundary problem in the calculus of variations, and the uniform radius of the boundary C_4 between the two regions is allowed to vary arbitrarily, in addition to the displacements, u_1, u_2, v_1, and v_2. The action integral (per unit depth), Π, is formulated next and yields the governing equations of motion, the associated boundary conditions, and a transversality condition upon application of Hamilton's Principle. Hence,

$$\Pi = \mathcal{T}^{(1)} + \mathcal{T}^{(2)} - \mathcal{U}^{(1)} - \mathcal{U}^{(2)} + \mathcal{W}_V^{(1)} + \mathcal{W}_V^{(2)} - \mathcal{E}_F, \tag{2.11}$$

where $\mathcal{T}^{(1)}$ and $\mathcal{T}^{(2)}$ are the kinetic energy per unit depth in Regions S_1 and S_2, respectively, $\mathcal{U}^{(1)}$ and $\mathcal{U}^{(2)}$ are the strain energy per unit depth in Regions S_1 and S_2, respectively, $\mathcal{W}_V^{(1)}$ and $\mathcal{W}_V^{(2)}$ are the virtual work per unit depth of the viscous damping forces of the fluid medium in Regions S_1 and S_2, respectively, and $\mathcal{E}_F$ represents the energy per unit depth absorbed during detachment.

Upon saccadic motion, point O, the point on the vitreous body that is attached to the posterior edge of the lens and is the origin of the coordinate system, rotates about the center of the eye with normalized velocity of magnitude

$$\frac{\partial u_o}{\partial t} = d_0 \frac{\partial}{\partial t}\psi(t), \tag{2.12}$$

with respect to a fixed reference frame with origin at the center of the eye, where u_o is the displacement of point O in this fixed reference frame. Therefore, the absolute velocity of any point in the vitreous during a saccade is the vector sum of its relative velocity with respect to point O and the aforementioned velocity of point O with respect to the fixed reference frame. The kinetic energy per unit depth in Regions S_1 and S_2 measured from the fixed reference frame, therefore, take the following forms

$$\begin{aligned}\mathcal{T}^{(1)} = \frac{1}{2}\iint\limits_{A_1} \rho_1 \Bigg[& \left(\frac{\partial u_1}{\partial t} + \frac{\partial u_o}{\partial t}\frac{d_0 \sin\phi}{\sqrt{r^2 + d_0^2 - 2rd_0\cos\phi}}\right)^2 \\ & + \left(\frac{\partial v_1}{\partial t} + \frac{\partial u_o}{\partial t}\frac{r - d_0\cos\phi}{\sqrt{r^2 + d_0^2 - 2rd_0\cos\phi}}\right)^2\Bigg] dA,\end{aligned} \tag{2.13a}$$

$$\begin{aligned}\mathcal{T}^{(2)} = \frac{1}{2}\iint\limits_{A_2} \rho_2 \Bigg[& \left(\frac{\partial u_2}{\partial t} + \frac{\partial u_o}{\partial t}\frac{d_0 \sin\phi}{\sqrt{r^2 + d_0^2 - 2rd_0\cos\phi}}\right)^2 \\ & + \left(\frac{\partial v_2}{\partial t} + \frac{\partial u_o}{\partial t}\frac{r - d_0\cos\phi}{\sqrt{r^2 + d_0^2 - 2rd_0\cos\phi}}\right)^2\Bigg] dA,\end{aligned} \tag{2.13b}$$

where A_1 and A_2 are the planar areas of Regions S_1 and S_2, respectively.

The elastic strain energy per unit depth in each region is given by

$$\mathcal{U}^{(j)} = \frac{1}{2}\iint\limits_{A_j} \left[\left(\sigma_{rr}^{(K;j)} - p\right)\varepsilon_{rr}^{(j)} + \left(\sigma_{\phi\phi}^{(K;j)} - p\right)\varepsilon_{\phi\phi}^{(j)} + 2\sigma_{r\phi}^{(K;j)}\varepsilon_{r\phi}^{(j)}\right] dA \qquad (j = 1, 2)\,. \tag{2.14}$$

Substitution of Equations (2.2), (2.4), and (2.5) into Equation (2.14) yields the strain energy per unit depth expressed in terms of displacements. Hence,

$$\begin{aligned}\mathcal{U}^{(1)} = \frac{1}{2}\iint\limits_{A_1} \Bigg\{ & \frac{2G_1}{1-2\nu_1}\left[(1-\nu_1)\frac{\partial u_1}{\partial r} + \frac{\nu_1}{r}\left(\frac{\partial v_1}{\partial \phi} + u_1\right)\right]\frac{\partial u_1}{\partial r} \\ & + \frac{2G_1}{1-2\nu_1}\left[\frac{(1-\nu_1)}{r}\left(\frac{\partial v_1}{\partial \phi} + u_1\right) + \nu_1\frac{\partial u_1}{\partial r}\right]\frac{1}{r}\left(\frac{\partial v_1}{\partial \phi} + u_1\right) \\ & + G_1\left(\frac{1}{r}\frac{\partial u_1}{\partial \phi} + \frac{\partial v_1}{\partial r} - \frac{v_1}{r}\right)^2 - p\left[\frac{\partial u_1}{\partial r} + \frac{1}{r}\left(\frac{\partial v_1}{\partial \phi} + u_1\right)\right]\Bigg\} dA,\end{aligned} \tag{2.15a}$$

$$\mathcal{U}^{(2)} = \frac{1}{2}\iint\limits_{A_2} \left\{G_2\left(\frac{1}{r}\frac{\partial u_2}{\partial \phi} + \frac{\partial v_2}{\partial r} - \frac{v_2}{r}\right)^2 - p\left[\frac{\partial u_2}{\partial r} + \frac{1}{r}\left(\frac{\partial v_2}{\partial \phi} + u_2\right)\right]\right\} dA. \tag{2.15b}$$

In addition to the kinetic and potential energies of the system, the virtual work of the viscous damping of the fluid medium must be added to the formulation, and are expressed as follows

$$\mathcal{W}_V^{(1)} = \frac{1}{2}\iint\limits_{A_1} \left\{ \frac{c_1}{(1+\nu_1)(1-2\nu_1)} \left[(1-\nu_1)\frac{\partial^2 u_1}{\partial t \partial r} + \frac{\nu_1}{r}\left(\frac{\partial^2 v_1}{\partial t \partial \phi} + \frac{\partial u_1}{\partial t}\right)\right]\frac{\partial u_1}{\partial r} \right.$$
$$+ \frac{c_1}{(1+\nu_1)(1-2\nu_1)}\left[\frac{(1-\nu_1)}{r}\left(\frac{\partial^2 v_1}{\partial t\partial\phi} + \frac{\partial u_1}{\partial t}\right) + \nu_1 \frac{\partial^2 u_1}{\partial t \partial r}\right]\frac{1}{r}\left(\frac{\partial v_1}{\partial \phi} + u_1\right) \quad (2.16a)$$
$$\left. + \frac{c_1}{1+\nu_1}\left(\frac{1}{r}\frac{\partial^2 u_1}{\partial t\partial\phi} + \frac{\partial^2 v_1}{\partial t \partial r} - \frac{1}{r}\frac{\partial v_1}{\partial t}\right)\left(\frac{1}{r}\frac{\partial u_1}{\partial\phi} + \frac{\partial v_1}{\partial r} - \frac{1}{r}v_1\right)\right\} dA,$$

$$\mathcal{W}_V^{(2)} = \frac{1}{2}\iint\limits_{A_2} \frac{c_2}{1+\nu_2}\left(\frac{1}{r}\frac{\partial^2 u_2}{\partial t\partial\phi} + \frac{\partial^2 v_2}{\partial t \partial r} - \frac{1}{r}\frac{\partial v_2}{\partial t}\right)\left(\frac{1}{r}\frac{\partial u_2}{\partial\phi} + \frac{\partial v_2}{\partial r} - \frac{1}{r}v_2\right) dA. \quad (2.16b)$$

Lastly, $\mathcal{E}_F$, the energy per unit depth absorbed by the vitreo-retinal interface during the growth of the detachment at points a and b, is given by

$$\mathcal{E}_F = 2\gamma\,(a_0 - a) + 2\gamma\,(b_0 - b)\,, \quad (2.17)$$

where γ is the energy per unit depth required to produce a unit area of detachment, a material property of the vitreo-retinal interface, and a_0 and b_0 correspond to some initial values of a and b, respectively.

For the problem at hand, Hamilton's Principle takes the form

$$\delta \int_{t_1}^{t_2} \Pi dt = 0. \quad (2.18)$$

Substitution of Equation (2.11) into Equation (2.18), and performing the variations yields governing equations of the form

$$\mathbf{m}_1 \frac{\partial^2 \mathbf{u}_1}{\partial t^2} + \mathbf{c}_1 \frac{\partial \mathbf{u}_1}{\partial t} + \mathbf{k}_1 \mathbf{u}_1 = \mathbf{F}_1, \quad (2.19a)$$

$$\mathbf{m}_2 \frac{\partial^2 \mathbf{u}_2}{\partial t^2} + \mathbf{c}_2 \frac{\partial \mathbf{u}_2}{\partial t} + \mathbf{k}_2 \mathbf{u}_2 = \mathbf{F}_2, \quad (2.19b)$$

where

$$\mathbf{u}_j = \begin{bmatrix} u_j(r,\phi,t) \\ v_j(r,\phi,t) \end{bmatrix} \qquad (j = 1, 2)\,. \quad (2.20a)$$

The parameters $\mathbf{m}_j$, $\mathbf{c}_j$, and $\mathbf{k}_j$ $(j = 1, 2)$ represent the mass, damping, and stiffness differential operators for each region, respectively. They take the following forms

$$\mathbf{m}_1 = \begin{bmatrix} \rho_1 & 0 \\ 0 & \rho_1 \end{bmatrix}, \tag{2.21a}$$

$$\mathbf{m}_2 = \begin{bmatrix} \rho_2 & 0 \\ 0 & \rho_2 \end{bmatrix}, \tag{2.21b}$$

$$\mathbf{k}_1 = \begin{bmatrix} \mathbf{k}_1^{(1,1)} & \mathbf{k}_1^{(1,2)} \\ \mathbf{k}_1^{(2,1)} & \mathbf{k}_1^{(2,2)} \end{bmatrix}, \tag{2.22a}$$

$$\mathbf{k}_2 = \begin{bmatrix} \mathbf{k}_2^{(1,1)} & \mathbf{k}_2^{(1,2)} \\ \mathbf{k}_2^{(2,1)} & \mathbf{k}_2^{(2,2)} \end{bmatrix}, \tag{2.22b}$$

$$\mathbf{c}_1 = \begin{bmatrix} \mathbf{c}_1^{(1,1)} & \mathbf{c}_1^{(1,2)} \\ \mathbf{c}_1^{(2,1)} & \mathbf{c}_1^{(2,2)} \end{bmatrix}, \tag{2.23a}$$

$$\mathbf{c}_2 = \begin{bmatrix} \mathbf{c}_2^{(1,1)} & \mathbf{c}_2^{(1,2)} \\ \mathbf{c}_2^{(2,1)} & \mathbf{c}_2^{(2,2)} \end{bmatrix}, \tag{2.23b}$$

$$\mathbf{F}_1 = \begin{bmatrix} -\frac{\rho_1 d_0 \sin\phi}{\sqrt{r^2+d_0^2-2rd_0\cos\phi}} \frac{\partial^2 u_o}{\partial t^2} \\ -\frac{\rho_1 (r-d_0\cos\phi)}{\sqrt{r^2+d_0^2-2rd_0\cos\phi}} \frac{\partial^2 u_o}{\partial t^2}, \end{bmatrix}, \tag{2.24a}$$

$$\mathbf{F}_2 = \begin{bmatrix} -\frac{\rho_2 d_0 \sin\phi}{\sqrt{r^2+d_0^2-2rd_0\cos\phi}} \frac{\partial^2 u_o}{\partial t^2} \\ -\frac{\rho_2 (r-d_0\cos\phi)}{\sqrt{r^2+d_0^2-2rd_0\cos\phi}} \frac{\partial^2 u_o}{\partial t^2}, \end{bmatrix}, \tag{2.24b}$$

where

$$\mathbf{k}_1^{(1,1)} = -\frac{2G_1(1-\nu_1)}{1-2\nu_1}\left[\frac{\partial^2}{\partial r^2} + \frac{1}{r}\frac{\partial}{\partial r} - \frac{1}{r^2}\right] - \frac{G_1}{r^2}\frac{\partial^2}{\partial \phi^2}, \tag{2.25a}$$

$$\mathbf{k}_1^{(1,2)} = \frac{2G_1}{1-2\nu_1}\frac{1}{r}\left[\frac{1-\nu_1}{r}\frac{\partial}{\partial\phi} - \nu_1\frac{\partial^2}{\partial r\partial\phi}\right] - \frac{G_1}{r}\left[\frac{\partial^2}{\partial r\partial\phi} - \frac{1}{r}\frac{\partial}{\partial\phi}\right], \tag{2.25b}$$

$$\mathbf{k}_1^{(2,1)} = -\frac{2G_1}{1-2\nu_1}\frac{1}{r}\left[\frac{1-\nu_1}{r}\frac{\partial}{\partial\phi} + \nu_1\frac{\partial^2}{\partial r\partial\phi}\right] - \frac{G_1}{r}\left[\frac{1}{r}\frac{\partial}{\partial\phi} + \frac{\partial^2}{\partial r\partial\phi}\right], \tag{2.25c}$$

$$\mathbf{k}_1^{(2,2)} = -\frac{2G_1(1-\nu_1)}{1-2\nu_1}\frac{1}{r^2}\frac{\partial^2}{\partial\phi^2} - G_1\left[\frac{\partial^2}{\partial r^2} + \frac{1}{r}\frac{\partial}{\partial r} - \frac{1}{r^2}\right], \tag{2.25d}$$

$$\mathbf{k}_2^{(1,1)} = -\frac{G_2}{r^2}\frac{\partial^2}{\partial\phi^2}, \tag{2.26a}$$

$$\mathbf{k}_2^{(1,2)} = -\frac{G_2}{r}\left[\frac{\partial^2}{\partial r\partial\phi} - \frac{1}{r}\frac{\partial}{\partial\phi}\right], \tag{2.26b}$$

$$\mathbf{k}_2^{(2,1)} = -\frac{G_2}{r}\left[\frac{1}{r}\frac{\partial}{\partial\phi} + \frac{\partial^2}{\partial r\partial\phi}\right], \tag{2.26c}$$

$$\mathbf{k}_2^{(2,2)} = -G_2\left[\frac{\partial^2}{\partial r^2} + \frac{1}{r}\frac{\partial}{\partial r} - \frac{1}{r^2}\right], \tag{2.26d}$$

$$\mathbf{c}_1^{(1,1)} = \frac{c_1}{2G_1(1+\nu_1)}\mathbf{k}_1^{(1,1)}, \tag{2.27a}$$

$$\mathbf{c}_1^{(1,2)} = \frac{c_1}{2G_1(1+\nu_1)}\mathbf{k}_1^{(1,2)}, \tag{2.27b}$$

$$\mathbf{c}_1^{(2,1)} = \frac{c_1}{2G_1(1+\nu_1)}\mathbf{k}_1^{(2,1)}, \tag{2.27c}$$

$$\mathbf{c}_1^{(2,2)} = \frac{c_1}{2G_1(1+\nu_1)}\mathbf{k}_1^{(2,2)}, \tag{2.27d}$$

$$\mathbf{c}_2^{(1,1)} = \frac{c_2}{2G_2(1+\nu_2)}\mathbf{k}_2^{(1,1)}, \tag{2.28a}$$

$$\mathbf{c}_2^{(1,2)} = \frac{c_2}{2G_2(1+\nu_2)}\mathbf{k}_2^{(1,2)}, \tag{2.28b}$$

$$\mathbf{c}_2^{(2,1)} = \frac{c_2}{2G_2(1+\nu_2)}\mathbf{k}_2^{(2,1)}, \tag{2.28c}$$

$$\mathbf{c}_2^{(2,2)} = \frac{c_2}{2G_2(1+\nu_2)}\mathbf{k}_2^{(2,2)}. \tag{2.28d}$$

It can be seen by Equations (2.27a) – (2.28d) that the differential damping operator in each region is proportional to the differential stiffness operator in each region. The proportionality constants for each region are defined as μ_1 and μ_2, respectively, and are identified as

$$\mu_1 = \frac{c_1}{E_1} = \frac{c_1}{2G_1(1+\nu_1)}, \tag{2.29a}$$

$$\mu_2 = \frac{c_2}{2G_2(1+\nu_2)}. \tag{2.29b}$$

This makes physical sense, as the system is macroscopically isotropic, and therefore the coefficients associated with the damping on the fibrils caused by the fluid medium are naturally proportional to the elastic parameters at each point in the vitreous continuum.

The boundary conditions for Region S_1 are similarly obtained from the variational principle, Equation (2.18), and take the form

$$u_1^{(n)} = 0 \qquad \text{on } C_1 \text{ in } S_1, \tag{2.30a}$$

$$u_1^{(t)} = 0 \qquad \text{on } C_1 \text{ in } S_1, \tag{2.30b}$$

$$u_1^{(n)} = 0 \qquad \text{on } C_2 \text{ in } S_1, \tag{2.31a}$$

$$u_1^{(t)} = 0 \qquad \text{on } C_2 \text{ in } S_1, \tag{2.31b}$$

$$u_1^{(n)} = 0 \qquad \text{on } C_3 \text{ in } S_1, \tag{2.32a}$$

$$u_1^{(t)} = 0 \qquad \text{on } C_3 \text{ in } S_1, \tag{2.32b}$$

where $u_1^{(n)}$ and $u_1^{(t)}$ represent the displacements normal to and tangential to the boundaries, respectively. Since the components of the displacement of the vitreous in both the normal and tangential directions vanish in Region S_1, we can restate these boundary conditions as follows

$$u_1 = 0 \qquad \text{on } C_1 \text{ in } S_1, \tag{2.30a$'$}$$

$$v_1 = 0 \qquad \text{on } C_1 \text{ in } S_1, \tag{2.30b$'$}$$

$$u_1 = 0 \qquad \text{on } C_2 \text{ in } S_1, \tag{2.31a$'$}$$

$$v_1 = 0 \qquad \text{on } C_2 \text{ in } S_1, \tag{2.31b$'$}$$

$$u_1 = 0 \qquad \text{on } C_3 \text{ in } S_1, \tag{2.32a$'$}$$

$$v_1 = 0 \qquad \text{on } C_3 \text{ in } S_1. \tag{2.32b$'$}$$

Likewise, the matching boundary conditions across C_4, the propagating boundary between the two regions, are obtained and take the form

$$u_1 = u_2 \qquad \text{on } C_4, \tag{2.33a}$$

$$v_1 = v_2 \qquad \text{on } C_4, \tag{2.33b}$$

$$\sigma_{r\phi}^{(T;1)} = \sigma_{r\phi}^{(T;2)} \qquad \text{on } C_4, \tag{2.33c}$$

$$u_1 = 0 \qquad \text{on } C_4. \tag{2.33d}$$

Finally, the boundary conditions for Region S_2 on the boundaries C_2 and C_3 are as follows

$$\sigma_{nt}^{(T;2)} = 0 \qquad \text{on } C_2 \text{ in } S_2, \tag{2.34}$$

$$\sigma_{nt}^{(T;2)} = 0 \qquad \text{on } C_3 \text{ in } S_2, \tag{2.35}$$

where $\sigma_{nt}^{(T;2)}$ represents the components of the total stress tangential to the boundary. Since normal stress vanishes by definition in Region S_2, Equations (2.34) and (2.35) reduce to

$$\sigma_{r\phi}^{(T;2)} = 0 \qquad \text{on } C_2 \text{ in } S_2. \tag{2.34$'$}$$

$$\sigma_{r\phi}^{(T;2)} = 0 \qquad \text{on } C_3 \text{ in } S_2, \tag{2.35$'$}$$

respectively. There is also an additional boundary condition on boundaries C_2 and C_3 in Region S_2 that states that the normal stress is equal to the IOP of the vitreous. This pressure will not cause deformation of the retina because the stress is balanced by equal stress on the outside of the retina from the choroid. The choroid is a highly vascular tissue, and the blood pressure that flows through it is equivalent to the IOP inside the vitreous cavity [7].

As previously stated, the boundary points a and b along C_2 and C_3, respectively, are not stationary, but rather are allowed to evolve causing C_4 to recede. The model assumes symmetric detachment meaning boundary C_4 is at a uniform radius, R_d, from the origin. This implies that points a and b detach at the same rate. The variations of these parameters are related in the following way

$$\delta R_d = \left[\delta a \ \vec{e}_t \cdot -\vec{e}_r\right]\big|_a = \left[\delta b \ \vec{e}_t \cdot -\vec{e}_r\right]\big|_b , \tag{2.36}$$

where $\vec{e}_t$ is the unit vector tangent to the boundary C_2 or C_3, and $\vec{e}_r$ is the unit vector in the radial direction. Allowing for variation of these points yields a transversality condition, which governs the location of the boundary C_4 at $r = R_d$, and thus of points a and b. The resulting condition takes the following form

$$\mathcal{G}\{R_d; a, b\} = 2\gamma\big|_a + 2\gamma\big|_b \tag{2.37}$$

where $\mathcal{G}\{R_d; a, b\}$ is identified as the energy release rate per unit depth of the detaching vitreous. This is the energy per unit depth released per unit increase of detachment area.

The explicit form of $\mathcal{G}$ is found to be

$$\begin{aligned}
\mathcal{G}\{R_d; a, b\} = &\left\{ \frac{1}{2} \left[\sigma_{rr}^{(T;1)} \varepsilon_{rr}^{(1)} + \sigma_{\phi\phi}^{(T;1)} \varepsilon_{\phi\phi}^{(1)} + 2 \left(\sigma_{r\phi}^{(T;1)} \varepsilon_{r\phi}^{(1)} - \sigma_{r\phi}^{(T;2)} \varepsilon_{r\phi}^{(2)} \right) \right] - \sigma_{nt}^{(T;1)} \frac{\partial u_1^{(t)}}{\partial s} \right. \\
&+ \sigma_{nt}^{(T;2)} \frac{\partial u_2^{(t)}}{\partial s} - \frac{\rho_1}{2} \left[\left(\frac{\partial u_1}{\partial t} + \frac{\partial u_o}{\partial t} \frac{d_0 \sin\phi}{\sqrt{r^2 + d_0^2 - 2rd_0 \cos\phi}} \right)^2 \right. \\
&\left. + \left(\frac{\partial v_1}{\partial t} + \frac{\partial u_o}{\partial t} \frac{r - d_0 \cos\phi}{\sqrt{r^2 + d_0^2 - 2rd_0 \cos\phi}} \right)^2 \right] \\
&+ \frac{\rho_2}{2} \left[\left(\frac{\partial u_2}{\partial t} + \frac{\partial u_o}{\partial t} \frac{d_0 \sin\phi}{\sqrt{r^2 + d_0^2 - 2rd_0 \cos\phi}} \right)^2 \right. \\
&\left.\left. + \left(\frac{\partial v_2}{\partial t} + \frac{\partial u_o}{\partial t} \frac{r - d_0 \cos\phi}{\sqrt{r^2 + d_0^2 - 2rd_0 \cos\phi}} \right)^2 \right] \right\} \Bigg|_a \\
+ &\left\{ \frac{1}{2} \left[\sigma_{rr}^{(T;1)} \varepsilon_{rr}^{(1)} + \sigma_{\phi\phi}^{(T;1)} \varepsilon_{\phi\phi}^{(1)} + 2 \left(\sigma_{r\phi}^{(T;1)} \varepsilon_{r\phi}^{(1)} - \sigma_{r\phi}^{(T;2)} \varepsilon_{r\phi}^{(2)} \right) \right] - \sigma_{nt}^{(T;1)} \frac{\partial u_1^{(t)}}{\partial s} \right. \qquad (2.38) \\
&+ \sigma_{nt}^{(T;2)} \frac{\partial u_2^{(t)}}{\partial s} - \frac{\rho_1}{2} \left[\left(\frac{\partial u_1}{\partial t} + \frac{\partial u_o}{\partial t} \frac{d_0 \sin\phi}{\sqrt{r^2 + d_0^2 - 2rd_0 \cos\phi}} \right)^2 \right. \\
&\left. + \left(\frac{\partial v_1}{\partial t} + \frac{\partial u_o}{\partial t} \frac{r - d_0 \cos\phi}{\sqrt{r^2 + d_0^2 - 2rd_0 \cos\phi}} \right)^2 \right] \\
&+ \frac{\rho_2}{2} \left[\left(\frac{\partial u_2}{\partial t} + \frac{\partial u_o}{\partial t} \frac{d_0 \sin\phi}{\sqrt{r^2 + d_0^2 - 2rd_0 \cos\phi}} \right)^2 \right. \\
&\left.\left. + \left(\frac{\partial v_2}{\partial t} + \frac{\partial u_o}{\partial t} \frac{r - d_0 \cos\phi}{\sqrt{r^2 + d_0^2 - 2rd_0 \cos\phi}} \right)^2 \right] \right\} \Bigg|_b \\
&+ [\vec{e}_t \cdot -\vec{e}_r]|_{(a \text{ or } b)} \int_{C_4} \sigma_{rr}^{(T;1)} \frac{\partial u_1}{\partial r} ds
\end{aligned}$$

where s is the path coordinate along boundary C_4.

Detachment progression will be based upon a Griffith-type detachment criterion [25]. If the energy release rate per unit depth gets large enough such that $\mathcal{G}\{a; b; R_d\} \geq 2\gamma|_a + 2\gamma|_b$, the detachment will propagate until the inequality no longer holds. The boundaries will remain fixed when $\mathcal{G}\{R_d; a, b\} < 2\gamma|_a + 2\gamma|_b$.

To summarize, the motion of the vitreous is Regions S_1 as S_2 are determined as solutions to the propagating boundary value problem with governing equations formally stated by Equations (2.19a) and (2.19b), and boundary conditions given by Equations (2.30a′), (2.30b′), (2.31a′), (2.31b′), (2.32a′), (2.32b′), (2.33a), (2.33b), (2.33c), (2.33d), (2.34′), and (2.35′). In addition, the locations of the point of detachment of the vitreous cortex from the sensory retina are determined by the transversality condition given by Equation (2.37). The next two chapters in this dissertation are concerned with solving this propagating boundary value problem, and analyzing the results, first for purely circumferential displacement, and second for full two-dimensional motion.

Chapter 3

Constrained 2D Model

As discussed in Chapter 1, it is widely believed that the separation of liquid from the gel-like vitreous initiates the onset of PVD. (See, for example, Foos and Wheeler (1982) [20] and Sebag (1987) [44].) This syneresis implies that some fibrils in the gel-like vitreous have attached themselves in an anteroposterior orientation [44]. The effect of these fibril chains can be incorporated into the model by imposing a constraint on the motion of the vitreous in the r-direction. Furthermore, the rotation of the eye is about its geometric center, and therefore it may be anticipated that the dominant motion of the vitreous in response to a single saccade will be in the ϕ-direction. Thus in this chapter, the simplifying assumption is made that displacement of the vitreous in the r-direction can be neglected when compared with that in the ϕ-direction.

3.1 Constraint on Motion

By neglecting the radial components of displacement, the motion of the vitreous is effectively constrained in the radial direction. The problem is formulated as a constrained problem to characterize the body force necessary to restrain the deformation. In doing so, this inherent constraining force serves as a relative measure of the omission of radial displacement.

This constraint is handled formally by amending the action integral per unit depth, Π, given by Equation (2.11), to include a constraint functional, Λ, which restricts displacement in the r-direction. The total potential energy functional per unit depth becomes

$$\Pi = \mathcal{T}^{(1)} + \mathcal{T}^{(2)} - \mathcal{U}^{(1)} - \mathcal{U}^{(2)} + \mathcal{W}_V^{(1)} + \mathcal{W}_V^{(2)} - \mathcal{E}_F - \Lambda, \tag{3.1}$$

where

$$\Lambda = \Lambda^{(1)} + \Lambda^{(2)} = \iint\limits_{A_1} \lambda_1 u_1 dA + \iint\limits_{A_2} \lambda_2 u_2 dA, \tag{3.2}$$

where the Lagrange multipliers λ_1 and λ_2 represent the force per unit volume (i.e. body force) in Region S_1 and Region S_2, respectively, that constrains the displacement in the r-direction. All other parameters in Equation (3.1) remain unchanged.

Invoking Hamilton's Principle for the constrained problem yields a self-consistent set of governing equations of motion, external boundary conditions, matching boundary conditions, transversality conditions to locate boundaries a and b, as well as differential constraint equations that determine λ_1 and λ_2.

Substitution of Equation (3.1) into Equation (2.18), and performing the variations yields the formal statement of constraint on displacement, namely

$$u_1 \equiv 0, \tag{3.3a}$$

$$u_2 \equiv 0. \tag{3.3b}$$

The governing equations of motion are likewise obtained and take the forms

$$\begin{aligned}\rho_1 \frac{\partial^2 v_1}{\partial t^2} &+ \mu_1 G_1 \left[-\frac{2(1-\nu_1)}{1-2\nu_1}\frac{1}{r^2}\frac{\partial^2}{\partial \phi^2} - \frac{\partial^2}{\partial r^2} - \frac{1}{r}\frac{\partial}{\partial r} + \frac{1}{r^2}\right]\frac{\partial v_1}{\partial t} \\ &+ G_1 \left[-\frac{2(1-\nu_1)}{1-2\nu_1}\frac{1}{r^2}\frac{\partial^2}{\partial \phi^2} - \frac{\partial^2}{\partial r^2} - \frac{1}{r}\frac{\partial}{\partial r} + \frac{1}{r^2}\right] v_1 \\ &= -\frac{\rho_1 \left(r - d_0\cos\phi\right)}{\sqrt{r^2 + d_0^2 - 2rd_0\cos\phi}}\frac{\partial^2 u_o}{\partial t^2},\end{aligned} \tag{3.4a}$$

$$\begin{aligned}\rho_2 \frac{\partial^2 v_2}{\partial t^2} - \mu_2 G_2 \left[\frac{\partial^2}{\partial r^2} + \frac{1}{r}\frac{\partial}{\partial r} - \frac{1}{r^2}\right]\frac{\partial v_2}{\partial t} - G_2\left[\frac{\partial^2}{\partial r^2} + \frac{1}{r}\frac{\partial}{\partial r} - \frac{1}{r^2}\right] v_2 \\ = -\frac{\rho_2 \left(r - d_0\cos\phi\right)}{\sqrt{r^2 + d_0^2 - 2rd_0\cos\phi}}\frac{\partial^2 u_o}{\partial t^2}.\end{aligned} \tag{3.4b}$$

The boundary conditions in Region S_1 follow as

$$v_1 = 0 \qquad \text{on } C_1 \text{ in } S_1, \tag{3.5a}$$

$$v_1 = 0 \qquad \text{on } C_2 \text{ in } S_1, \tag{3.5b}$$

$$v_1 = 0 \qquad \text{on } C_3 \text{ in } S_1, \tag{3.5c}$$

Likewise, the matching boundary conditions across C_4, the propagating boundary between the two regions, are obtained and take the form

$$v_1 = v_2 \qquad \text{on } C_4, \tag{3.6a}$$

$$\sigma_{r\phi}^{(T;1)} = \sigma_{r\phi}^{(T;2)} \qquad \text{on } C_4. \tag{3.6b}$$

Finally, the boundary conditions for Region S_2 on the boundaries C_2 and C_3 are as follows

$$\sigma_{nt}^{(T;2)} = 0 \qquad \text{on } C_2 \text{ in } S_2, \tag{3.7}$$

$$\sigma_{nt}^{(T;2)} = 0 \qquad \text{on } C_2 \text{ in } S_2. \tag{3.8}$$

Since normal stress vanishes by definition in Region S_2, Equations (3.7) and (3.8) reduce to

$$\sigma_{r\phi}^{(T;2)} = 0 \qquad \text{on } C_2 \text{ in } S_2, \tag{3.7$'$}$$

$$\sigma_{r\phi}^{(T;2)} = 0 \qquad \text{on } C_3 \text{ in } S_2, \tag{3.8$'$}$$

respectively.

In addition, the differential constraint equations are

$$\begin{aligned}\lambda_1 = {} & \frac{\mu_1 G_1}{1-2\nu_1}\frac{1}{r}\left[(3-4\nu_1)\frac{1}{r}\frac{\partial}{\partial\phi} - \frac{\partial^2}{\partial r\partial\phi}\right]\frac{\partial v_1}{\partial t} \\ & + \frac{G_1}{1-2\nu_1}\frac{1}{r}\left[(3-4\nu_1)\frac{1}{r}\frac{\partial}{\partial\phi} - \frac{\partial^2}{\partial r\partial\phi}\right]v_1 + \frac{\rho_1 d_0 \sin\phi}{\sqrt{r^2+d_0^2-2rd_0\cos\phi}}\frac{\partial^2 u_o}{\partial t^2},\end{aligned} \tag{3.9a}$$

$$\begin{aligned}\lambda_2 = {} & \frac{\mu_2 G_2}{r^2}\left(\frac{\partial^2}{\partial r\partial\phi} - \frac{\partial}{\partial\phi}\right)\frac{\partial v_2}{\partial t} \\ & + \frac{G_2}{r^2}\left(\frac{\partial^2}{\partial r\partial\phi} - \frac{\partial}{\partial\phi}\right)v_2 + \frac{\rho_2 d_0 \sin\phi}{\sqrt{r^2+d_0^2-2rd_0\cos\phi}}\frac{\partial^2 u_o}{\partial t^2}.\end{aligned} \tag{3.9b}$$

Equations (3.9a) and (3.9b) are used to determine λ_1 and λ_2 once the governing equations of motion, Equations (3.4a) and (3.4b), have been solved for v_1 and v_2.

The transversality condition, which governs the location of points a and b take the same general form as the unconstrained equation. That is

$$\mathcal{G}\{R_d; a, b\} = 2\gamma\big|_a + 2\gamma\big|_b\,. \tag{3.10}$$

However, the energy release rate per unit depth term, $\mathcal{G}\{R_d; a, b\}$, now reduces to the following form

$$
\begin{aligned}
\mathcal{G}\{R_d; a, b\} = & \left\{ \frac{1}{2} \left[\sigma_{\phi\phi}^{(T;1)} \varepsilon_{\phi\phi}^{(1)} + 2 \left(\sigma_{r\phi}^{(T;1)} \varepsilon_{r\phi}^{(1)} - \sigma_{r\phi}^{(T;2)} \varepsilon_{r\phi}^{(2)} \right) \right] - \sigma_{nt}^{(T;1)} \frac{\partial u_1^{(t)}}{\partial s} + \sigma_{nt}^{(T;2)} \frac{\partial u_2^{(t)}}{\partial s} \right. \\
& - \frac{\rho_1}{2} \left[\left(\frac{\partial u_o}{\partial t} \frac{d_0 \sin\phi}{\sqrt{r^2 + d_0^2 - 2rd_0 \cos\phi}} \right)^2 + \left(\frac{\partial v_1}{\partial t} + \frac{\partial u_o}{\partial t} \frac{r - d_0 \cos\phi}{\sqrt{r^2 + d_0^2 - 2rd_0 \cos\phi}} \right)^2 \right] \\
& \left. + \frac{\rho_2}{2} \left[\left(\frac{\partial u_o}{\partial t} \frac{d_0 \sin\phi}{\sqrt{r^2 + d_0^2 - 2rd_0 \cos\phi}} \right)^2 + \left(\frac{\partial v_2}{\partial t} + \frac{\partial u_o}{\partial t} \frac{r - d_0 \cos\phi}{\sqrt{r^2 + d_0^2 - 2rd_0 \cos\phi}} \right)^2 \right] \right\} \Bigg|_a \\
& + \left\{ \frac{1}{2} \left[\sigma_{\phi\phi}^{(T;1)} \varepsilon_{\phi\phi}^{(1)} + 2 \left(\sigma_{r\phi}^{(T;1)} \varepsilon_{r\phi}^{(1)} - \sigma_{r\phi}^{(T;2)} \varepsilon_{r\phi}^{(2)} \right) \right] - \sigma_{nt}^{(T;1)} \frac{\partial u_1^{(t)}}{\partial s} + \sigma_{nt}^{(T;2)} \frac{\partial u_2^{(t)}}{\partial s} \right. \\
& - \frac{\rho_1}{2} \left[\left(\frac{\partial u_o}{\partial t} \frac{d_0 \sin\phi}{\sqrt{r^2 + d_0^2 - 2rd_0 \cos\phi}} \right)^2 + \left(\frac{\partial v_1}{\partial t} + \frac{\partial u_o}{\partial t} \frac{r - d_0 \cos\phi}{\sqrt{r^2 + d_0^2 - 2rd_0 \cos\phi}} \right)^2 \right] \\
& \left. + \frac{\rho_2}{2} \left[\left(\frac{\partial u_o}{\partial t} \frac{d_0 \sin\phi}{\sqrt{r^2 + d_0^2 - 2rd_0 \cos\phi}} \right)^2 + \left(\frac{\partial v_2}{\partial t} + \frac{\partial u_o}{\partial t} \frac{r - d_0 \cos\phi}{\sqrt{r^2 + d_0^2 - 2rd_0 \cos\phi}} \right)^2 \right] \right\} \Bigg|_b .
\end{aligned}
\tag{3.11}
$$

If the energy release rate per unit depth gets large enough such that $\mathcal{G}\{R_d; a, b\} \geq 2\gamma|_a + 2\gamma|_b$, the detachment will propagate until the inequality no longer holds. The boundaries will remain fixed when $\mathcal{G}\{R_d; a, b\} < 2\gamma|_a + 2\gamma|_b$.

3.2 Solution Procedure

The mathematical problem is formally stated by Equations (3.4a), (3.4b), (3.5a), (3.5b), (3.5c), (3.6a), (3.6b), (3.7′), (3.8′), (3.9a), (3.9b), (3.10), and (3.11). These equations represent a forced vibration problem for a composite domain with an internal boundary whose location is to be determined as part of the solution. This problem will be solved via modal analysis. Since the damping operator is proportional to the stiffness operator, the vitreous is subject to Rayleigh damping, which allows the forced vibration solution to be expressed as a linear combination of the undamped free vibration modes. (See, for example, Bottega (2015) [15].)

3.2.1 Undamped Free Vibration Analysis

The undamped free vibration problem is obtained by removing the forcing function and damping operator from Equations (3.4a) and (3.4b). The corresponding equations of motion take the following form

$$\rho_1 \frac{\partial^2 v_1}{\partial t^2} + G_1 \left[-\frac{2(1-\nu_1)}{1-2\nu_1} \frac{1}{r^2} \frac{\partial^2}{\partial \phi^2} - \frac{\partial^2}{\partial r^2} - \frac{1}{r}\frac{\partial}{\partial r} + \frac{1}{r^2} \right] v_1 = 0, \tag{3.12a}$$

$$\rho_2 \frac{\partial^2 v_2}{\partial t^2} + G_2 \left[-\frac{\partial^2}{\partial r^2} - \frac{1}{r}\frac{\partial}{\partial r} + \frac{1}{r^2} \right] v_2 = 0. \tag{3.12b}$$

The above form does not admit a separable solution in its current form, as boundaries C_2 and C_3 are neither constant-r nor constant-ϕ boundaries. The problem is therefore transformed to a new domain where the ϕ-coordinate is mapped to a new coordinate ϕ^* in the following way

$$\phi^* = \begin{cases} \phi, & 0 < r < \sqrt{1-d_0^2} \\ \dfrac{\pi/2}{\cos^{-1}\left(\frac{r^2+d_0^2-1}{2rd_0}\right)}\phi, & \sqrt{1-d_0^2} < r < 1+d_0^2 \end{cases}. \tag{3.13}$$

The governing equations and boundary conditions are transformed accordingly, and take the form

$$\rho_1 \frac{\partial^2 v_1}{\partial t^2} + G_1 \left[-\frac{2(1-\nu_1)}{1-2\nu_1} \left(\frac{\cos^{-1}\left(\frac{r^2+d_0^2-1}{2rd_0}\right)}{\pi/2} \right)^2 \frac{1}{r^2} \frac{\partial^2}{\partial \phi^{*2}} - \frac{\partial^2}{\partial r^2} - \frac{1}{r}\frac{\partial}{\partial r} + \frac{1}{r^2} \right] v_1 = 0, \tag{3.14a}$$

$$\rho_2 \frac{\partial^2 v_2}{\partial t^2} + G_2 \left[-\frac{\partial^2}{\partial r^2} - \frac{1}{r}\frac{\partial}{\partial r} + \frac{1}{r^2} \right] v_2 = 0. \tag{3.14b}$$

The transformed boundary value problem admits separable solutions. A solution is found in the (r, ϕ^*) domain, and is then transformed back into the original (r, ϕ) domain. The solution is of the form

$$v_1(r, \phi, t) = \sum_{n=1}^{\infty} \sum_{j=1}^{\infty} C^{(nj)} V_1^{(nj)}(r, \phi) e^{i\omega^{(nj)} t}, \tag{3.15a}$$

$$v_2(r, \phi, t) = \sum_{n=1}^{\infty} \sum_{j=1}^{\infty} C^{(nj)} V_2^{(nj)}(r, \phi) e^{i\omega^{(nj)} t}. \tag{3.15b}$$

where the modal functions are found to be

$$V_1^{(nj)}(r,\phi) = \begin{cases} J_{\xi^{(n)}}\left(\alpha_1^{(nj)} r\right)\cos(n\phi^*) & (n \sim \text{odd};\ j=1,2,3,...) \\ J_{\xi^{(n)}}\left(\alpha_1^{(nj)} r\right)\sin(n\phi^*) & (n \sim \text{even};\ j=1,2,3,...) \end{cases} \tag{3.16a}$$

$$V_2^{(nj)}(r,\phi) = \begin{cases} T^{(nj)}\left[J_1\left(\alpha_2^{(nj)} r\right) - S^{(nj)} Y_1\left(\alpha_2^{(nj)} r\right)\right]\cos(n\phi^*) & (n \sim \text{odd};\ j=1,2,3,...) \\ T^{(nj)}\left[J_1\left(\alpha_2^{(nj)} r\right) - S^{(nj)} Y_1\left(\alpha_2^{(nj)} r\right)\right]\sin(n\phi^*) & (n \sim \text{even};\ j=1,2,3,...). \end{cases} \tag{3.16b}$$

The modes corresponding to $n \sim$ odd (i.e. $n = 1,3,5,...$) are symmetric about $\phi = 0$ in the ϕ-direction and the modes corresponding to $n \sim$ even (i.e. $n = 2,4,6,...$) are anti-symmetric about $\phi = 0$ in the ϕ-direction. This means that for symmetric modes $V^{(nj)}(r_0,\phi_0) = V^{(nj)}(r_0,-\phi_0)$, and for anti-symmetric modes $V^{(nj)}(r_0,\phi_0) = -V^{(nj)}(r_0,-\phi_0)$, where (r_0,ϕ_0) are arbitrary points in the vitreous. Moreover, $C^{(nj)}$ are arbitrary constants that satisfy initial conditions, and J_i and Y_i are Bessel functions of the first and second kind, respectively, of order i. The order of the Bessel function in Region S_1 is unique for each mode, and is given by

$$\xi^{(n)} = \sqrt{1 + \frac{2(1-\nu_1)}{1-2\nu_1} n^2} \qquad (n = 1,2,3,...)\,. \tag{3.17}$$

The radial wave number, $\alpha_k^{(nj)}$ $(k = 1,2)$ in each region associated with each mode is related to the natural frequency, $\omega^{(nj)}$, of the given mode as

$$\alpha_1^{(nj)} = \frac{\omega^{(nj)}}{\sqrt{G_1/\rho_1}} \qquad (n,j = 1,2,3,...)\,, \tag{3.18a}$$

$$\alpha_2^{(nj)} = \frac{\omega^{(nj)}}{\sqrt{G_2/\rho_2}} \qquad (n,j = 1,2,3,...)\,. \tag{3.18b}$$

The remaining terms in Equations (3.16a) and (3.16b) are defined as follows

$$S^{(nj)} = \frac{J_1\left(\alpha_2^{(nj)} R_d\right)}{Y_1\left(\alpha_2^{(nj)} R_d\right)} \qquad (n,j = 1,2,3,...)\,, \tag{3.19a}$$

$$T^{(nj)} = \frac{J_{\xi^{(n)}}\left[\alpha_1^{(nj)}(R+d_0)\right]}{J_1\left[\alpha_2^{(nj)}(R+d_0)\right] - S^{(nj)} Y_1\left[\alpha_2^{(nj)}(R+d_0)\right]} \qquad (n,j = 1,2,3,...)\,. \tag{3.19b}$$

Substitution of Equations (3.15a) and (3.15b) into the remaining boundary condition, the balance of shear stress along boundary C_4 given by Equation (3.6b), yields the frequency equation for the nj^{th} mode given by

$$G_1\left\{\frac{\alpha_1^{(nj)}}{2}\left[J_{\xi^{(n)}-1}\left(\alpha_1^{(nj)}R_d\right)-J_{\xi^{(n)}+1}\left(\alpha_1^{(nj)}R_d\right)\right]-\frac{1}{R_d}J_{\xi^{(nj)}}\left(\alpha_1^{(nj)}R_d\right)\right\}$$
$$=G_2T^{(nj)}\left\{\frac{\alpha_2^{(nj)}}{2}\left[J_0\left(\alpha_2^{(nj)}R_d\right)-J_2\left(\alpha_2^{(nj)}R_d\right)\right]-\frac{1}{R_d}J_1\left(\alpha_2^{(nj)}R_d\right)\right.$$
$$\left.-S^{(nj)}\frac{\alpha_2^{(nj)}}{2}\left[Y_0\left(\alpha_2^{(nj)}R_d\right)-Y_2\left(\alpha_2^{(nj)}R_d\right)\right]+S^{(nj)}\frac{1}{R_d}J_1\left(\alpha_2^{(nj)}R_d\right)\right\}. \tag{3.20}$$

The natural frequency, $\omega^{(nj)}$, for each mode corresponds to a root of the frequency equation, Equation (3.20). Each frequency is determined numerically using root solving techniques.

3.2.2 Modal Analysis

The free vibration modes for vanishing damping are given by Equations (3.16a) and (3.16b), with the corresponding natural frequencies determined by Equation (3.20). Any two vibration modes are mutually orthogonal with respect to one another if they satisfy the following condition

$$\iint\limits_{A_1}[V_1^{(nj)}\mathbf{k}_1^{(2,2)}V_1^{(lp)}-V_1^{(lp)}\mathbf{k}_1^{(2,2)}V_1^{(nj)}]dA+\iint\limits_{A_2}[V_2^{(nj)}\mathbf{k}_2^{(2,2)}V_2^{(lp)}-V_2^{(lp)}\mathbf{k}_2^{(2,2)}V_2^{(nj)}]dA=0, \tag{3.21}$$

where $\mathbf{k}_1^{(2,2)}$ and $\mathbf{k}_2^{(2,2)}$ are given by Equations (2.25d) and (2.26d), respectively, and correspond to the stiffness operators of the free vibration equations given by Equations (3.12a) and (3.12b). It can be shown that Equations (3.16a) and (3.16b) satisfy Equation (3.21), proving that all the vibration modes are mutually orthogonal. Therefore, the modes provide an orthogonal basis on which the solution to Equations (3.4a) and (3.4b), the damped forced vibration problem, can be expressed. The solution will be of the form

$$v_1(r,\phi,t)=\sum_{n=1}^{\infty}\sum_{j=1}^{\infty}V_1^{(nj)}(r,\phi)\eta^{(nj)}(t), \tag{3.22a}$$

$$v_2(r,\phi,t)=\sum_{n=1}^{\infty}\sum_{j=1}^{\infty}V_2^{(nj)}(r,\phi)\eta^{(nj)}(t), \tag{3.22b}$$

where $\eta^{(nj)}(t)$ represents the modal coordinates. Substitution of Equations (3.22a) and (3.22b) into Equations (3.4a) and (3.4b), while exploiting the mutual orthogonality of the modes, reduces the system of coupled partial differential equations to one of uncoupled ordinary differential equations, one for each mode. The modal equations take the form

$$\tilde{m}^{(nj)}\ddot{\eta}(t) + \tilde{c}^{(nj)}\dot{\eta}(t) + \tilde{k}^{(nj)}\eta(t) = \tilde{F}^{(nj)}(t) \qquad (n, j = 1, 2, 3, ...)\,, \tag{3.23}$$

where

$$\tilde{m}^{(nj)} = \iint\limits_{A_1} V_1^{(nj)}(r,\phi)\rho_1 V_1^{(nj)}(r,\phi)dA + \iint\limits_{A_2} V_2^{(nj)}(r,\phi)\rho_2 V_2^{(nj)}(r,\phi)dA \tag{3.24a}$$

is the modal mass operator for the nj^{th} mode,

$$\begin{aligned}\tilde{k}^{(nj)} &= \iint\limits_{A_1} V_1^{(nj)}(r,\phi)G_1\left[-\frac{2(1-\nu_1)}{1-2\nu_1}\frac{1}{r^2}\frac{\partial^2}{\partial\phi^2} - \frac{\partial^2}{\partial r^2} - \frac{1}{r}\frac{\partial}{\partial r} + \frac{1}{r^2}\right]V_1^{(nj)}(r,\phi)dA \\ &\quad + \iint\limits_{A_2} V_2^{(nj)}(r,\phi)G_2\left[-\frac{\partial^2}{\partial r^2} - \frac{1}{r}\frac{\partial}{\partial r} + \frac{1}{r^2}\right]V_2^{(nj)}(r,\phi)dA \\ &= \tilde{k}_1^{(nj)} + \tilde{k}_2^{(nj)} \\ &= {\omega^{(nj)}}^2\tilde{m}^{(nj)}\end{aligned} \tag{3.24b}$$

is the modal stiffness operator for the nj^{th} mode,

$$\begin{aligned}\tilde{c}^{(nj)} &= \iint\limits_{A_1} V_1^{(nj)}(r,\phi)\mu_1 G_1\left[-\frac{2(1-\nu_1)}{1-2\nu_1}\frac{1}{r^2}\frac{\partial^2}{\partial\phi^2} - \frac{\partial^2}{\partial r^2} - \frac{1}{r}\frac{\partial}{\partial r} + \frac{1}{r^2}\right]V_1^{(nj)}(r,\phi)dA \\ &\quad + \iint\limits_{A_2} V_2^{(nj)}(r,\phi)\mu_2 G_2\left[-\frac{\partial^2}{\partial r^2} - \frac{1}{r}\frac{\partial}{\partial r} + \frac{1}{r^2}\right]V_2^{(nj)}(r,\phi)dA \\ &= \mu_1\tilde{k}_1^{(nj)} + \mu_2\tilde{k}_2^{(nj)}\end{aligned} \tag{3.24c}$$

is the modal damping operator for the nj^{th} mode, and

$$\begin{aligned}\tilde{F}^{(nj)} &= -\iint\limits_{A_1} \frac{\rho_1(r-d_0\cos\phi)}{\sqrt{r^2+d_0^2-2rd_0\cos\phi}}\ddot{u}_o V_1^{(nj)}(r,\phi)dA \\ &\quad -\iint\limits_{A_2} \frac{\rho_2(r-d_0\cos\phi)}{\sqrt{r^2+d_0^2-2rd_0\cos\phi}}\ddot{u}_o V_2^{(nj)}(r,\phi)dA\end{aligned} \tag{3.24d}$$

is the modal force for the nj^{th} mode.

The solution to Equation (3.23) depends on whether the particular mode is overdamped or underdamped. Depending on the values chosen for μ_1 and μ_2, some modes may be overdamped while others are underdamped. For an overdamped modal coordinate, $\eta^{(nj)}(t)$ is expressed as the solution of a convolution integral in the form

$$\eta^{(nj)}(t) = -\int_0^t \left(a_0^{(nj)} + a_1^{(nj)}\tau + a_2^{(nj)}\tau^2 + a_3^{(nj)}\tau^3\right) e^{-\zeta^{(nj)}\omega^{(nj)}(t-\tau)} \frac{\sinh\left[\omega^{(nj)}z^{(nj)}\,(t-\tau)\right]}{\tilde{m}^{(nj)}\omega^{(nj)}\tilde{z}^{(nj)}} d\tau$$
$$-\int_{t-t_s}^{t} \left[a_0^{(nj)} + a_1^{(nj)}\,(t-\tau) + a_2^{(nj)}\,(t-\tau)^2 + a_3^{(nj)}\,(t-\tau)^3\right] e^{-\zeta^{(nj)}\omega^{(nj)}\tau} \frac{\sinh\left(\omega^{(nj)}z^{(nj)}\tau\right)}{\tilde{m}^{(nj)}\omega^{(nj)}\tilde{z}^{(nj)}} d\tau, \tag{3.25}$$

where

$$a_0^{(nj)} = -2c_2\left[\iint_{A_1} \frac{\rho_1(r-d_0\cos\phi)V_1^{(nj)}}{\sqrt{r^2+d_0^2-2rd_0\cos\phi}} dA + \iint_{A_2} \frac{\rho_2(r-d_0\cos\phi)V_2^{(nj)}}{\sqrt{r^2+d_0^2-2rd_0\cos\phi}} dA\right], \tag{3.26a}$$

$$a_1^{(nj)} = -6c_3\left[\iint_{A_1} \frac{\rho_1(r-d_0\cos\phi)V_1^{(nj)}}{\sqrt{r^2+d_0^2-2rd_0\cos\phi}} dA + \iint_{A_2} \frac{\rho_2(r-d_0\cos\phi)V_2^{(nj)}}{\sqrt{r^2+d_0^2-2rd_0\cos\phi}} dA\right], \tag{3.26b}$$

$$a_2^{(nj)} = -12c_4\left[\iint_{A_1} \frac{\rho_1(r-d_0\cos\phi)V_1^{(nj)}}{\sqrt{r^2+d_0^2-2rd_0\cos\phi}} dA + \iint_{A_2} \frac{\rho_2(r-d_0\cos\phi)V_2^{(nj)}}{\sqrt{r^2+d_0^2-2rd_0\cos\phi}} dA\right], \tag{3.26c}$$

$$a_3^{(nj)} = -20c_5\left[\iint_{A_1} \frac{\rho_1(r-d_0\cos\phi)V_1^{(nj)}}{\sqrt{r^2+d_0^2-2rd_0\cos\phi}} dA + \iint_{A_2} \frac{\rho_2(r-d_0\cos\phi)V_2^{(nj)}}{\sqrt{r^2+d_0^2-2rd_0\cos\phi}} dA\right], \tag{3.26d}$$

$$\tilde{\zeta}^{(nj)} = \frac{\tilde{c}^{(nj)}}{2\omega^{(nj)}\tilde{m}^{(nj)}}, \tag{3.27a}$$

$$\tilde{z}^{(nj)} = \sqrt{\tilde{\zeta}^{(nj)\,2} - 1}. \tag{3.27b}$$

If, instead, the vibration mode of interest is underdamped, $\eta^{(nj)}(t)$ takes the form

$$\eta^{(nj)}(t) = -\int_0^t \left(a_0^{(nj)} + a_1^{(nj)}\tau + a_2^{(nj)}\tau^2 + a_3^{(nj)}\tau^3\right) e^{-\zeta^{(nj)}\omega^{(nj)}(t-\tau)} \frac{\sin\left[\omega_d^{(nj)}\,(t-\tau)\right]}{\tilde{m}^{(nj)}\omega_d^{(nj)}} d\tau$$
$$-\int_{t-t_s}^{t} \left[a_0^{(nj)} + a_1^{(nj)}\,(t-\tau) + a_2^{(nj)}\,(t-\tau)^2 + a_3^{(nj)}\,(t-\tau)^3\right] e^{-\zeta^{(nj)}\omega^{(nj)}\tau} \frac{\sin\left(\omega_d^{(nj)}\tau\right)}{\tilde{m}^{(nj)}\omega_d^{(nj)}} d\tau, \tag{3.28}$$

where

$$\omega_d^{(nj)} = \sqrt{1 - \tilde{\zeta}^{(nj)\,2}}. \tag{3.29}$$

The convolution integrals of Equations (3.25) and (3.28) are computed analytically. The solutions are not shown for brevity.

The displacement of the vitreous subject to saccadic motion can now be expressed analytically as a function of two spatial variables and time by Equations (3.22a) and (3.22b). Substitution of these solutions into the strain-displacement relations and constitutive equations will yield the strain and stress at every point in the vitreous at all instances of time during the saccade. Substitution of these equations into Equations (3.10) and (3.11) will determine the location of the detachment boundaries a, and b. From this, the evolving detachment behavior can be characterized.

3.3 Results and Discussion

Now that the solution has been determined for the circumferential motion model, attention is turned to analyzing these results for typical scenarios. Geometric and material properties are selected based on data available in the literature. Resultant displacement and stress fields are presented, in addition to a lengthy discussion of detachment behavior. Where there is ambiguity on material values, the results of parameter studies are presented to demonstrate how the parameters affect the overall results.

3.3.1 Selection of Geometric and Material Properties

As previously mentioned, length scales are normalized by the dimensional radius of the eye. Therefore, the results presented here are independent of the radius chosen. Wilkerson and Rice (1997) [49] show the distance from the geometric center of a typical human eye to the retinal wall as 11 mm, and the distance from the geometric center to the posterior portion of the lens as 4.8 mm. Hence, d_0, the normalized distance from the center of the eye to the lens is chosen as $d_0 = \frac{4.8 \text{ mm}}{11 \text{ mm}} = 0.436$. The maximum radius of Region S_2 is thus $R_0 = R + d_0 = 1.436$. Detachment size is quantified as the difference between R_0 and R_d, where R_d is the radius of Region S_1 as defined earlier.

Since water constitutes $98-99\%$ of the mass of the vitreous, both $\overline{\rho}_1$ and $\overline{\rho}_2$ are taken to be the same density as water, 1000 kg/m^3. Hence, $\rho_1 = \rho_2 = 1$. Furthermore, since water is nearly incompressible, Poisson's ratio is assumed the same for both regions, $\nu_1 = \nu_2 = 0.49$. It is again noted that the material differences between these two regions is accounted for by the constitutive relations given by Equations (2.4) and (2.5).

There is a large degree of difficulty in determining the rheological properties of the vitreous. In studies by Lee at al. (1992 and 1994) [34] [35], ex vivo rheological experiments are conducted on the vitreous of fresh bovine, porcine, and human eyes. The authors determine that the viscoelastic characteristics of the central porcine vitreous closely resemble those of the human vitreous. Due to the more readily available porcine eyes, most rheological experimentation going forward have been conducted on the central portion of the porcine vitreous. A further degree of uncertainty for rheological parameters is added by the fact that Zimberlin et al. (2010) [50] have experimentally demonstrated that the mechanical properties of the vitreous differ between *in vivo* measurements and *ex vivo* measurements. The shear modulus decreases when removed from the eye, and decreases further when the hyaloid membrane has been disrupted.

The values most commonly used in the literature are attributed to Nickerson et al. (2008) [39] and Swindle, Hamilton, and Ravi (2008) [48]. In both studies, the values of the dynamic shear moduli are determined by conducting an ex vivo oscillatory strain test of the central portion of porcine vitreous. Nickerson et al. conclude that the storage modulus is $\overline{G}^{'} = 10 \pm 1.9$ N/m^2, while the loss modulus is $\overline{G}^{''} = 3.9 \pm 0.8$ N/m^2. In contrast, Swindle, Hamilton, and Ravi conclude that the storage modulus is $\overline{G}^{'} = 3.46 \pm 0.30$ N/m^2, while the loss modulus is $\overline{G}^{''} = 0.71 \pm 0.12$ N/m^2. This work has been extended by Modarreszadeh and Abouali [38] to determine the complex shear modulus for finite non-linear deformation, which is not considered in the present study.

In the present study, the shear moduli for each region, G_1 and G_2, are akin to the storage moduli of these tests, while the proportionality constants in each region, μ_1 and μ_2, are determined from the loss moduli of these experiments. The present study adopts the values of the dynamic moduli determined by Nickerson et al. as they utilized a novel cleated rheometry fixture to correct for slippage at the boundary. However, a parameter study is performed later due to the large uncertainty surrounding these values, and the aforementioned difficulties in obtaining these properties. The values from Nickerson et al.

correspond to the present study as $\overline{G}_1 = \overline{G}_2 = 10$ N/m^2 and $\mu_1 = \mu_2 = 0.354$. Since $\overline{G}_1$ and $\overline{G}_2$ are both normalized by $\overline{G}_1$, $G_1 = G_2 = 1$. In this study, the shear moduli and Poisson's ratio of Regions S_1 and S_2 are kept the same. The material difference, as well as the difference in compliance, is accounted for by the differing constitutive relations.

3.3.2 Natural Frequencies

The natural frequencies of the vitreous are determined by Equation (3.20). They change with detachment size, and therefore during the process of detachment, as they are dependent on the geometry of the two regions. Figure 3.1 shows how these frequencies vary as a function of detachment. The lowest 18 frequencies are presented (nine associated with symmetric modes and nine associated with anti-symmetric modes). Figure 3.2 shows the same frequencies, but with only the symmetric frequencies displayed in Figure 3.2a and only the anti-symmetric ones displayed in Figure 3.2b.

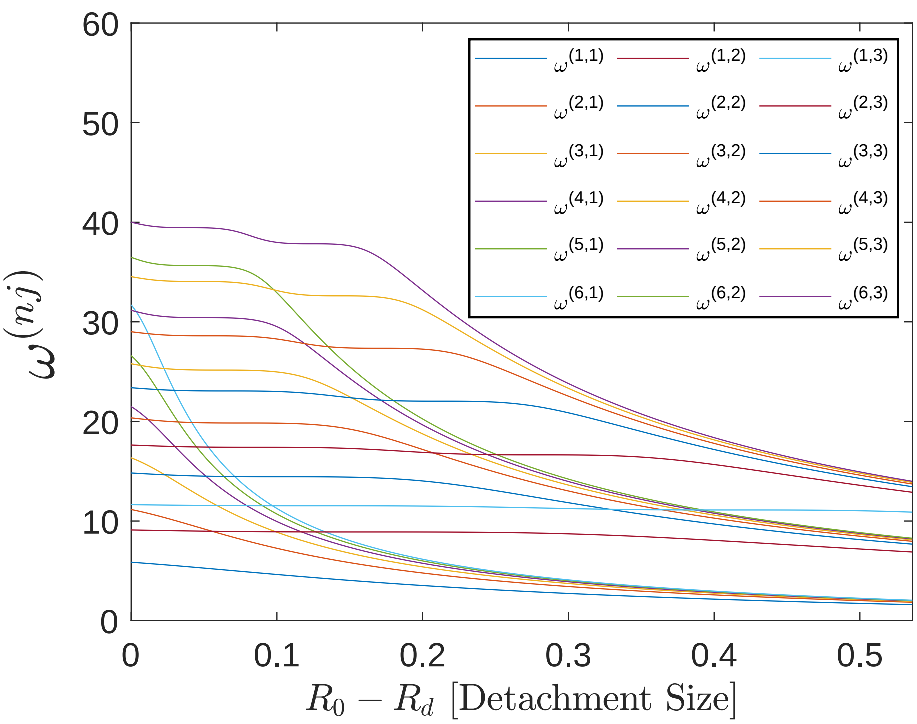

Figure 3.1: Natural frequencies as a function of detachment size.

As detachment increases, Region S_2 grows while Region S_1 shrinks. The detached region (Region S_2) is, of course, more compliant than the fully attached portion of the vitreous (Region S_1). Thus, the overall composite structure becomes more compliant as detachment progresses. Figure 3.1 shows that the natural frequencies decrease with increasing detachment, as may be anticipated for more compliant structures. Higher-order frequencies are seen to plateau for smaller detachment sizes. In addition, there exists small oscillations for the higher order frequencies at small detachment sizes. This is most likely a consequence of the atypical geometry of the vitreous cavity.

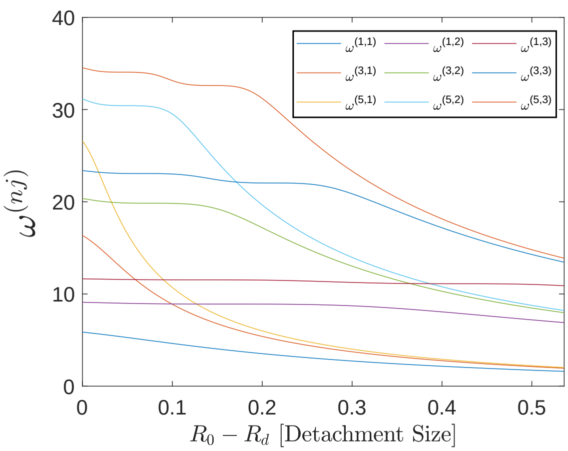

(a) Lowest nine symmetric mode natural frequencies as a function of detachment size.

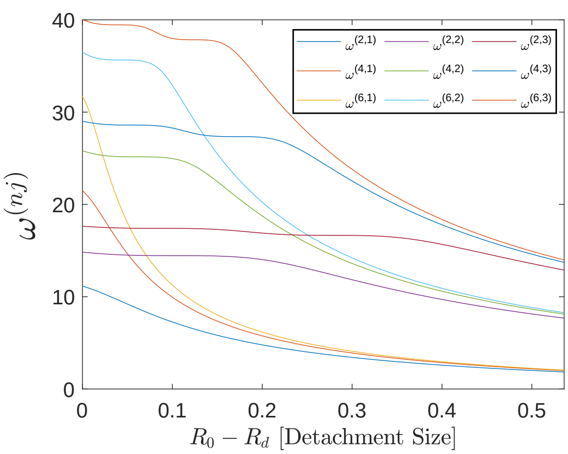

(b) Lowest nine anti-symmetric mode natural frequencies as a function of detachment size.

Figure 3.2: Symmetric and anti-symmetric natural frequencies.

3.3.3 Mode Shapes

The mutually orthogonal free vibration modes given by Equations (3.16a) and (3.16b) vary as a function of detachment size, like the natural frequencies. Figures 3.3 and 3.4 show these mode shapes for the case of partial detachment where $R_0 - R_d = 0.236$. The green shade represents the neutral position. The lighter yellow shading represents displacement in the positive ϕ direction, whereas the darker blue shade represents displacement in the negative ϕ direction. Boundary C_4 is represented by the black curve across the figures. It is apparent that, for most modes, the majority of the motion is concentrated in Region S_2.

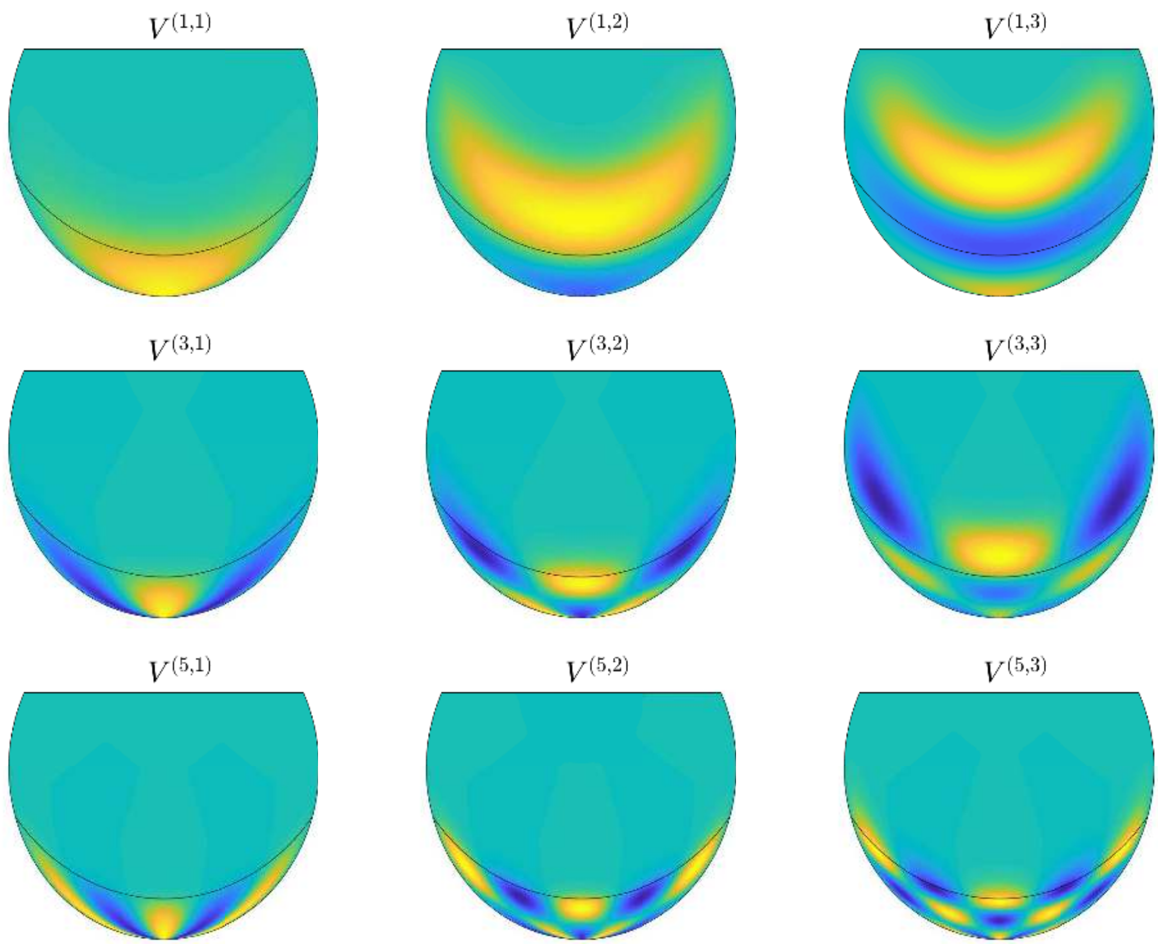

Figure 3.3: Lowest nine symmetric mode shapes.

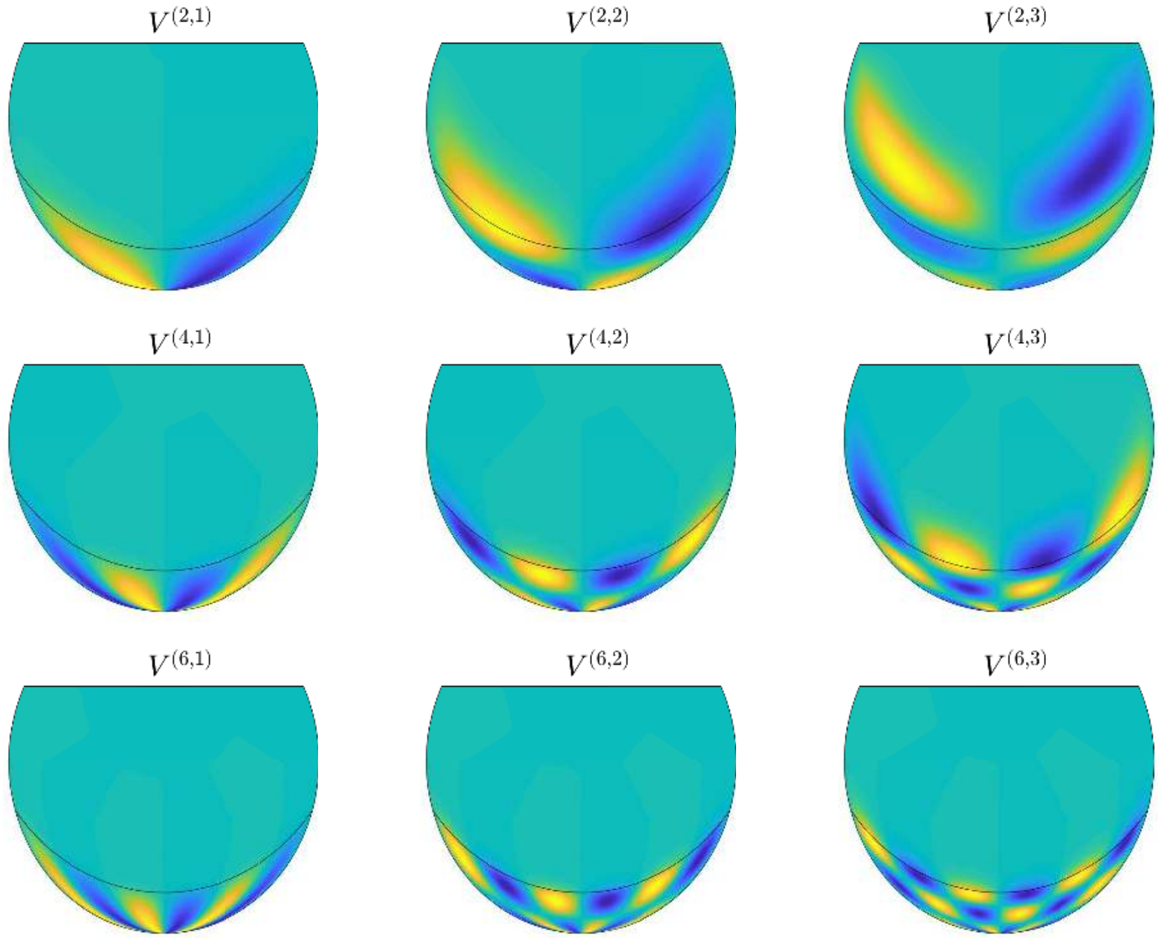

Figure 3.4: Lowest nine anti-symmetric mode shapes.

3.3.4 Relative Contribution of Modes

For the material properties selected, all vibration modes are overdamped. Thus, the contribution of each mode, as a function of time, during a saccade is given by Equation (3.25), where the integral has been evaluated analytically. It is worth noting that Equation (3.24d) vanishes for all anti-symmetric modes ($n = 2, 4, 6, ...$). This means that during saccadic motion, the anti-symmetric modes are not excited. Therefore the resultant motion of the vitreous will be entirely symmetric. The modal amplitudes are calculated from Equation (3.25), and are displayed graphically in Figures 3.5 – 3.7 for various detachment sizes and saccade amplitudes. For all saccades and detachment sizes, the motion is seen to be dominated by Mode $(1, 1)$, the lowest symmetric natural frequency. As the detachment size increases, the modal contribution, and thus the total motion of the vitreous increases, as the structure is less constrained. The relative contribution of Mode $(1,1)$ compared to the next highest contributing mode, Mode $(2,1)$, remains relatively consistent throughout the different cases. The overall contribution of each mode increases with saccade amplitude, corresponding to larger motion.

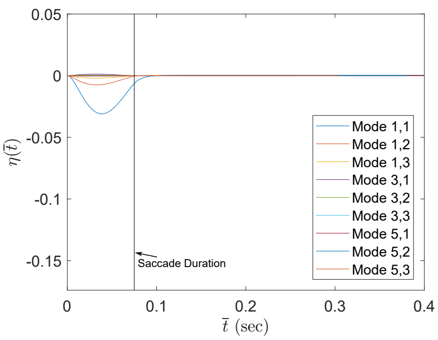

(a) Detachment size: $R_0 - R_d = 0.036$;
Saccade amplitude: 20°

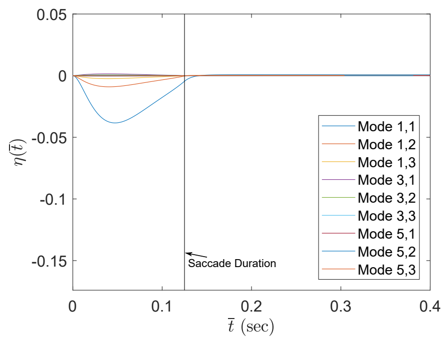

(b) Detachment size: $R_0 - R_d = 0.036$;
Saccade amplitude: 40°

Figure 3.5: Modal contribution as a function of dimensional time for small detachment.

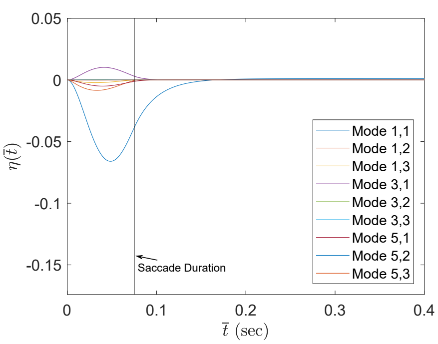

(a) Detachment size: $R_0 - R_d = 0.236$;
Saccade amplitude: 20°

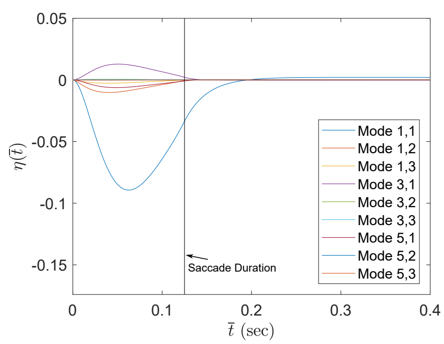

(b) Detachment size: $R_0 - R_d = 0.236$;
Saccade amplitude: 40°

Figure 3.6: Modal contribution as a function of dimensional time for medium detachment.

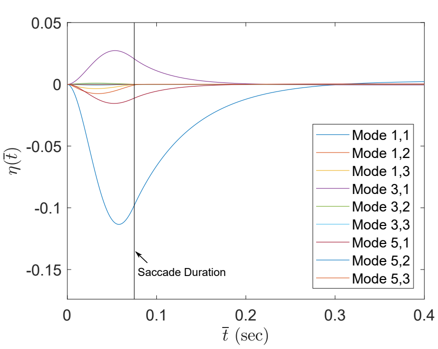

(a) Detachment size: $R_0 - R_d = 0.436$;
Saccade amplitude: 20°

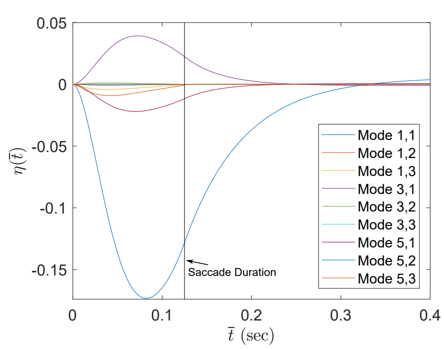

(b) Detachment size: $R_0 - R_d = 0.436$;
Saccade amplitude: 40°

Figure 3.7: Modal contribution as a function of dimensional time for large detachment.

3.3.5 Vitreous Response Fields

The displacement response, $v(r, \phi, t)$, of the partially detached vitreous body subject to saccadic motion is given by Equations (3.22a) and (3.22b). In this section, the response of an eye with vitreous detachment size $R_0 - R_d = 0.236$ subject to a 20° saccade is presented. This detachment size and saccade amplitude used here are chosen to be small enough so that they will not cause detachment progression. The criteria that determines detachment progression will be evaluated in the next section. The values chosen here demonstrate typical vitreous response.

Figure 3.8 shows the displacement field at two instances in time. Figure 3.8a shows the maximum displacement, which occurs at an instant just before the saccade is at its peak acceleration. For the 20^o saccade shown, this corresponds to $\bar{t} = 0.051$ sec. Consequently this time corresponds to the time of maximum normal and shear stress. Figure 3.8a looks very similar to Mode $(1, 1)$ because this is the dominant mode at this instance. Maximum displacement is seen to occur near the center of the vitreous body near the boundary between Region S_1 and S_2. Figure 3.8b shows the displacement at the instant the saccade has finished, which for the 20° saccade corresponds to $\bar{t}_s = 0.075$ sec. The displacement at this time is not zero, as Figure 3.6a showed that there is still responsive motion at this instant, which is consistent with the experimental results observed by Zimmerman (1980) [51] and Repetto et al. (2005) [41]. The response decays to near zero by $\bar{t} = 0.150$ sec.

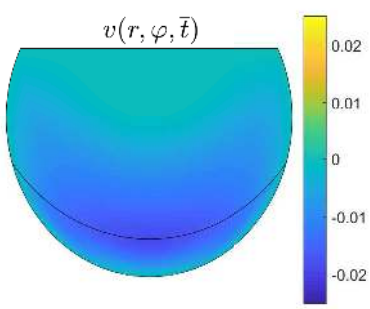

(a) Maximum displacement during the saccade; $\bar{t} = 0.051$ sec.

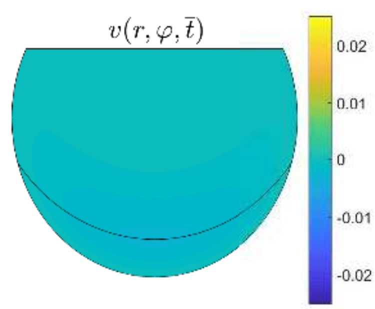

(b) Displacement at the instance the saccade has finished; $\bar{t}_s = 0.075$ sec.

Figure 3.8: Displacement of vitreous during a 20° saccade with detachment size, $R_0 - R_d = 0.236$.

Figures 3.9, 3.10, and 3.11 show the total stress during the saccade, but exclude the uniform stress due to IOP. The IOP is neglected in these plots because this pressure is equally balanced on the other side of the retinal wall, and does not effect the detachment behavior, which is studied next. Figures 3.9a and 3.10a show that normal stress is concentrated on the boundaries C_2 and C_3, where the vitreous is attached to the retina. The stress tends to be concentrated more towards the vitreous base, though there is still significant traction at detachment points a and b. Figure 3.11a shows the shear stress to be concentrated towards the interior of the vitreous body, specifically along C_4, the boundary between the two regions. Figures 3.9b, 3.10b, and 3.11b demonstrate that, although the external eye has stopped moving, there is still significant stress distributed throughout the vitreous, as a consequence of the lagging motion.

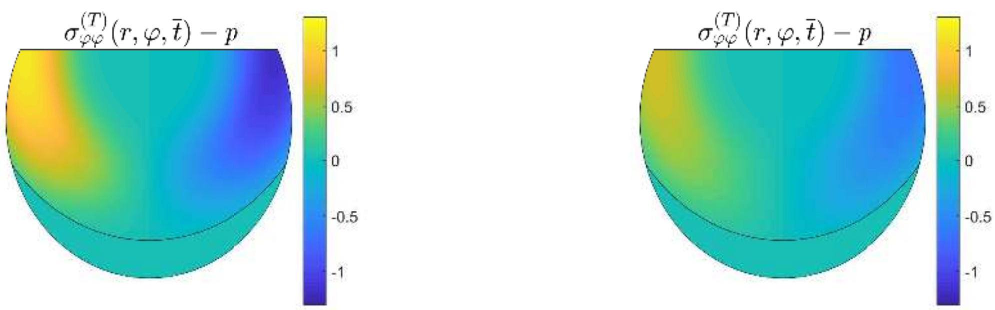

(a) Maximum normal stress, $\sigma_{\phi\phi}$, during the saccade; $\bar{t} = 0.051$ sec.

(b) Normal stress, $\sigma_{\phi\phi}$, at the instance the saccade has finished; $\bar{t}_s = 0.075$ sec.

Figure 3.9: Normal stress, $\sigma_{\phi\phi}$, of the vitreous during a 20° saccade with detachment size, $R_0 - R_d = 0.236$.

(a) Maximum normal stress, σ_{rr}, during the saccade; $\bar{t} = 0.051$ sec.

(b) Normal stress, σ_{rr}, at the instance the saccade has finished; $\bar{t}_s = 0.075$ sec.

Figure 3.10: Normal stress, σ_{rr}, of the vitreous during a 20° saccade with detachment size, $R_0 - R_d = 0.236$.

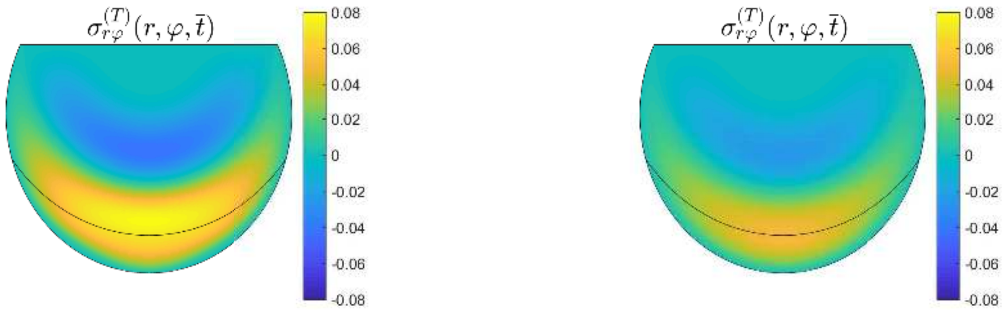

(a) Maximum shear stress, $\sigma_{r\phi}$, during the saccade; $\bar{t} = 0.051$ sec.

(b) Shear stress, $\sigma_{r\phi}$, at the instance the saccade has finished; $\bar{t}_s = 0.075$ sec.

Figure 3.11: Shear stress, $\sigma_{r\phi}$, of vitreous during a 20° saccade with detachment size, $R_0 - R_d = 0.236$.

It must be kept in mind that, for this model, the radial displacement is neglected, and so the vitreous is effectively "constrained." Figure 3.12 shows the inherent constraining force field that would have to be applied to the system to render the radial displacement to vanish. This is a visualization of λ_1 and λ_2 as determined by Equations (3.9a) and (3.9b). It is noteworthy that the constraint force is at its maximum value at the detachment points a and b. Thus, more so than at any other location, the displacement and stress fields cannot be fully trusted here.

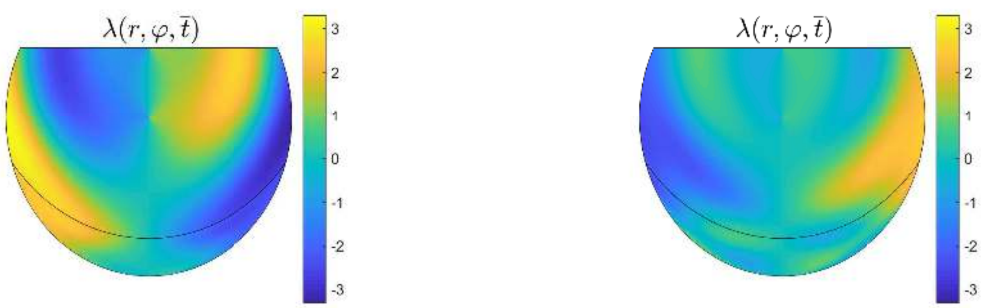

(a) Maximum inherent constraint force per unit volume, λ, during the saccade; $\bar{t} = 0.051$ sec.

(b) Inherent constraint force per unit volume, λ, at the instance the saccade has finished; $\bar{t}_s = 0.075$ sec.

Figure 3.12: Inherent force per unit volume, λ, necessary to constrain the radial motion of the vitreous to vanish during a 20° saccade with detachment size, $R_0 - R_d = 0.236$.

Figures 3.13 – 3.16 show the maximum resultant stress fields in the vitreous body for the same detachment size, $R_0 - R_d = 0.236$, but with increasing amplitude of the saccade. Stresses $\sigma_{\phi\phi}^{(T)}$, $\sigma_{rr}^{(T)}$, and $\sigma_{r\phi}^{(T)}$ all increase as the saccade amplitude increases. This agrees with the numerical results of Repetto et al. (2011) [42], Meskauskas et al. (2012) [37], and Modarreszadeh and Abouali (2014) [38], as well as the experimental results of Repetto et al. (2005) [41].

It is seen with this current model that the order of magnitude of maximum stress near the detachment points remains the same. In this context, the robustness of the model is demonstrated. This is similar to what was determined by the two-dimensional computational model of Repetto et al. (2011)), which considered the vitreous as a hybrid Neo-Hookean incompressible solid with Newtonian fluid-like dissipation.

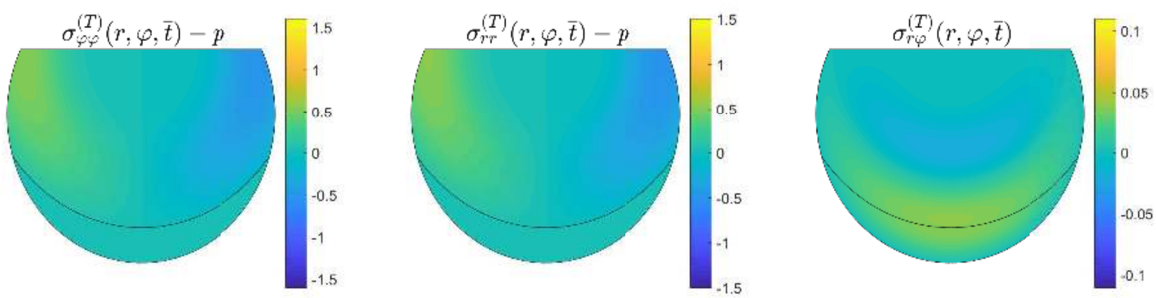

Figure 3.13: Maximum stress fields during a saccade of amplitude 10° with detachment size, $R_0 - R_d = 0.236$.

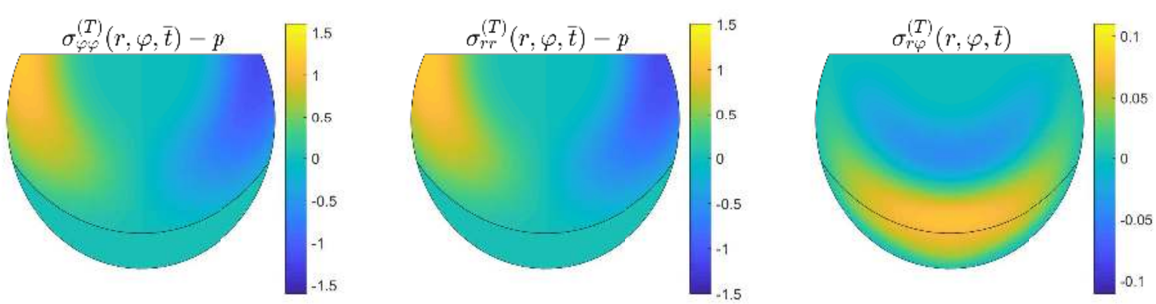

Figure 3.14: Maximum stress fields during a saccade of amplitude 20° with detachment size, $R_0 - R_d = 0.236$.

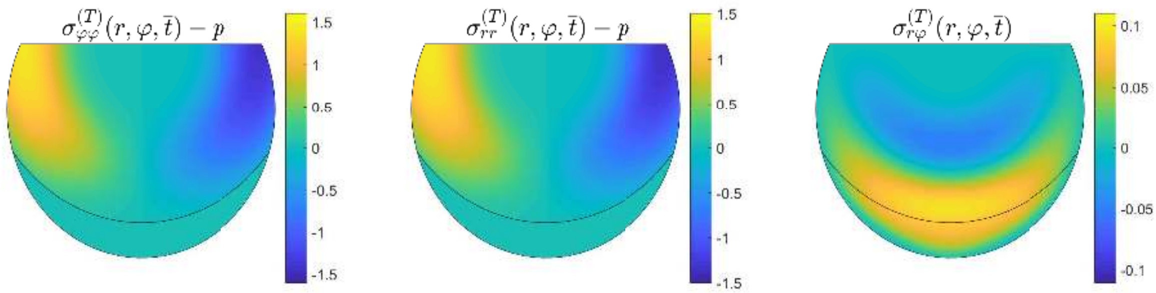

Figure 3.15: Maximum stress fields during a saccade of amplitude 30° with detachment size, $R_0 - R_d = 0.236$.

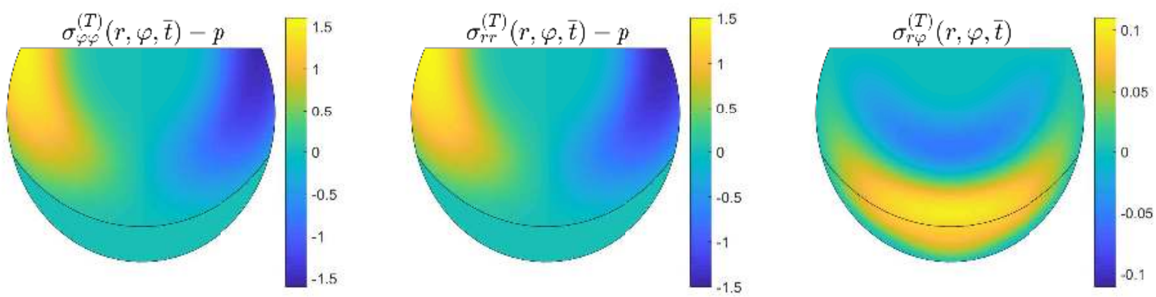

Figure 3.16: Maximum stress fields during a saccade of amplitude 40° with detachment size, $R_0 - R_d = 0.236$.

3.3.6 Detachment Progression

The energy formulation gave way to a transversality condition, which predicts the vitreous detachment behavior by locating boundaries a and b that correspond to configurations of the evolving ocular system that satisfy the dynamic conditions. Upon substitution of boundary conditions, along with the current selection of material properties, the transversality condition given by Equations (3.10) and (3.11) reduces to

$$\begin{aligned}\mathcal{G}\{R_d;a,b\} = &\left.\left[\frac{G_1(1-\nu_1)}{(1-2\nu_1)}\frac{1}{r}\left(\frac{\partial v_1}{\partial\phi}+\mu_1\frac{\partial^2 v_1}{\partial t\partial\phi}\right)\frac{1}{r}\frac{\partial v_1}{\partial\phi}-\sigma_{nt}^{(T;1)}\frac{\partial u_1^{(t)}}{\partial s}+\sigma_{nt}^{(T;2)}\frac{\partial u_2^{(t)}}{\partial s}\right]\right|_a \\ &+\left.\left[\frac{G_1(1-\nu_1)}{(1-2\nu_1)}\frac{1}{r}\left(\frac{\partial v_1}{\partial\phi}+\mu_1\frac{\partial^2 v_1}{\partial t\partial\phi}\right)\frac{1}{r}\frac{\partial v_1}{\partial\phi}-\sigma_{nt}^{(T;1)}\frac{\partial u_1^{(t)}}{\partial s}+\sigma_{nt}^{(T;2)}\frac{\partial u_2^{(t)}}{\partial s}\right]\right|_b = 2\gamma|_a + 2\gamma|_b\,.\end{aligned} \tag{3.30}$$

The energy release rate per unit depth is depicted graphically as a function of time in Figure 3.17 for saccades of various amplitudes, for three separate detachment sizes. The energy release rate quantifies the amount of energy released by the system if detachment occurs at a and b. These figures show that the energy release rate per unit depth increases with saccade amplitude. They also show that the energy release rate per unit depth increases with detachment size. The peak value of the energy release rate per unit depth occurs at the same instance of time as maximum displacement and maximum stress. The peak time increases with detachment size. If at any point during the saccade the energy release rate per unit depth is greater than $2\gamma|_a + 2\gamma|_b$, detachment will propagate.

It is instructive to see how the energy release rate per unit depth changes with detachment size because if the energy release rate per unit depth exceeds $2\gamma|_a + 2\gamma|_b$ for a given configuration, then detachment propagation occurs. It is assumed that the bond breaks instantaneously. The configuration now changes, and the energy release rate per unit depth needs to be evaluated at the next point, an infinitesimal distance away, to see if it exceeds $2\gamma|_a + 2\gamma|_b$, where a and b have moved to correspond to the new detachment size. If so, then the bond between the vitreous and the sensory retina breaks at this point, and the process is repeated at the next point and so on. Figure 3.18 shows the maximum energy release rate per unit depth as a function of detachment size for saccades of various amplitudes. For small detachment size, the curves all increase monotonically. However, when the detachment size exceeds $R_0 - R_d = 0.240$, it can be seen that the maximum energy release rate per unit depth for the 10° saccade begins to level off. For larger detachment sizes, it can be seen that the curves for larger saccades also begin to level off, and the maximum energy release rate per unit depth for some higher amplitude saccades even begin to decrease slightly.

The data displayed in Figure 3.18 is used to create Figure 3.19, a threshold path for the evolution of the propagating boundaries. This is a plot of the critical saccade amplitude per unit bond energy, $\widetilde{A}_{cr}$, as a function of detachment size, where

$$\widetilde{A}_{cr} = \frac{A_{cr}}{2\gamma|_a + 2\gamma|_b}, \tag{3.31}$$

and A_{cr} is the critical saccade amplitude—the amplitude required to precipitate detachment. It is the saccade amplitude that causes $\mathcal{G}\{R_d; a, b\} \geq 2\gamma|_a + 2\gamma|_b$. Currently, there is no

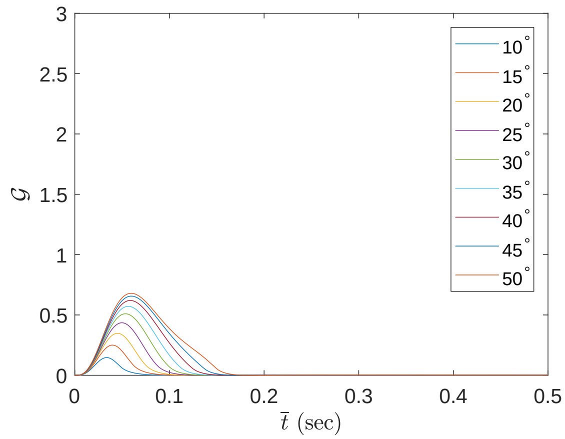

(a) Detachment size, $R_0 - R_d = 0.036$.

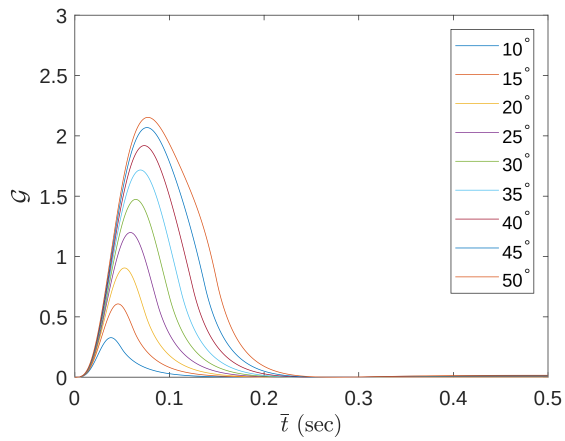

(b) Detachment size, $R_0 - R_d = 0.236$.

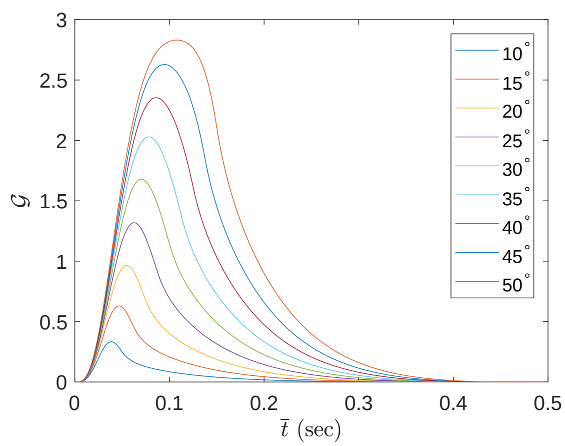

(c) Detachment size, $R_0 - R_d = 0.436$.

Figure 3.17: Energy release rate per unit depth as a function of time for small, medium, and large detachment sizes.

available data in the literature that quantifies the strength of the bond between the vitreous cortex and the sensory retina. To this end, the curve of Figure 3.19 is less quantitatively important, but reveals very interesting qualitative information about the characteristics of detachment propagation. The curve decreases monotonically until the detachment size is greater than $R_0 - R_d = 0.397$, after which point it increases slightly. The shape of the threshold path for initial detachment in the range $R_0 - R_d < 0.397$ implies that if a saccade is large enough to cause detachment to occur at one point, the detachment will grow continuously (catastrophically), assuming the bond strength is the same at all points.

For example, for initial detachment size of $R_0 - R_d = 0.136$, $\widetilde{A}_{cr} = 28.08°$. If the saccade has an amplitude this large (or larger), detachment will occur. It is seen that at the next point, $\widetilde{A}_{cr}$ is smaller. Thus, the current saccade has already surpassed the limit for this new detachment size, and the detachment will grow unstable and catastrophically all the way to the vitreous base or another point of abnormally strong adhesion between the vitreous cortex and the sensory retina. However, the behavior is different after $R_0 - R_d > 0.397$. The curve begins to increase, which implies that a prior detachment of that size or larger will progress in a stable manner, and thus will not progress without bound. This analysis

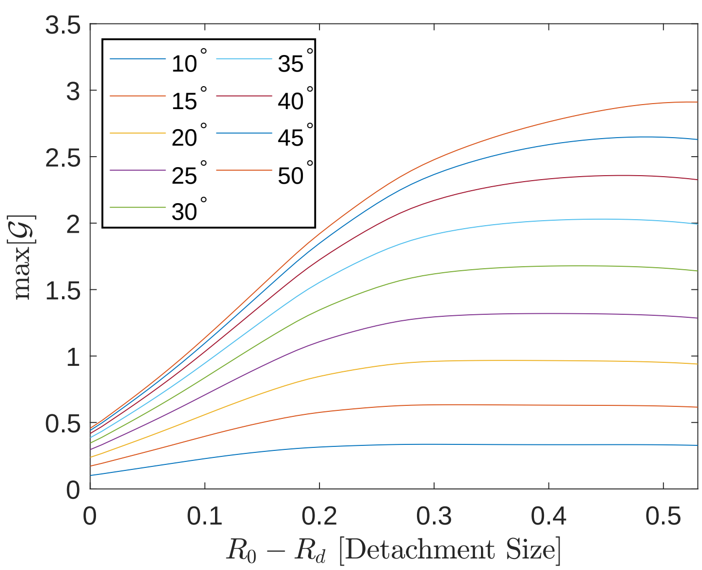

Figure 3.18: Maximum energy release rate per unit depth as a function of detachment size for saccades of nine different amplitudes.

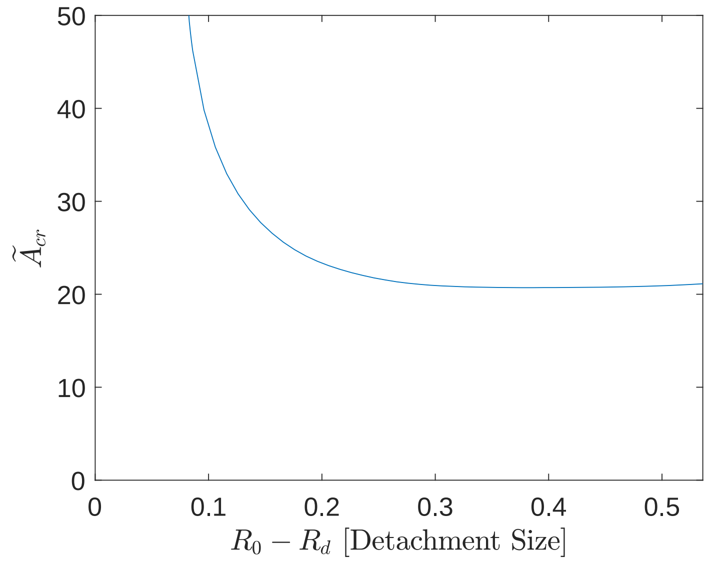

Figure 3.19: Critical saccade amplitude per unit bond energy as a function of detachment size.

assumes that the bond strength is the same at all points, which is known to not be true. It is, however, known that the bond is stronger near the vitreous base as well as at other places, due to random abnormalities such as lattice degeneration, cystic retinal tufts, and certain chorioretinal scars, including some photocoagulation scars. (Wilkerson and Rice) [49]. Therefore, it can be said that if the saccade is large enough to cause detachment of the vitreous from the sensory retina, the detachment will increase until either it reaches the vitreous base or it encounters a point with an abnormally strong bond strength.

3.3.7 Parameter Study

As mentioned earlier, the experimental data for the shear modulus of the vitreous varies significantly. In addition to not being able to measure the shear modulus in a healthy human eye directly, this property varies significantly from individual to individual. To this end, a parameter study on the influence of the shear modulus is presented.

Equation (3.20) shows that the natural frequencies of the system depend on two variable parameters: the current detachment size, and the shear modulus. The variation of natural frequency as a function of detachment size for a fixed shear modulus has already been presented in Figures 3.1, 3.2a, and 3.2b. The influence of shear modulus is demonstrated in Figures 3.20a, 3.20b, and 3.20c. These figures show the symmetric natural frequencies as a function of detachment size for various values of the shear modulus. Since it was already shown that only the symmetric modes are excited by saccadic motion, Figures 3.20a – 3.20c only show the symmetric frequencies. It can be seen that there is a direct relation between the shear modulus and the natural frequencies. A higher value of the shear modulus corresponds to a higher value in natural frequency. This makes physical sense, as a structure with a higher shear modulus is inherently stiffer, and therefore would oscillate at a higher frequency. The corresponding figures are seen to all maintain the same qualitative shape. The plateaus in the curves occur at the same points, and frequency branches cross at the same detachment sizes. This shows that the shape of the natural frequency variations are a function of geometry, and not a function of shear modulus.

Figures 3.21 – 3.23 show the maximum stress distributions during a typical 20° saccade, but with different values of shear modulus. As was seen with the natural frequencies, the qualitative behavior is not changed when varying the shear modulus. However, a larger value of shear modulus corresponds to greater stress. This result is consistent with the computational results of the study by Repetto et al. (2011) [42]. This increase in stress will invariably lead to larger values of energy release rate per unit depth, which means lower values of the critical saccade amplitude. Figures 3.24 and 3.25 confirm this. Figure 3.24 shows the maximum energy release rate per unit depth as a function of detachment size for different values of the shear modulus. It can be seen that the for higher values of the shear modulus, the curves increase monotonically for a larger amount of detachment. In addition, the maximum values are increased as the shear modulus increases. Figure 3.25 shows the normalized critical saccade amplitude as a function of detachment size for the different values of the shear modulus. It is seen that the qualitative behavior is catastrophic detachment for the majority of detachment sizes, until switching to weakly stable detachment. It is seen that an increase in the shear modulus leads to an increased detachment size corresponding to the change in qualitative detachment behavior. It is also shown that the critical saccade amplitude is lowered for larger values of the shear modulus.

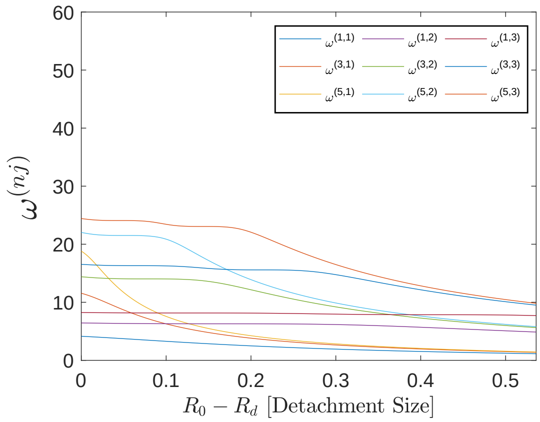

(a) Lowest nine symmetric natural frequencies as a function of detachment size for $G_1 = G_2 = 0.5$.

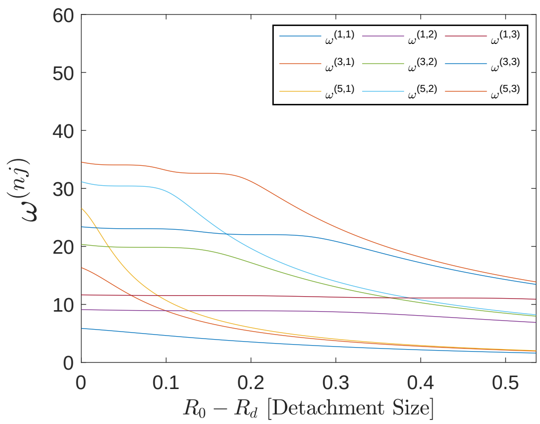

(b) Lowest nine symmetric natural frequencies as a function of detachment size for $G_1 = G_2 = 1.0$.

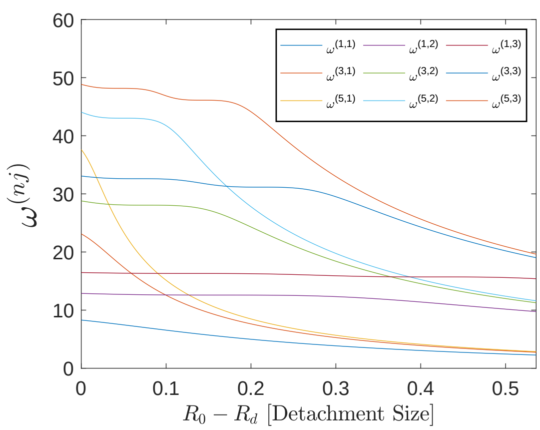

(c) Lowest nine symmetric natural frequencies as a function of detachment size for $G_1 = G_2 = 2.0$.

Figure 3.20: Lowest nine symmetric natural frequencies for different values of shear modulus.

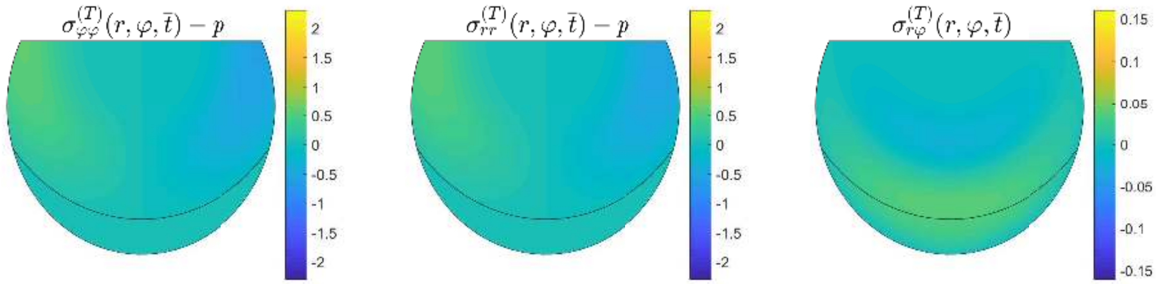

Figure 3.21: Maximum stress fields during a saccade of amplitude 20° with detachment size, $R_0 - R_d = 0.236$ where $G_1 = G_2 = 0.5$.

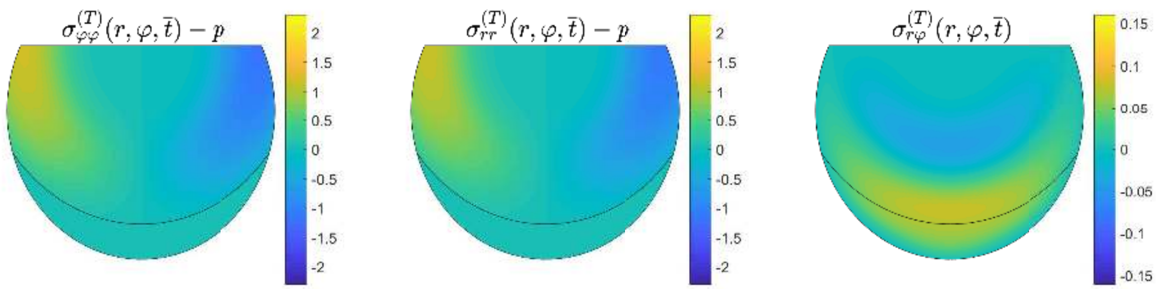

Figure 3.22: Maximum stress fields during a saccade of amplitude 20° with detachment size, $R_0 - R_d = 0.236$ where $G_1 = G_2 = 1.0$.

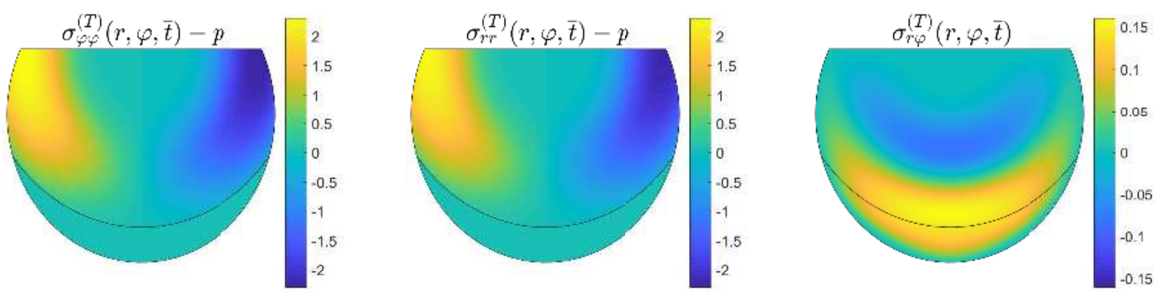

Figure 3.23: Maximum stress fields during a saccade of amplitude 20° with detachment size, $R_0 - R_d = 0.236$ where $G_1 = G_2 = 2.0$.

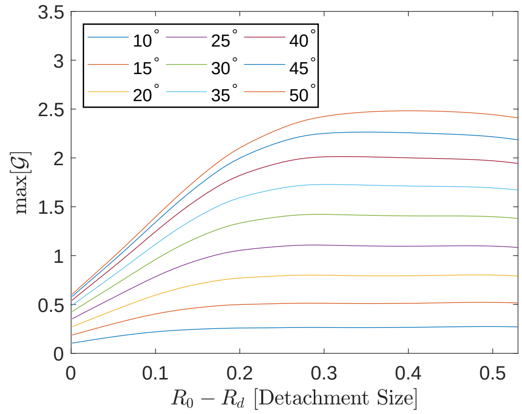

(a) Energy release rate per unit depth as a function of detachment size for various saccade amplitudes taking $G_1 = G_2 = 0.5$.

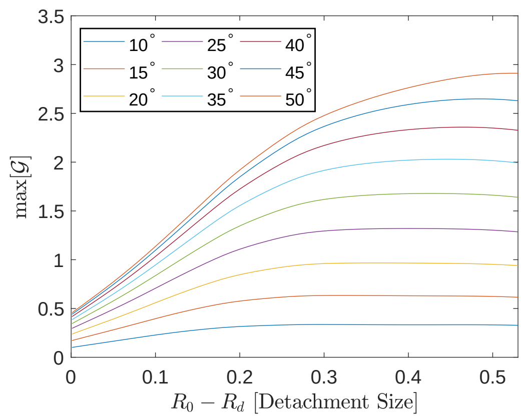

(b) Energy release rate per unit depth as a function of detachment size for various saccade amplitudes taking $G_1 = G_2 = 1.0$.

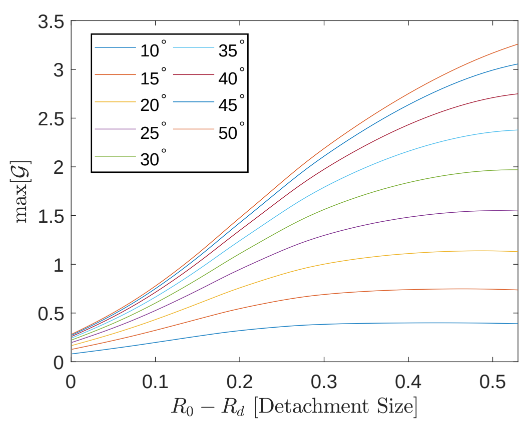

(c) Energy release rate per unit depth as a function of detachment size for various saccade amplitudes taking $G_1 = G_2 = 2.0$.

Figure 3.24: Energy release rate per unit depth as a function of detachment size for three different values of shear modulus.

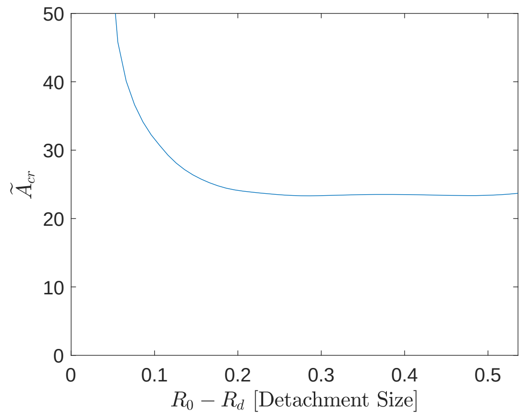

(a) Critical saccade amplitude per unit bond energy as a function of detachment size for $G_1 = G_2 = 0.5$.

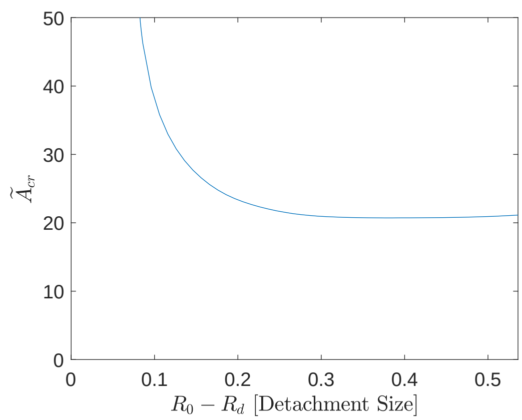

(b) Critical saccade amplitude per unit bond energy as a function of detachment size for $G_1 = G_2 = 1.0$.

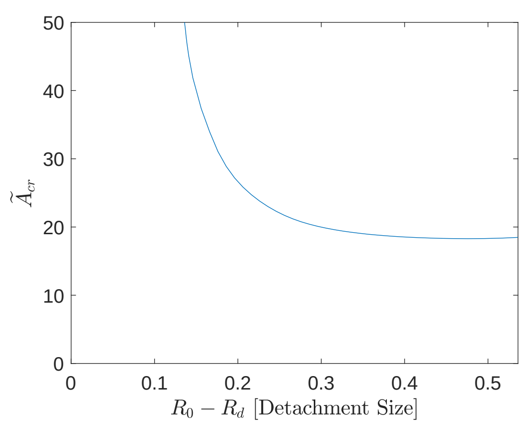

(c) Critical saccade amplitude per unit bond energy as a function of detachment size for $G_1 = G_2 = 2.0$.

Figure 3.25: Critical saccade amplitude per unit bond energy as a function of detachment size for different values of shear modulus.

3.4 Conclusions

A model of vitreous motion and detachment has been presented, and the response of the vitreous when subject to a typical saccade has been analyzed based on this model. The distribution of stress agrees qualitatively with what has been observed clinically and what has been predicted by other analytical, numerical, and computational studies, namely that the stress concentration is highest along the retinal walls. The detachment behavior of the vitreous from the sensory retina has been determined analytically. It is has been shown that the detachment will typically be catastrophic, meaning the detachment will continue to progress until there is an abnormality in the strength of the bond between the vitreous and the retina. This is consistent with what is observed, as partial posterior vitreous detachments typically progress rapidly to become complete vitreous separations (Wilkerson and Rice) [49].

The preceding analysis is based on the assumption that the radial motion can be neglected when compared to the circumferential motion. It was shown in Figure 3.12 that this is akin to applying an artificial constraint force per unit volume that is not negligible, and that this force, in fact, is largest at the detachment points. Therefore this assumption is dropped in the next chapter, and the problem is analyzed using a quasi-analytical method.

Chapter 4

Full 2D Solution

Chapter 3 presented an analytical solution to the model of vitreous detachment proposed in Chapter 2 by hypothesizing that the formation of long chains of collagen fibrils aligned in an anteroposterior orientation effectively constrains the vitreous from deforming in the radial direction. In this chapter, this constraint on the deformation of the vitreous is relaxed. The governing equations for the current model do not lend themselves to an exact analytical solution. A semi-analytical solution is developed and presented in which the deformation is approximated by a Rayleigh-Ritz solution based on the modes of the constrained 2D model.

4.1 Solution Procedure

Recall, the equations governing the motion of the vitreous body during a typical saccade derived in Chapter 2 are given by

$$\mathbf{m}_1 \frac{\partial^2 \mathbf{u}_1}{\partial t^2} + \mathbf{c}_1 \frac{\partial \mathbf{u}_1}{\partial t} + \mathbf{k}_1 \mathbf{u}_1 = \mathbf{F}_1, \tag{4.1a}$$

$$\mathbf{m}_2 \frac{\partial^2 \mathbf{u}_2}{\partial t^2} + \mathbf{c}_2 \frac{\partial \mathbf{u}_2}{\partial t} + \mathbf{k}_2 \mathbf{u}_2 = \mathbf{F}_2, \tag{4.1b}$$

where

$$\mathbf{u}_1 = \begin{bmatrix} u_1(r,\phi,t) \\ v_1(r,\phi,t) \end{bmatrix}, \tag{4.2a}$$

$$\mathbf{u}_2 = \begin{bmatrix} u_2(r,\phi,t) \\ u_2(r,\phi,t) \end{bmatrix}, \tag{4.2b}$$

$$\mathbf{m}_1 = \begin{bmatrix} \rho_1 & 0 \\ 0 & \rho_1 \end{bmatrix}, \tag{4.3a}$$

$$\mathbf{m}_2 = \begin{bmatrix} \rho_2 & 0 \\ 0 & \rho_2 \end{bmatrix}, \tag{4.3b}$$

$$\mathbf{k}_1 = \begin{bmatrix} \mathbf{k}_1^{(1,1)} & \mathbf{k}_1^{(1,2)} \\ \mathbf{k}_1^{(2,1)} & \mathbf{k}_1^{(2,2)} \end{bmatrix}, \tag{4.4a}$$

$$\mathbf{k}_2 = \begin{bmatrix} \mathbf{k}_2^{(1,1)} & \mathbf{k}_2^{(1,2)} \\ \mathbf{k}_2^{(2,1)} & \mathbf{k}_2^{(2,2)} \end{bmatrix}, \tag{4.4b}$$

$$\mathbf{c}_1 = \begin{bmatrix} \mathbf{c}_1^{(1,1)} & \mathbf{c}_1^{(1,2)} \\ \mathbf{c}_1^{(2,1)} & \mathbf{c}_1^{(2,2)} \end{bmatrix}, \tag{4.5a}$$

$$\mathbf{c}_2 = \begin{bmatrix} \mathbf{c}_2^{(1,1)} & \mathbf{c}_2^{(1,2)} \\ \mathbf{c}_2^{(2,1)} & \mathbf{c}_2^{(2,2)} \end{bmatrix}, \tag{4.5b}$$

$$\mathbf{F}_1 = \begin{bmatrix} -\frac{\rho_1 d_0 \sin\phi}{\sqrt{r^2+d_0^2-2rd_0\cos\phi}} \frac{\partial^2 u_o}{\partial t^2} \\ -\frac{\rho_1 (r-d_0\cos\phi)}{\sqrt{r^2+d_0^2-2rd_0\cos\phi}} \frac{\partial^2 u_o}{\partial t^2}, \end{bmatrix}, \tag{4.6a}$$

$$\mathbf{F}_2 = \begin{bmatrix} -\frac{\rho_2 d_0 \sin\phi}{\sqrt{r^2+d_0^2-2rd_0\cos\phi}} \frac{\partial^2 u_o}{\partial t^2} \\ -\frac{\rho_2 (r-d_0\cos\phi)}{\sqrt{r^2+d_0^2-2rd_0\cos\phi}} \frac{\partial^2 u_o}{\partial t^2}, \end{bmatrix}, \tag{4.6b}$$

and

$$\mathbf{k}_1^{(1,1)} = -\frac{2G_1(1-\nu_1)}{1-2\nu_1}\left[\frac{\partial^2}{\partial r^2} + \frac{1}{r}\frac{\partial}{\partial r} - \frac{1}{r^2}\right] - \frac{G_1}{r^2}\frac{\partial^2}{\partial \phi^2}, \tag{4.7a}$$

$$\mathbf{k}_1^{(1,2)} = \frac{2G_1}{1-2\nu_1}\frac{1}{r}\left[\frac{1-\nu_1}{r}\frac{\partial}{\partial \phi} - \nu_1\frac{\partial^2}{\partial r\partial \phi}\right] - \frac{G_1}{r}\left[\frac{\partial^2}{\partial r\partial \phi} - \frac{1}{r}\frac{\partial}{\partial \phi}\right], \tag{4.7b}$$

$$\mathbf{k}_1^{(2,1)} = -\frac{2G_1}{1-2\nu_1}\frac{1}{r}\left[\frac{1-\nu_1}{r}\frac{\partial}{\partial \phi} + \nu_1\frac{\partial^2}{\partial r\partial \phi}\right] - \frac{G_1}{r}\left[\frac{1}{r}\frac{\partial}{\partial \phi} + \frac{\partial^2}{\partial r\partial \phi}\right], \tag{4.7c}$$

$$\mathbf{k}_1^{(2,2)} = -\frac{2G_1(1-\nu_1)}{1-2\nu_1}\frac{1}{r^2}\frac{\partial^2}{\partial \phi^2} - G_1\left[\frac{\partial^2}{\partial r^2} + \frac{1}{r}\frac{\partial}{\partial r} - \frac{1}{r^2}\right], \tag{4.7d}$$

$$\mathbf{k}_2^{(1,1)} = -\frac{G_2}{r^2}\frac{\partial^2}{\partial\phi^2}, \tag{4.8a}$$

$$\mathbf{k}_2^{(1,2)} = -\frac{G_2}{r}\left[\frac{\partial^2}{\partial r\partial\phi} - \frac{1}{r}\frac{\partial}{\partial\phi}\right], \tag{4.8b}$$

$$\mathbf{k}_2^{(2,1)} = -\frac{G_2}{r}\left[\frac{1}{r}\frac{\partial}{\partial\phi} + \frac{\partial^2}{\partial r\partial\phi}\right], \tag{4.8c}$$

$$\mathbf{k}_2^{(2,2)} = -G_2\left[\frac{\partial^2}{\partial r^2} + \frac{1}{r}\frac{\partial}{\partial r} - \frac{1}{r^2}\right], \tag{4.8d}$$

$$\mathbf{c}_1^{(1,1)} = \mu_1\mathbf{k}_1^{(1,1)}, \tag{4.9a}$$

$$\mathbf{c}_1^{(1,2)} = \mu_1\mathbf{k}_1^{(1,2)}, \tag{4.9b}$$

$$\mathbf{c}_1^{(2,1)} = \mu_1\mathbf{k}_1^{(2,1)}, \tag{4.9c}$$

$$\mathbf{c}_1^{(2,2)} = \mu_1\mathbf{k}_1^{(2,2)}, \tag{4.9d}$$

$$\mathbf{c}_2^{(1,1)} = \mu_2\mathbf{k}_2^{(1,1)}, \tag{4.10a}$$

$$\mathbf{c}_2^{(1,2)} = \mu_2\mathbf{k}_2^{(1,2)}, \tag{4.10b}$$

$$\mathbf{c}_2^{(2,1)} = \mu_2\mathbf{k}_2^{(2,1)}, \tag{4.10c}$$

$$\mathbf{c}_2^{(2,2)} = \mu_2\mathbf{k}_2^{(2,2)}. \tag{4.10d}$$

The boundary conditions and matching conditions for both regions take the following forms

$$u_1 = 0 \qquad \text{on } C_1 \text{ in } S_1, \tag{4.11a}$$

$$v_1 = 0 \qquad \text{on } C_1 \text{ in } S_1, \tag{4.11b}$$

$$u_1 = 0 \qquad \text{on } C_2 \text{ in } S_1, \tag{4.12a}$$

$$v_1 = 0 \qquad \text{on } C_2 \text{ in } S_1, \tag{4.12b}$$

$$u_1 = 0 \qquad \text{on } C_3 \text{ in } S_1, \tag{4.13a}$$

$$v_1 = 0 \qquad \text{on } C_3 \text{ in } S_1, \tag{4.13b}$$

$$u_1 = u_2 \qquad \text{on } C_4, \tag{4.13c}$$

$$v_1 = v_2 \qquad \text{on } C_4, \tag{4.13d}$$

$$\sigma_{r\phi}^{(T;1)} = \sigma_{r\phi}^{(T;2)} \qquad \text{on } C_4, \tag{4.13e}$$

$$u_1 = 0 \qquad \text{on } C_4, \tag{4.13f}$$

$$\sigma_{r\phi}^{(T;2)} = 0 \qquad \text{on } C_2 \text{ in } S_2, \tag{4.13g}$$

$$\sigma_{r\phi}^{(T;2)} = 0 \qquad \text{on } C_3 \text{ in } S_2. \tag{4.13h}$$

The evolution of the detachment of the vitreous cortex from the sensory retina is determined by the transversality condition which locates boundary C_4, and consequently boundary points a and b. The transversality condition is given by

$$\mathcal{G}\{R_d; a, b\} = 2\gamma|_a + 2\gamma|_b\,, \tag{4.14}$$

where $\mathcal{G}$ is interpreted as the energy release rate, and is given by

$$
\begin{aligned}
\mathcal{G}\{R_d; a, b\} = &\left\{ \frac{1}{2} \left[\sigma_{rr}^{(T;1)} \varepsilon_{rr}^{(1)} + \sigma_{\phi\phi}^{(T;1)} \varepsilon_{\phi\phi}^{(1)} + 2\left(\sigma_{r\phi}^{(T;1)} \varepsilon_{r\phi}^{(1)} - \sigma_{r\phi}^{(T;2)} \varepsilon_{r\phi}^{(2)} \right) \right] - \sigma_{nt}^{(T;1)} \frac{\partial u_1^{(t)}}{\partial s} \right. \\
&+ \sigma_{nt}^{(T;2)} \frac{\partial u_2^{(t)}}{\partial s} - \frac{\rho_1}{2} \left[\left(\frac{\partial u_1}{\partial t} + \frac{\partial u_o}{\partial t} \frac{d_0 \sin\phi}{\sqrt{r^2 + d_0^2 - 2rd_0 \cos\phi}} \right)^2 \right. \\
&\left. + \left(\frac{\partial v_1}{\partial t} + \frac{\partial u_o}{\partial t} \frac{r - d_0 \cos\phi}{\sqrt{r^2 + d_0^2 - 2rd_0 \cos\phi}} \right)^2 \right] \\
&+ \frac{\rho_2}{2} \left[\left(\frac{\partial u_2}{\partial t} + \frac{\partial u_o}{\partial t} \frac{d_0 \sin\phi}{\sqrt{r^2 + d_0^2 - 2rd_0 \cos\phi}} \right)^2 \right. \\
&\left. \left. + \left(\frac{\partial v_2}{\partial t} + \frac{\partial u_o}{\partial t} \frac{r - d_0 \cos\phi}{\sqrt{r^2 + d_0^2 - 2rd_0 \cos\phi}} \right)^2 \right] \right\} \Bigg|_a \\
+ &\left\{ \frac{1}{2} \left[\sigma_{rr}^{(T;1)} \varepsilon_{rr}^{(1)} + \sigma_{\phi\phi}^{(T;1)} \varepsilon_{\phi\phi}^{(1)} + 2\left(\sigma_{r\phi}^{(T;1)} \varepsilon_{r\phi}^{(1)} - \sigma_{r\phi}^{(T;2)} \varepsilon_{r\phi}^{(2)} \right) \right] - \sigma_{nt}^{(T;1)} \frac{\partial u_1^{(t)}}{\partial s} \right. \qquad (4.15) \\
&+ \sigma_{nt}^{(T;2)} \frac{\partial u_2^{(t)}}{\partial s} - \frac{\rho_1}{2} \left[\left(\frac{\partial u_1}{\partial t} + \frac{\partial u_o}{\partial t} \frac{d_0 \sin\phi}{\sqrt{r^2 + d_0^2 - 2rd_0 \cos\phi}} \right)^2 \right. \\
&\left. + \left(\frac{\partial v_1}{\partial t} + \frac{\partial u_o}{\partial t} \frac{r - d_0 \cos\phi}{\sqrt{r^2 + d_0^2 - 2rd_0 \cos\phi}} \right)^2 \right] \\
&+ \frac{\rho_2}{2} \left[\left(\frac{\partial u_2}{\partial t} + \frac{\partial u_o}{\partial t} \frac{d_0 \sin\phi}{\sqrt{r^2 + d_0^2 - 2rd_0 \cos\phi}} \right)^2 \right. \\
&\left. \left. + \left(\frac{\partial v_2}{\partial t} + \frac{\partial u_o}{\partial t} \frac{r - d_0 \cos\phi}{\sqrt{r^2 + d_0^2 - 2rd_0 \cos\phi}} \right)^2 \right] \right\} \Bigg|_b \\
&+ [\vec{e}_t \cdot -\vec{e}_r]|_{(a \text{ or } b)} \int\limits_{C_4} \sigma_{rr}^{(T;1)} \frac{\partial u_1}{\partial r} ds.
\end{aligned}
$$

As in the previous chapter, these equations represent a forced vibration problem for a composite domain with an internal boundary whose location is to be determined as part of the solution. This problem will again be solved via modal analysis where the forced vibration response is expressed as a linear combination of the undamped free vibration modes. These modes are determined semi-analytically by way of using the Rayleigh-Ritz method.

4.1.1 Undamped Free Vibration Response Using the Rayleigh-Ritz Method

Consider the undamped free vibration problem which determines the response modes of the vitreous. The governing equations of motion in Regions S_1 and S_2 are given by

$$\mathbf{m}_1 \frac{\partial^2 \mathbf{u}_1}{\partial t^2} + \mathbf{k}_1 \mathbf{u}_1 = \mathbf{0}, \tag{4.16a}$$

$$\mathbf{m}_2 \frac{\partial^2 \mathbf{u}_2}{\partial t^2} + \mathbf{k}_2 \mathbf{u}_2 = \mathbf{0}. \tag{4.16b}$$

It is assumed that the response in each region will be of the form

$$u_1(r, \phi, t) = \sum_{m=1}^{\infty} A_u^{(m)} U_1^{(m)} e^{i\omega^{(m)} t}, \tag{4.17a}$$

$$u_2(r, \phi, t) = \sum_{m=1}^{\infty} A_u^{(m)} U_2^{(m)} e^{i\omega^{(m)} t}, \tag{4.17b}$$

$$v_1(r, \phi, t) = \sum_{m=1}^{\infty} A_v^{(m)} V_1^{(m)} e^{i\omega^{(m)} t}, \tag{4.17c}$$

$$v_2(r, \phi, t) = \sum_{m=1}^{\infty} A_v^{(m)} V_2^{(m)} e^{i\omega^{(m)} t}, \tag{4.17d}$$

where $A_u^{(m)}$ and $A_v^{(m)}$ are arbitrary constants that satisfy the initial conditions, and $U_1^{(m)}$, $U_2^{(m)}$, $V_1^{(m)}$, and $V_2^{(m)}$ are the unknown modal functions associated with the (yet to be determined) natural frequencies $\omega^{(m)}$. Since the governing equations given by (4.16a) and (4.16b) do not yield exact solutions for the natural frequencies and corresponding mode shapes, the Rayleigh-Ritz method is used to approximate the unknown modal functions and the associated natural frequencies.

The Rayleigh-Ritz method is an approximation method used in mathematics for solving eigenvalue equations that may or may not have exact analytical solutions. This approach is used in structural dynamics for determining the response of a vibrating system. The development here follows that demonstrated by Ilanko et. al (2014) [29]. The theory is based upon minimizing the *Rayleigh quotient*, $\mathcal{R}$, of a vibrating system. The Rayleigh quotient, by definition, is the ratio of the maximum of the potential energy to the maximum of the kinetic energy functionals. If the system is vibrating harmonically and the vibration mode shape is known then the natural frequency at which it oscillates can be determined exactly by the Rayleigh quotient. If the form of multiple modes are known, then the corresponding natural frequency for each mode is determined by the Rayleigh quotient. For this specific problem, the Rayleigh quotient takes the form

$$\mathcal{R}[\mathbf{U}^{(m)}(r,\phi)] = \frac{\mathcal{U}^{(1)}[\mathbf{U}^{(m)}(r,\phi)] + \mathcal{U}^{(2)}[\mathbf{U}^{(m)}(r,\phi)]}{\mathcal{T}^{(1)}[\mathbf{U}^{(m)}(r,\phi)] + \mathcal{T}^{(2)}[\mathbf{U}^{(m)}(r,\phi)]} = {\omega^{(m)}}^2 \tag{4.18}$$

where

$$\mathbf{U}^{(m)}(r,\phi) = \mathbf{U}_1^{(m)}(r,\phi) + \mathbf{U}_2^{(m)}(r,\phi) = \begin{bmatrix} U_1^{(m)}(r,\phi) \\ V_1^{(m)}(r,\phi) \end{bmatrix} + \begin{bmatrix} U_2^{(m)}(r,\phi) \\ V_2^{(m)}(r,\phi) \end{bmatrix} \tag{4.19}$$

is a specific vibration mode.

If, however, the mode shapes and natural frequencies are unknown (as is the case here), minimizing the Rayleigh quotient will determine approximate values of the natural frequencies and mode shapes. This extension of Rayleigh's quotient is known as the Rayleigh-Ritz method. This involves expressing each vibration mode as a series of admissible functions, each multiplied by a (yet to be determined) constant coefficient as shown here.

$$\mathbf{U}^{(m)}(r,\phi) = \sum_{n=1}^{N}\sum_{j=1}^{J} \begin{bmatrix} C_u^{(m;nj)}\left(U_1^{(nj)}(r,\phi) + U_2^{(nj)}(r,\phi)\right) \\ C_v^{(m;nj)}\left(V_1^{(nj)}(r,\phi) + V_2^{(nj)}(r,\phi)\right) \end{bmatrix} \tag{4.20}$$

An admissible function is a continuous function, which is differentiable up to the order of the highest derivative in the kinetic or potential energy functionals, and also satisfies all of the kinematic boundary conditions of the system. In the context of the Rayleigh-Ritz method, these admissible functions $U_1^{(nj)}$, $U_2^{(nj)}$, $V_1^{(nj)}$, and $V_2^{(nj)}$ are referred to as *trial functions*. Once these trial functions are chosen, the Rayleigh quotient can then be minimized with respect to the unknown constants $C_p^{(m;nj)}$, where $p = u, v$. The Rayleigh quotient for each mode is minimized by taking the partial derivative of each trial function with respect to each unknown constant. If M modes are taken to solve the problem, and each mode is assumed to consist of $N \times J$ trial functions for u and $N \times J$ trial functions for v, then the minimization produces $M \times (2 \times N \times J)$ coupled equations of the form

$$\frac{\partial}{\partial C_p^{(k;nj)}}\left(\mathcal{R}\left[\mathbf{U}^{(m)}(r,\phi)\right]\right). \tag{4.21}$$

These equations are then solved simultaneously for the unknown constants and unknown natural frequencies, $\omega^{(m)}$. Since the problem is linear, each equation will be a linear function of the unknown constants. If Equation (4.21) is expressed in terms of the potential and kinetic energy functionals, it can be transformed into the following form

$$\mathbf{KC} - \omega^2 \mathbf{MC} = \mathbf{0} \tag{4.22}$$

where

$$\mathbf{K} = \begin{bmatrix} \frac{\partial^2 \mathcal{U}}{\partial C_u^{(1;1,1)} \partial C_u^{(1;1,1)}} & \cdots & \frac{\partial^2 \mathcal{U}}{\partial C_u^{(1;1,1)} \partial C_u^{(M;N,J)}} & \frac{\partial^2 \mathcal{U}}{\partial C_u^{(1;1,1)} \partial C_v^{(1;1,1)}} & \cdots & \frac{\partial^2 \mathcal{U}}{\partial C_u^{(1;1,1)} \partial C_v^{(M;N,J)}} \\ \vdots & \ddots & \vdots & \vdots & \ddots & \vdots \\ \frac{\partial^2 \mathcal{U}}{\partial C_u^{(M;N,J)} \partial C_u^{(1;1,1)}} & \cdots & \frac{\partial^2 \mathcal{U}}{\partial C_u^{(M;N,J)} \partial C_u^{(M;N,J)}} & \frac{\partial^2 \mathcal{U}}{\partial C_u^{(M;N,J)} \partial C_v^{(1;1,1)}} & \cdots & \frac{\partial^2 \mathcal{U}}{\partial C_u^{(M;N,J)} \partial C_v^{(M;N,J)}} \\ \frac{\partial^2 \mathcal{U}}{\partial C_v^{(1;1,1)} \partial C_u^{(1;1,1)}} & \cdots & \frac{\partial^2 \mathcal{U}}{\partial C_v^{(1;1,1)} \partial C_u^{(M;N,J)}} & \frac{\partial^2 \mathcal{U}}{\partial C_v^{(1;1,1)} \partial C_v^{(1;1,1)}} & \cdots & \frac{\partial^2 \mathcal{U}}{\partial C_v^{(1;1,1)} \partial C_v^{(M;N,J)}} \\ \vdots & \ddots & \vdots & \vdots & \ddots & \vdots \\ \frac{\partial^2 \mathcal{U}}{\partial C_v^{(1;1,1)} \partial C_u^{(1;1,1)}} & \cdots & \frac{\partial^2 \mathcal{U}}{\partial C_v^{(1;1,1)} \partial C_u^{(M;N,J)}} & \frac{\partial^2 \mathcal{U}}{\partial C_v^{(1;1,1)} \partial C_v^{(1;1,1)}} & \cdots & \frac{\partial^2 \mathcal{U}}{\partial C_v^{(1;1,1)} \partial C_v^{(M;N,J)}} \end{bmatrix}, \tag{4.23a}$$

$$\mathbf{M} = \begin{bmatrix} \frac{\partial^2 \mathcal{T}}{\partial C_u^{(1;1,1)} \partial C_u^{(1;1,1)}} & \cdots & \frac{\partial^2 \mathcal{T}}{\partial C_u^{(1;1,1)} \partial C_u^{(M;N,J)}} & \frac{\partial^2 \mathcal{T}}{\partial C_u^{(1;1,1)} \partial C_v^{(1;1,1)}} & \cdots & \frac{\partial^2 \mathcal{T}}{\partial C_u^{(1;1,1)} \partial C_v^{(M;N,J)}} \\ \vdots & \ddots & \vdots & \vdots & \ddots & \vdots \\ \frac{\partial^2 \mathcal{T}}{\partial C_u^{(M;N,J)} \partial C_u^{(1;1,1)}} & \cdots & \frac{\partial^2 \mathcal{T}}{\partial C_u^{(M;N,J)} \partial C_u^{(M;N,J)}} & \frac{\partial^2 \mathcal{T}}{\partial C_u^{(M;N,J)} \partial C_v^{(1;1,1)}} & \cdots & \frac{\partial^2 \mathcal{T}}{\partial C_u^{(M;N,J)} \partial C_v^{(M;N,J)}} \\ \frac{\partial^2 \mathcal{T}}{\partial C_v^{(1;1,1)} \partial C_u^{(1;1,1)}} & \cdots & \frac{\partial^2 \mathcal{T}}{\partial C_v^{(1;1,1)} \partial C_u^{(M;N,J)}} & \frac{\partial^2 \mathcal{T}}{\partial C_v^{(1;1,1)} \partial C_v^{(1;1,1)}} & \cdots & \frac{\partial^2 \mathcal{T}}{\partial C_v^{(1;1,1)} \partial C_v^{(M;N,J)}} \\ \vdots & \ddots & \vdots & \vdots & \ddots & \vdots \\ \frac{\partial^2 \mathcal{T}}{\partial C_v^{(1;1,1)} \partial C_u^{(1;1,1)}} & \cdots & \frac{\partial^2 \mathcal{T}}{\partial C_v^{(1;1,1)} \partial C_u^{(M;N,J)}} & \frac{\partial^2 \mathcal{T}}{\partial C_v^{(1;1,1)} \partial C_v^{(1;1,1)}} & \cdots & \frac{\partial^2 \mathcal{T}}{\partial C_v^{(1;1,1)} \partial C_v^{(M;N,J)}} \end{bmatrix}, \tag{4.23b}$$

$$\mathbf{C} = \left[C_u^{(1;1,1)}, \ldots, C_u^{(M;N,J)}, C_v^{(1;1,1)} \ldots C_v^{(M;N,J)} \right]^T, \tag{4.23c}$$

and $\mathcal{U} = \mathcal{U}^{(1)} + \mathcal{U}^{(2)}$ and $\mathcal{T} = \mathcal{T}^{(1)} + \mathcal{T}^{(2)}$.

Equation (4.22) corresponds to an eigenvalue problem where the eigenvalues represent the squares of the natural frequencies, and the eigenfunctions determine the unknown constants of the trial functions. Equation (4.22) yields M distinct natural frequencies (one for each mode), each associated with $2 \times N \times J$ constants (one for each trial function in each mode). More and more trial functions are added until both the natural frequencies and the unknown coefficients converge to steady values.

It is worth noting that the natural frequencies determined by the Rayleigh-Ritz method will always converge from above, and thus provide an over-estimate of the natural frequencies. (See, for example, Benaroya and Nagurka (2010) [6].) Also, when adding more trial functions, the lowest natural frequency will converge to the exact value first, followed by the second natural frequency, and so on. It is also worth noting that the mode shapes will not converge as quickly as their corresponding natural frequencies. Thus, checking for convergence of natural frequencies alone is not enough to accurately determine the response field of the structure.

Any functions which are orthogonal to each other will suffice because they form an orthogonal basis upon which to expand the mode. The most common choice of trial functions are polynomial or sinusoidal functions. However, to ensure quicker convergence and to minimize computations, it is advantageous to choose trial functions that are the modal functions of a similar structure. To this end, the modal functions for the radially constrained problem will serve as the trial functions for the displacement in the circumferential direction. Therefore,

$$V_1^{(nj)}(r,\phi) = J_{\xi^{(n)}}\left(\alpha_1^{(nj)} r\right) \begin{cases} \cos(n\phi^*) & (n \sim \text{odd}) \\ \sin(n\phi^*) & (n \sim \text{even}) \end{cases} , \tag{4.24}$$

$$V_2^{(nj)}(r,\phi) = T^{(nj)}\left[J_1\left(\alpha_2^{(nj)} r\right) - S^{(nj)} Y_1\left(\alpha_2^{(nj)} r\right)\right] \begin{cases} \cos(n\phi^*) \ \ (n \sim \text{odd}) \\ \sin(n\phi^*) \ \ (n \sim \text{even}) \end{cases} , \tag{4.25}$$

where $\xi^{(n)}$ is given by Equation (3.17), $\alpha_1^{(nj)}$ is given by Equation (3.18a), $\alpha_2^{(nj)}$ is given by Equation (3.18b), $S^{(nj)}$ is given by Equation (3.19a), and $T^{(nj)}$ is given by Equation (3.19b).

Since there is no prior solution to use as trial functions for the displacement in the r-direction, trigonometric trial functions are chosen so as to satisfy the kinematic boundary conditions. Therefore,

$$U_1^{(nj)}(r,\phi) = \sin\left(\frac{j\pi r}{R_d}\right)\begin{cases} \cos(n\phi^*) & (n \sim \text{odd}) \\ \sin(n\phi^*) & (n \sim \text{even}) \end{cases}, \tag{4.26}$$

$$U_2^{(nj)}(r,\phi) = \sin\left(\frac{j\pi(r-R_0)}{R_0-R_d}\right)\begin{cases} \cos(n\phi^*) \;\; (n \sim \text{odd}) \\ \sin(n\phi^*) \;\; (n \sim \text{even}) \end{cases}. \tag{4.27}$$

Convergence tests reveal that for the circumferential trial functions, $V_1^{(nj)}$ and $V_2^{(nj)}$, taking $n = 6$ and $j = 3$ and for the radial trial functions, $U_1^{(nj)}$ and $U_2^{(nj)}$, taking $n = 6$ and $j = 4$ are sufficient for the solutions to converge when using the lowest 18 modes.

4.1.2 Modal Analysis

The Rayleigh-Ritz procedure gave way to the undamped free vibration modes and corresponding natural frequencies. In order to apply modal analysis, the modes as given by Equations (4.24), (4.25), (4.26), and (4.27) must be mutually orthogonal to one another so that they provide an orthogonal basis on which the solution to the full problem can be expressed. Since the trial functions themselves were mutually orthogonal, the modes are also mutually orthogonal, and therefore form an orthogonal basis. The solution to Equations (4.1a) and (4.1b) can thus be expressed in the following form

$$\mathbf{u}_1(r,\phi,t) = \sum_{m=1}^{\infty} \mathbf{U}_1^{(m)}(r,\phi)\eta^{(m)}(t) \tag{4.28a}$$

$$\mathbf{u}_2(r,\phi,t) = \sum_{m=1}^{\infty} \mathbf{U}_2^{(m)}(r,\phi)\eta^{(m)}(t) \tag{4.28b}$$

where $\eta^{(m)}(t)$ represents the modal coordinates. Substitution of Equations (4.28a) and (4.28b) into Equations (4.1a) and (4.1b), while exploiting the mutual orthogonality of the modes, reduces the system of coupled partial differential equations to a system of uncoupled ordinary differential equations; one for each mode. The reduced system of equations takes the form

$$\tilde{m}^{(m)}\ddot{\eta}(t) + \tilde{c}^{(m)}\dot{\eta}(t) + \tilde{k}^{(m)}\eta(t) = \tilde{F}^{(m)}(t), \tag{4.29}$$

where

$$\tilde{m}^{(m)} = \iint\limits_{A_1} \mathbf{U}_1^{(m)^T}(r,\phi)\mathbf{m}_1\mathbf{U}_1^{(m)}(r,\phi)dA + \iint\limits_{A_2} \mathbf{U}_2^{(m)^T}(r,\phi)\mathbf{m}_2\mathbf{U}_2^{(m)}(r,\phi)dA \tag{4.30a}$$

is the modal mass for the m^{th} mode,

$$\begin{aligned}\tilde{k}^{(m)} &= \iint\limits_{A_1} \mathbf{U}_1^{(m)^T}(r,\phi)\mathbf{k}_1\mathbf{U}_1^{(m)}(r,\phi)dA + \iint\limits_{A_2} \mathbf{U}_2^{(m)^T}(r,\phi)\mathbf{k}_2\mathbf{U}_2^{(m)}(r,\phi)dA \\ &= \tilde{k}_1^{(m)} + \tilde{k}_2^{(m)} \\ &= {\omega^{(m)}}^2\tilde{m}^{(m)}\end{aligned} \tag{4.30b}$$

is the modal stiffness for the m^{th} mode,

$$\begin{aligned}\tilde{c}^{(m)} &= \iint\limits_{A_1} \mathbf{U}_1^{(m)^T}(r,\phi)\mathbf{c}_1\mathbf{U}_1^{(m)}(r,\phi)dA + \iint\limits_{A_2} \mathbf{U}_2^{(m)^T}(r,\phi)\mathbf{c}_2\mathbf{U}_2^{(m)}(r,\phi)dA \\ &= \mu_1\tilde{k}_1^{(m)} + \mu_2\tilde{k}_2^{(m)}\end{aligned} \tag{4.30c}$$

is the modal damping factor for the m^{th} mode, and

$$\tilde{F}^{(m)} = \iint\limits_{A_1} \mathbf{U}_1^{(m)^T}(r,\phi)\mathbf{F}_1(r,\phi)dA + \iint\limits_{A_2} \mathbf{U}_2^{(m)^T}(r,\phi)\mathbf{F}_2(r,\phi)dA \tag{4.30d}$$

is the modal force for the m^{th} mode.

The solution to Equation (4.29) depends on whether the particular mode is overdamped or underdamped. For an overdamped mode, $\eta^{(m)}(t)$ takes the same form as Equation (3.25) for the constrained 2D model:

$$\begin{aligned}\eta^{(m)}(t) = &-\int_0^t \left(a_0^{(m)} + a_1^{(m)}\tau + a_2^{(m)}\tau^2 + a_3^{(m)}\tau^3\right) e^{-\zeta^{(m)}\omega^{(m)}(t-\tau)} \frac{\sinh\left[\omega^{(m)}z^{(m)}\left(t-\tau\right)\right]}{\tilde{m}^{(m)}\omega^{(m)}\tilde{z}^{(m)}} d\tau \\ &- \int_{t-t_s}^t \left[a_0^{(m)} + a_1^{(m)}\left(t-\tau\right) + a_2^{(m)}\left(t-\tau\right)^2 + a_3^{(m)}\left(t-\tau\right)^3\right] e^{-\zeta^{(m)}\omega^{(m)}\tau} \frac{\sinh\left(\omega^{(m)}z^{(m)}\tau\right)}{\tilde{m}^{(m)}\omega^{(m)}\tilde{z}^{(m)}} d\tau,\end{aligned} \tag{4.31}$$

where, for the present case,

$$a_0^{(m)} = 2c_2\tilde{F}^{(m)}, \tag{4.32a}$$

$$a_1^{(m)} = 6c_3\tilde{F}^{(m)}, \tag{4.32b}$$

$$a_2^{(m)} = 12c_4\tilde{F}^{(m)}, \tag{4.32c}$$

$$a_3^{(m)} = 20c_5\tilde{F}^{(m)}, \tag{4.32d}$$

$$\tilde{\zeta}^{(m)} = \frac{\tilde{c}^{(m)}}{2\omega^{(m)}\tilde{m}^{(m)}}, \tag{4.33a}$$

$$\tilde{z}^{(m)} = \sqrt{\tilde{\zeta}^{(m)\,2} - 1}. \tag{4.33b}$$

If, instead, the vibration mode of interest is underdamped, $\eta^{(m)}(t)$ takes the same form as Equation (3.28) for the constrained 2D model:

$$\begin{aligned}\eta^{(m)}(t) = &-\int_0^t \left(a_0^{(m)} + a_1^{(m)}\tau + a_2^{(m)}\tau^2 + a_3^{(m)}\tau^3\right) e^{-\zeta^{(m)}\omega^{(m)}(t-\tau)} \frac{\sin\left[\omega_d^{(m)}(t-\tau)\right]}{\tilde{m}^{(m)}\omega_d^{(m)}} d\tau \\ &- \int_{t-t_s}^t \left[a_0^{(m)} + a_1^{(m)}(t-\tau) + a_2^{(m)}(t-\tau)^2 + a_3^{(m)}(t-\tau)^3\right] e^{-\zeta^{(m)}\omega^{(m)}\tau} \frac{\sin\left(\omega_d^{(m)}\tau\right)}{\tilde{m}^{(m)}\omega_d^{(m)}} d\tau,\end{aligned} \tag{4.34}$$

where

$$\omega_d^{(m)} = \sqrt{1 - \tilde{\zeta}^{(m)\,2}}. \tag{4.35}$$

The displacement field can now be expressed semi-analytically by Equations (4.28a) and (4.28b). Substitution of these equations into Equations (4.14) and (4.15) will determine the location of boundary C_4 and, consequently, of detachment points a and b.

4.2 Results and Discussion

With a robust quasi-analytical solution for the model of the vitreous during a typical saccade having been determined, the results for typical scenarios are analyzed and compared to those determined by the constrained 2D model. The same material and geometric properties of the previous model are used. From this analysis, new light is shed on the behavior of the vitreous during typical saccades. The two models are compared side-by-side. By doing this, the more subtle implications of the constraint in the original model become illuminated.

4.2.1 Natural Frequencies

As previously shown, the natural frequencies of the vitreous body are determined as the real square roots of the eigenvalues of Equation (4.22). As was the case with the constrained 2D model, the natural frequencies change as the system evolves. When the boundary C_4 recedes, the system inherently becomes a new system, and therefore will oscillate at different natural frequencies. Figure 4.1b depicts the lowest eighteen natural frequencies as a function of detachment size for the current full 2D model. In Figure 4.1, these frequencies are compared to those for the constrained 2D model of Chapter 3 (Figure 4.1a). It can be seen that for the current full 2D model, the natural frequencies are always lower than their counterpart for the constrained 2D model. The added degrees of freedom in the current model allows the vitreous to be more compliant, and thus lowers the natural frequencies. Similar qualitative behavior is observed between the two models, particularly for lower natural frequencies and for larger detachment. For both models, the natural frequencies converge towards one of three values for large detachment size. Once again, the frequencies are lowered for larger detachment due to the structure becoming more compliant as detachment progresses.

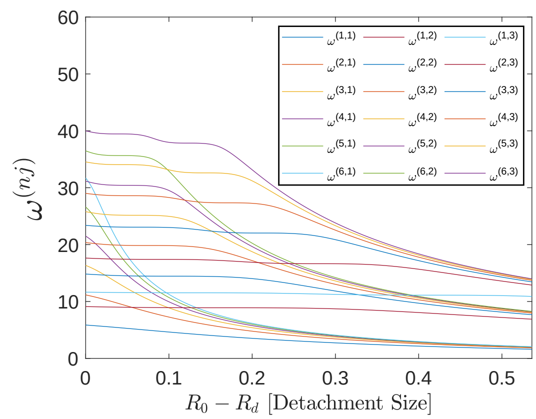

(a) **Constrained 2D Model.** Determined numerically as the solution to an analytical equation.

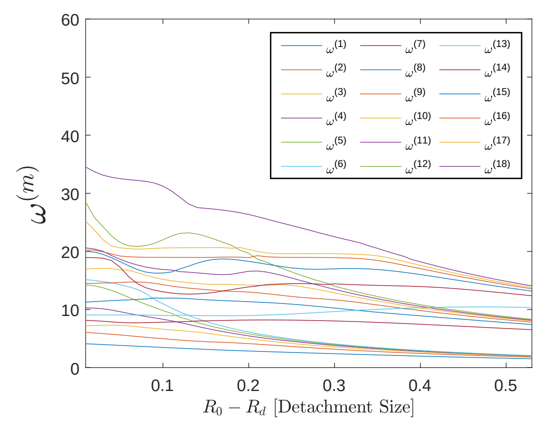

(b) **Full 2D Model.** Determined numerically as the solution to approximate equations determined by use of the Rayleigh-Ritz Method.

Figure 4.1: Comparison of the natural frequencies as determined by the two models.

4.2.2 Mode Shapes

Substitution of the natural frequencies, determined by the Rayleigh-Ritz method, back into Equation (4.22) yields the values for the constants $C_p^{(m;nj)}$ where $p = u, v$. Like the natural frequencies, these constants which determine the relative contribution of each trial function for each mode, change with detachment size. Appendix A shows the values of these constants yielded by the Rayleigh-Ritz method for three different detachment sizes: small, medium, and large. These constants are substituted into Equation (4.20) to yield the vibration modes for the system. For a detachment size of $R_0 - R_d = 0.236$, the circumferential components of the lowest eighteen modes are depicted by Figures 4.2 and 4.3, while the radial components of these modes are shown in Figures 4.4 and 4.5.

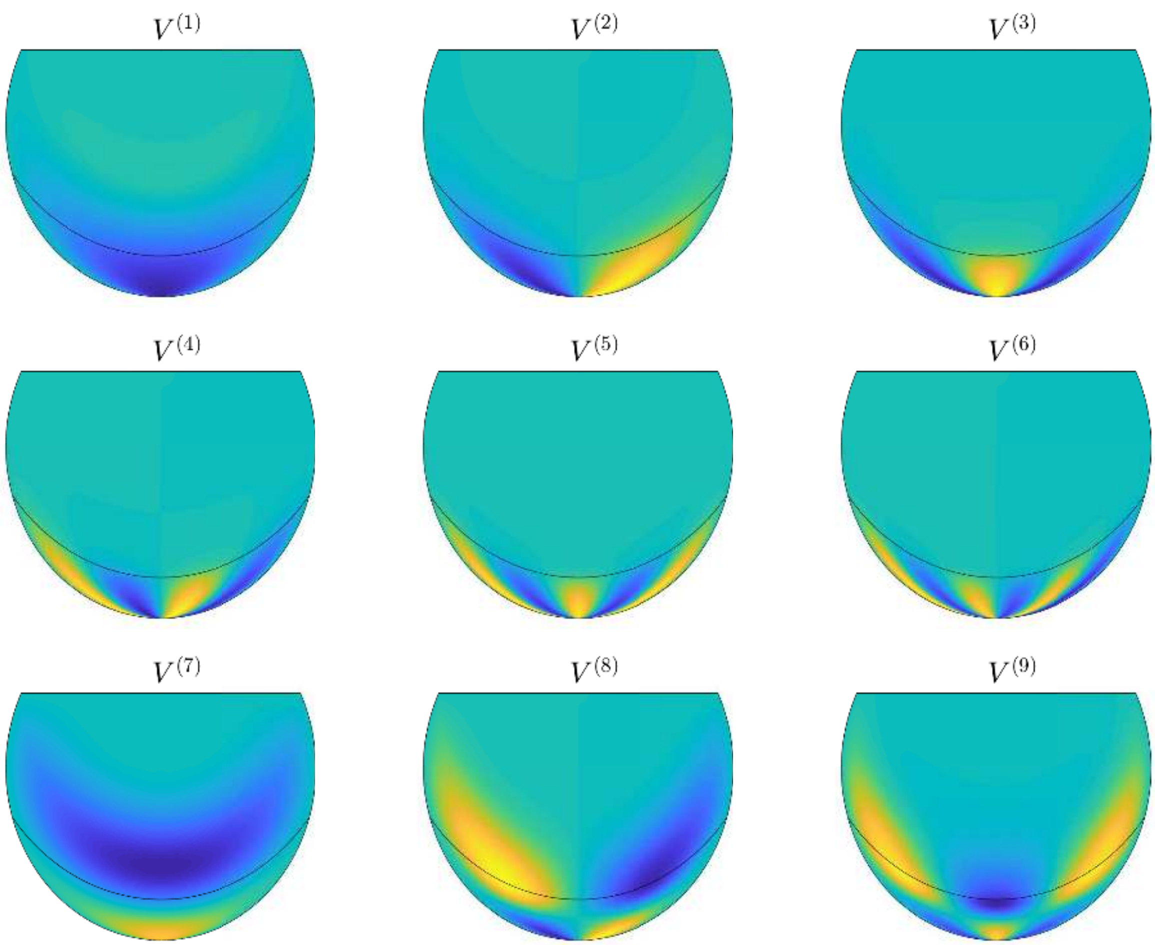

Figure 4.2: Circumferential component of Modes 1 - 9.

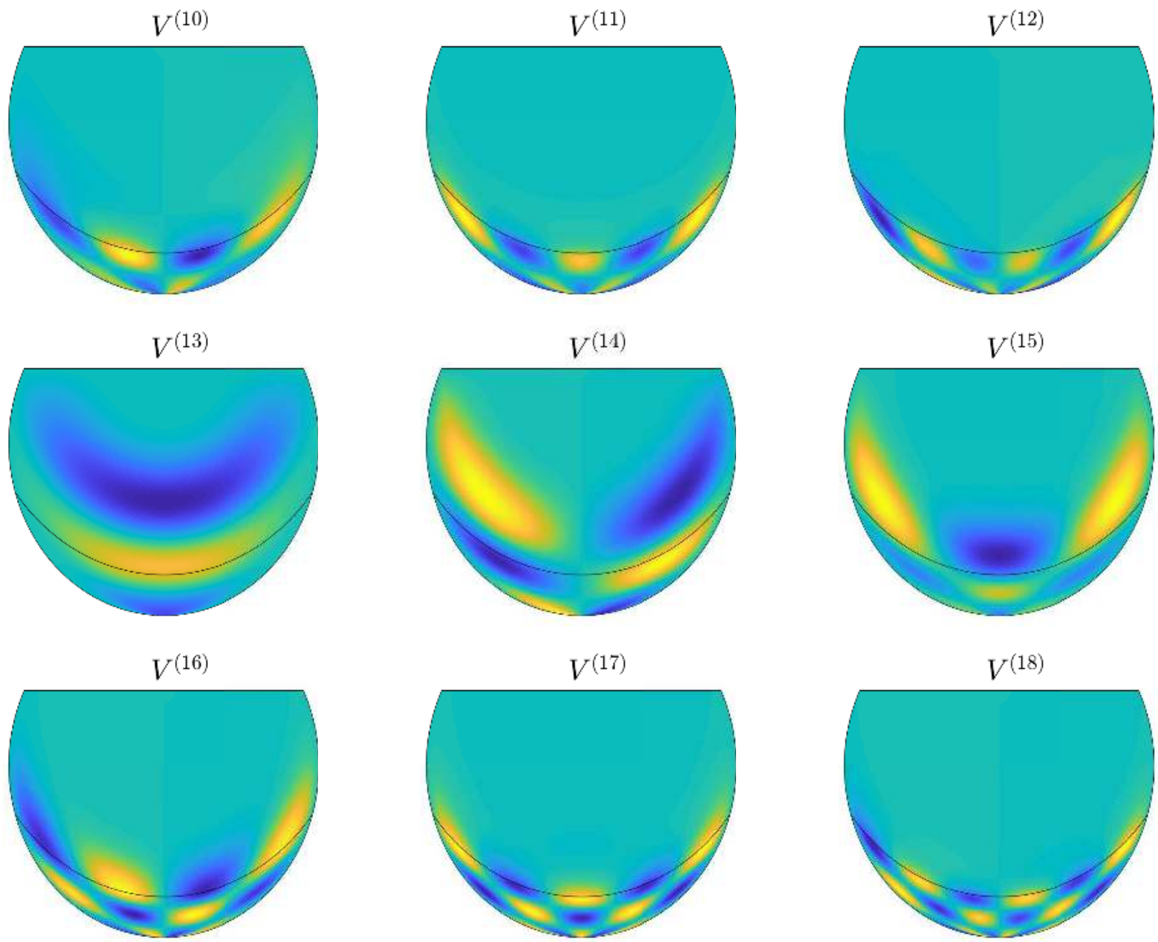

Figure 4.3: Circumferential component of Modes 10 - 18.

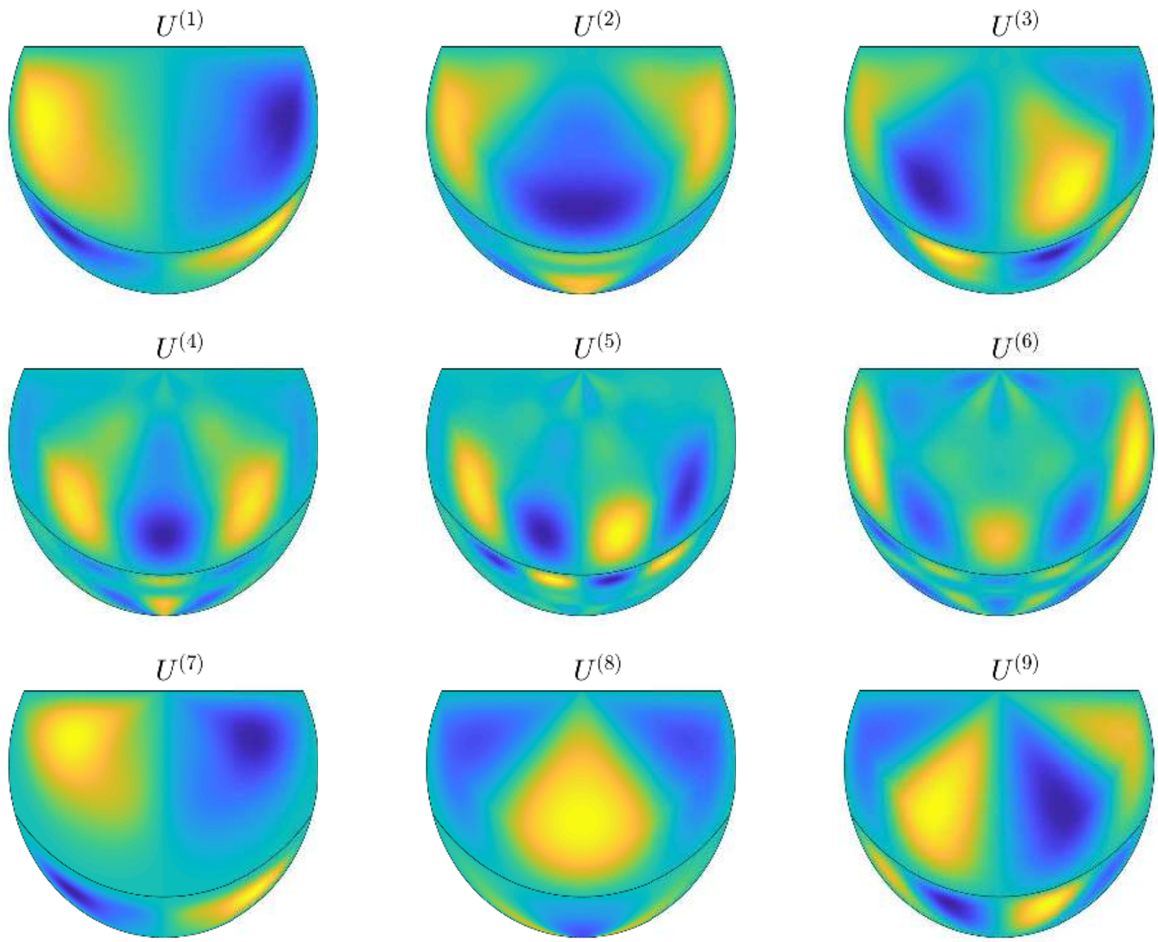

Figure 4.4: Radial component of Modes 1 - 9.

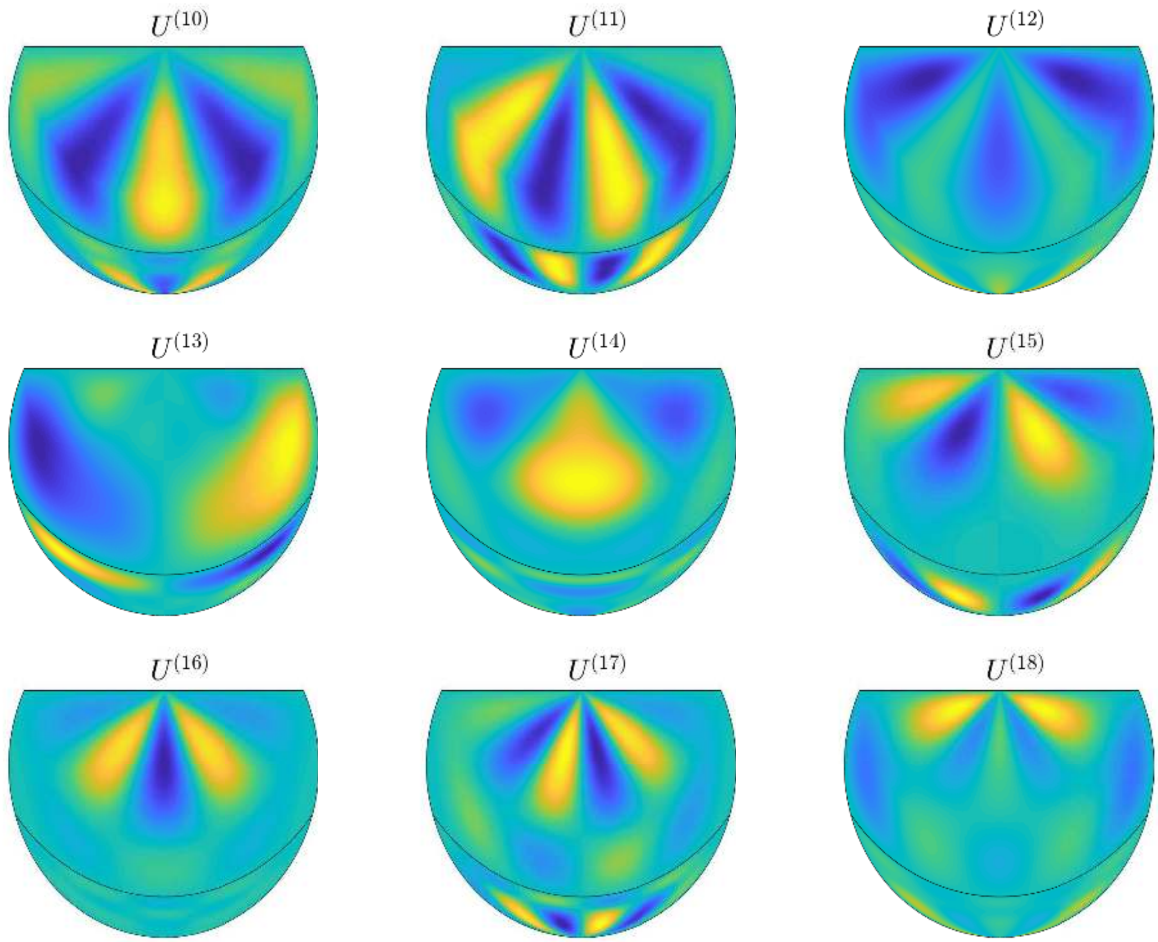

Figure 4.5: Radial component of Modes 10 - 18.

Table A.2 shows the constants, $C_p^{(m;nj)}$, determined by the Rayleigh-Ritz method. The dominant values are highlighted, and each correspond to a distinct trial function, which corresponds to a distinct mode from the constrained 2D model. Thus, for the current full 2D model, the lowest eighteen modes each correspond most closely with one of the modes determined by the constrained 2D model of Chapter 3. This shows that the assumption of the constrained 2D model was valid—that circumferential motion is the dominant motion of the vitreous during a saccade. In the full 2D model, the radial component for each mode is much smaller than the circumferential component, however its contribution is not insignificant. For the lowest eighteen modes of the full 2D model, Figures 4.6 – 4.23 show a direct comparison between these full 2D modes and the dominant constrained 2D mode for each full 2D mode. The circumferential modes are virtually identical, though some are in the opposite direction due to the arbitrary constant associated with the mode shapes.

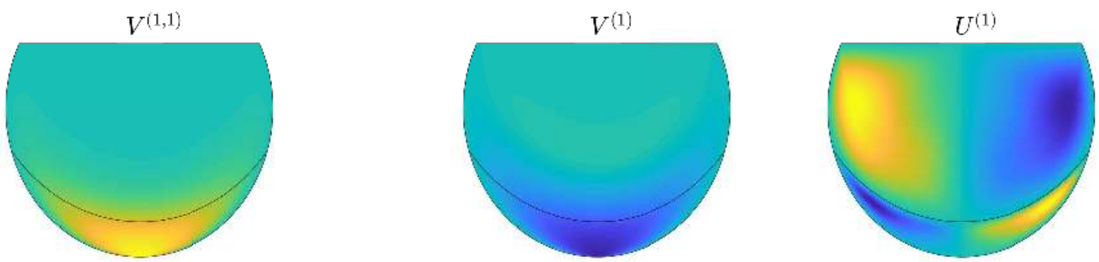

(a) Constrained 2D model (b) Full 2D model

Figure 4.6: Comparison of Mode 1 of the full 2D model with Mode (1,1) of the circumferential model for detachment size $R_0 - R_d = 0.236$.

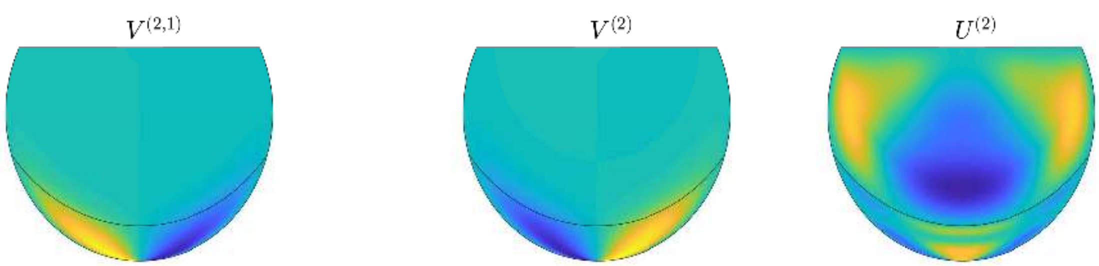

(a) Constrained 2D model (b) Full 2D model

Figure 4.7: Comparison of Mode 2 of the full 2D model with Mode (2,1) of the circumferential model for detachment size $R_0 - R_d = 0.236$.

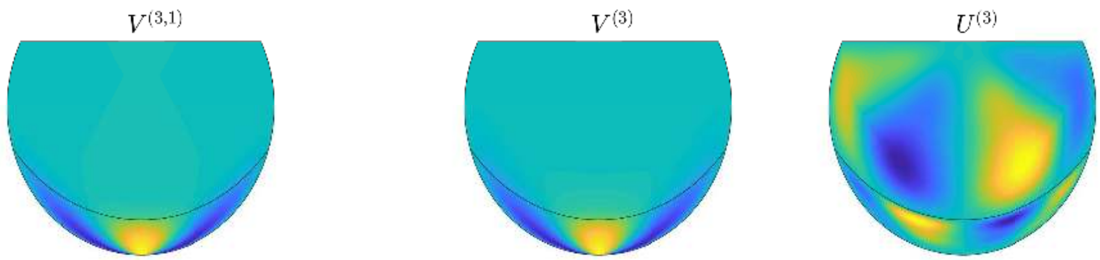

(a) Constrained 2D model (b) Full 2D model

Figure 4.8: Comparison of Mode 3 of the full 2D model with Mode (3,1) of the circumferential model for detachment size $R_0 - R_d = 0.236$.

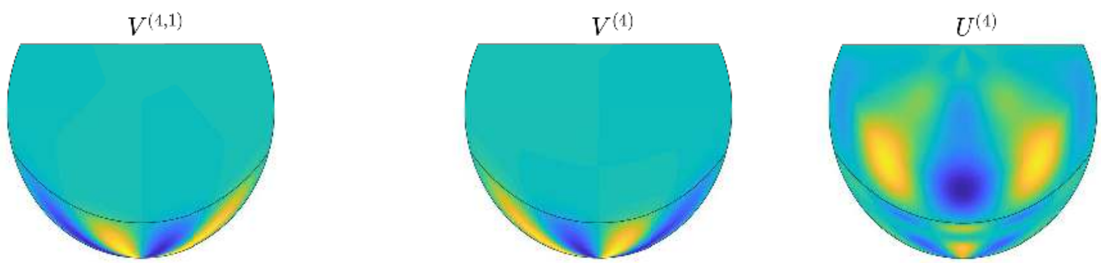

(a) Constrained 2D model (b) Full 2D model

Figure 4.9: Comparison of Mode 4 of the full 2D model with Mode (4,1) of the circumferential model for detachment size $R_0 - R_d = 0.236$.

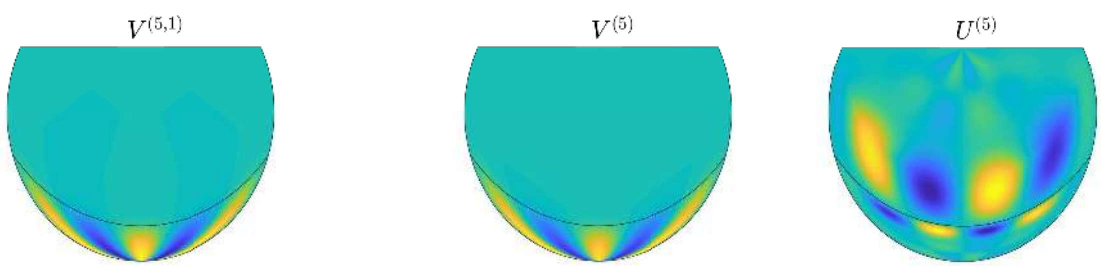

(a) Constrained 2D model (b) Full 2D model

Figure 4.10: Comparison of Mode 5 of the full 2D model with Mode (5,1) of the circumferential model for detachment size $R_0 - R_d = 0.236$.

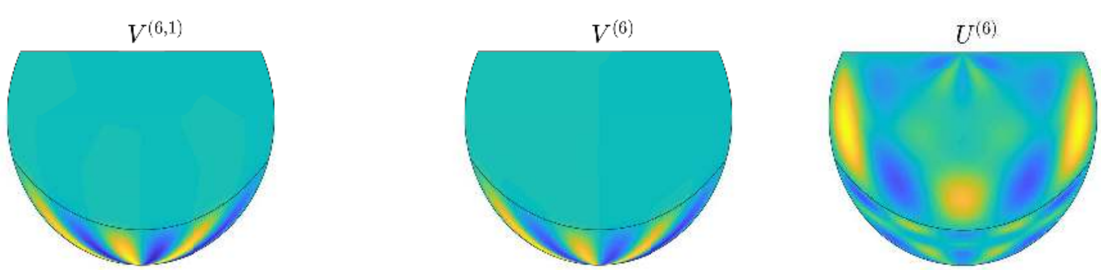

(a) Constrained 2D model (b) Full 2D model

Figure 4.11: Comparison of Mode 6 of the full 2D model with Mode (6,1) of the circumferential model for detachment size $R_0 - R_d = 0.236$.

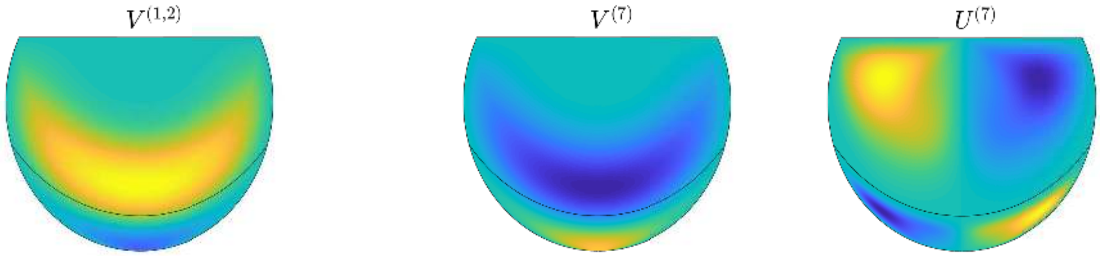

(a) Constrained 2D model

(b) Full 2D model

Figure 4.12: Comparison of Mode 7 of the full 2D model with Mode (1,2) of the circumferential model for detachment size $R_0 - R_d = 0.236$.

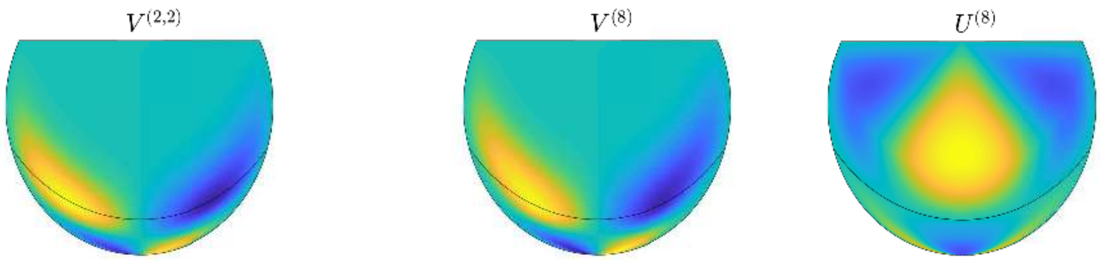

(a) Constrained 2D model

(b) Full 2D model

Figure 4.13: Comparison of Mode 8 of the full 2D model with Mode (2,2) of the circumferential model for detachment size $R_0 - R_d = 0.236$.

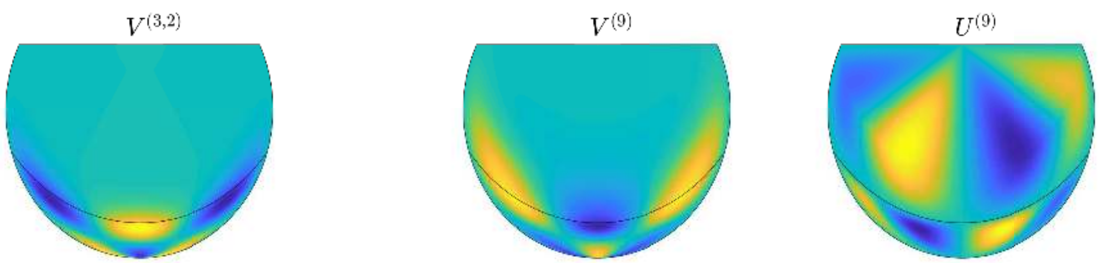

(a) Constrained 2D model

(b) Full 2D model

Figure 4.14: Comparison of Mode 9 of the full 2D model with Mode (3,2) of the circumferential model for detachment size $R_0 - R_d = 0.236$.

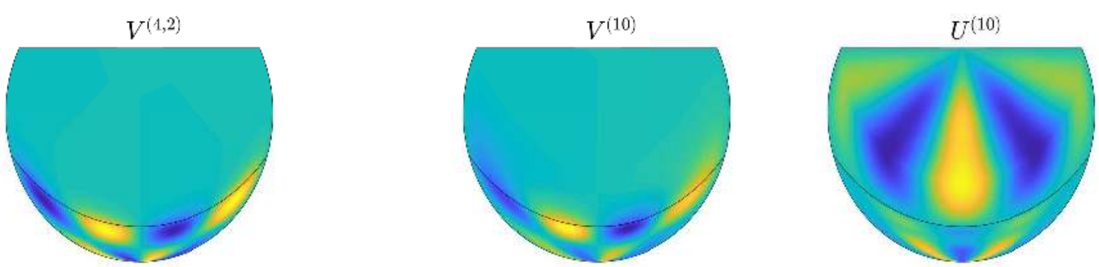

(a) Constrained 2D model

(b) Full 2D model

Figure 4.15: Comparison of Mode 10 of the full 2D model with Mode (4,2) of the circumferential model for detachment size $R_0 - R_d = 0.236$.

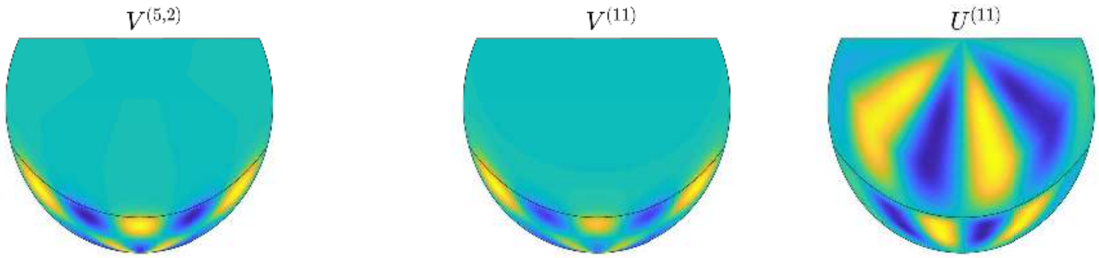

(a) Constrained 2D model (b) Full 2D model

Figure 4.16: Comparison of Mode 11 of the full 2D model with Mode (5,2) of the circumferential model for detachment size $R_0 - R_d = 0.236$.

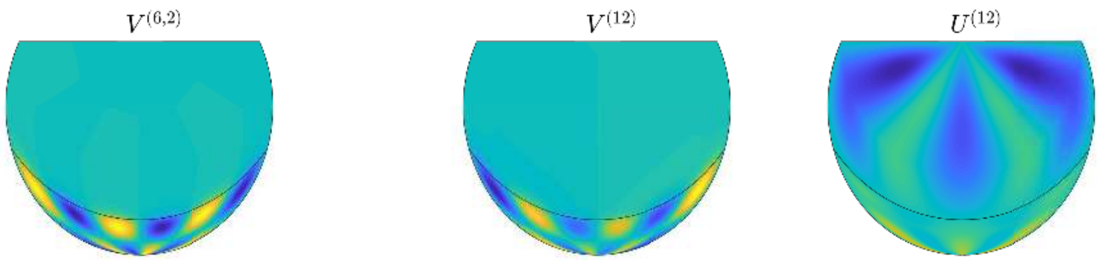

(a) Constrained 2D model (b) Full 2D model

Figure 4.17: Comparison of Mode 12 of the full 2D model with Mode (6,2) of the circumferential model for detachment size $R_0 - R_d = 0.236$.

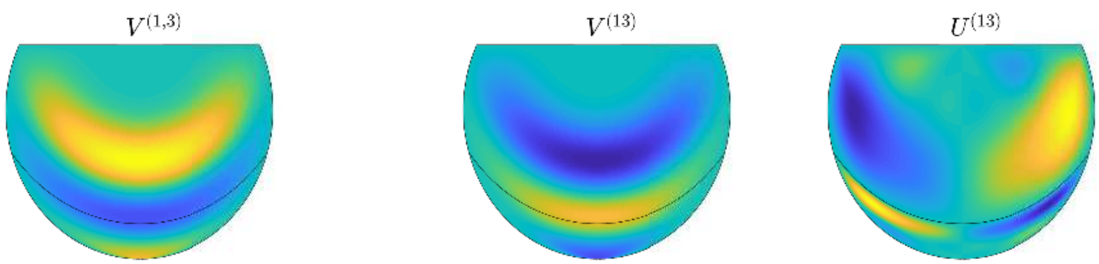

(a) Constrained 2D model (b) Full 2D model

Figure 4.18: Comparison of Mode 13 of the full 2D model with Mode (1,3) of the circumferential model for detachment size $R_0 - R_d = 0.236$.

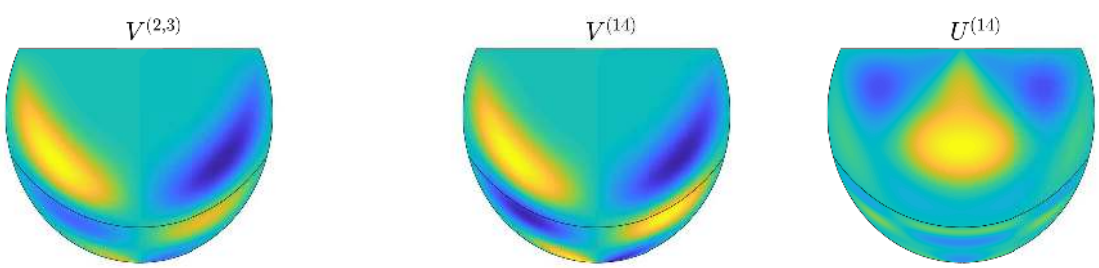

(a) Constrained 2D model (b) Full 2D model

Figure 4.19: Comparison of Mode 14 of the full 2D model with Mode (2,3) of the circumferential model for detachment size $R_0 - R_d = 0.236$.

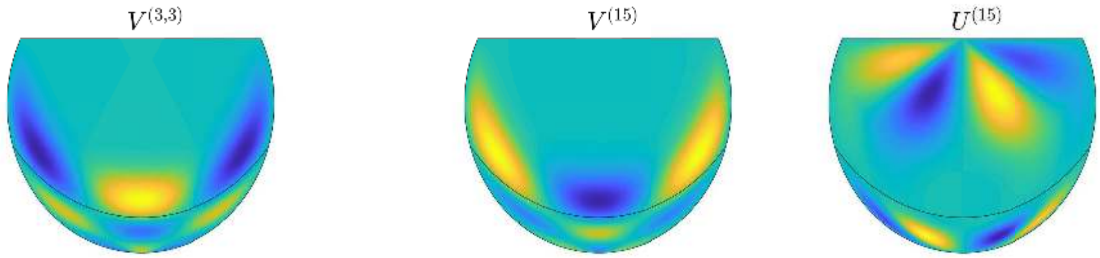

(a) Constrained 2D model (b) Full 2D model

Figure 4.20: Comparison of Mode 15 of the full 2D model with Mode (3,3) of the circumferential model for detachment size $R_0 - R_d = 0.236$.

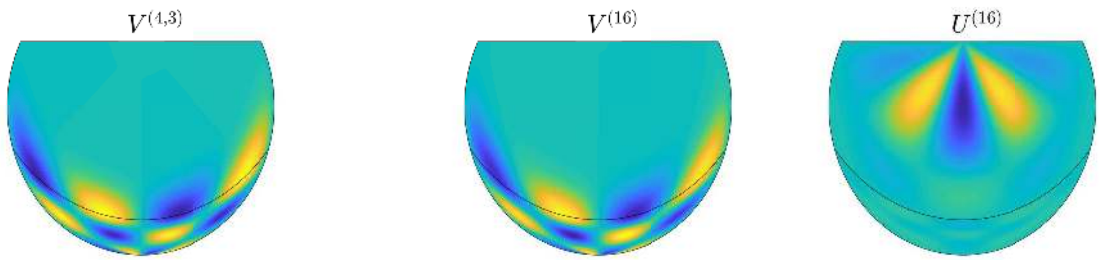

(a) Constrained 2D model (b) Full 2D model

Figure 4.21: Comparison of Mode 16 of the full 2D model with Mode (4,3) of the circumferential model for detachment size $R_0 - R_d = 0.236$.

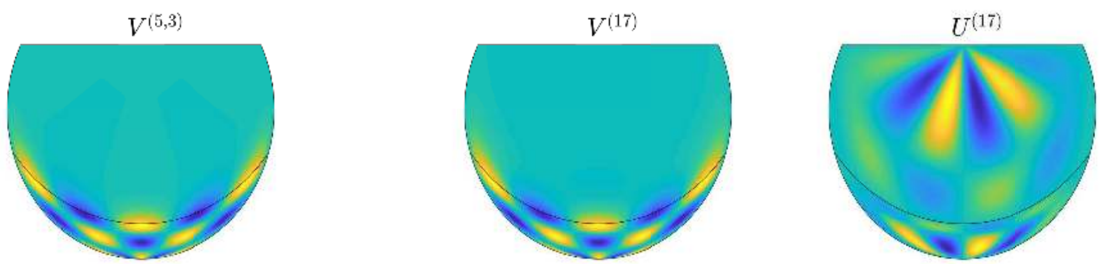

(a) Constrained 2D model (b) Full 2D model

Figure 4.22: Comparison of Mode 17 of the full 2D model with Mode (5,3) of the circumferential model for detachment size $R_0 - R_d = 0.236$.

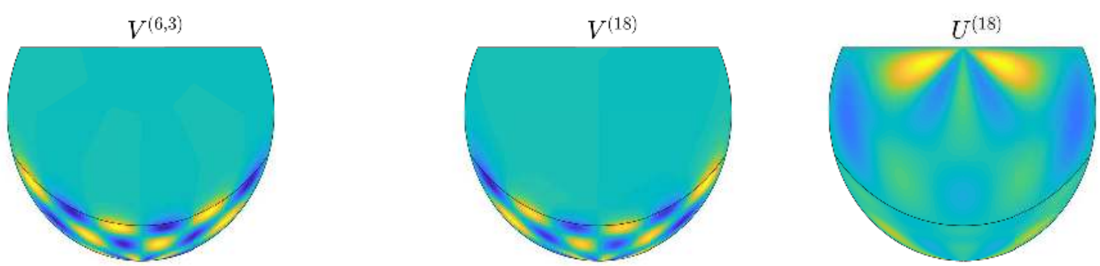

(a) Constrained 2D model (b) Full 2D model

Figure 4.23: Comparison of Mode 18 of the full 2D model with Mode (6,3) of the circumferential model for detachment size $R_0 - R_d = 0.236$.

4.2.3 Relative Contribution of Modes

With the material properties being the same as those used in Chapter 3 for the constrained 2D model, the vibration modes are again all overdamped. Thus, the contribution of each mode, as a function of time, during a saccade is given by Equation (4.31), where the integral has been evaluated analytically. Figures 4.24 – 4.26 show the relative contribution of each mode shape as a function of time for various detachment sizes and saccade amplitudes. These figures show that contributions of the even numbered modes are negligible for all saccades and detachment sizes. This is because the modal forces given by Equation (4.30d) vanish for these modes. As was shown in the previous section, the even numbered modes correspond with the anti-symmetric modes of the constrained 2D model, which are never excited during saccadic motion. Just like what was observed for the constrained 2D model, it is seen that in the full 2D model the motion is dominated by the fundamental mode. The modal contributions, and thus the total motion of the vitreous increases with both detachment size and saccade amplitude, as observed for the previous model.

Figure 4.27 compares the modal contribution between the full 2D model and the constrained 2D model for a 20° saccade with detachment size $R_0 - R_d = 0.036$. It can be seen that the full 2D model has slightly larger contributions from its modes compared to the constrained 2D model. This corresponds to more motion, which makes sense as this structure no longer has artificial constraints on its motion, and is thus more compliant. It is interesting to note the order of relative model contribution. Figure 4.27b shows that Mode 1 contributes the most, followed by Mode 3, Mode 5, and then Mode 7, while contributions from the rest are quite small in comparison. As was discussed in the previous section, these modes would correspond in the constrained 2D model to Mode (1,1), Mode (3,1), Mode (5,1), and Mode (1,2), respectively. However Figure 4.27a shows that the relative order of contribution is Mode (1,1), Mode (3,1), Mode (1,2), and then Mode (5,1). That is to say that the relative contribution of Mode (1,2) is larger than that of Mode (5,1) in the constrained 2D model, but the opposite is true in the full 2D model.

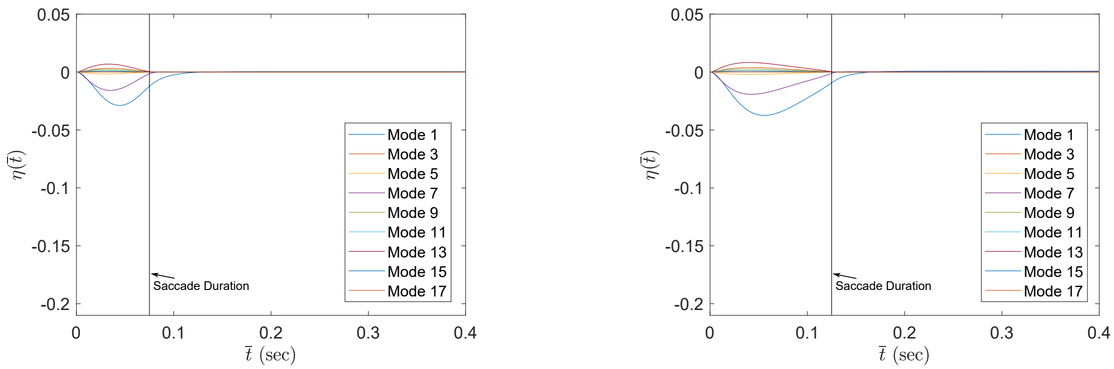

(a) Detachment size: $R_0 - R_d = 0.036$;
Saccade amplitude: 20°

(b) Detachment size: $R_0 - R_d = 0.036$;
Saccade amplitude: 40°

Figure 4.24: Modal contribution as a function of dimensional time for small detachment.

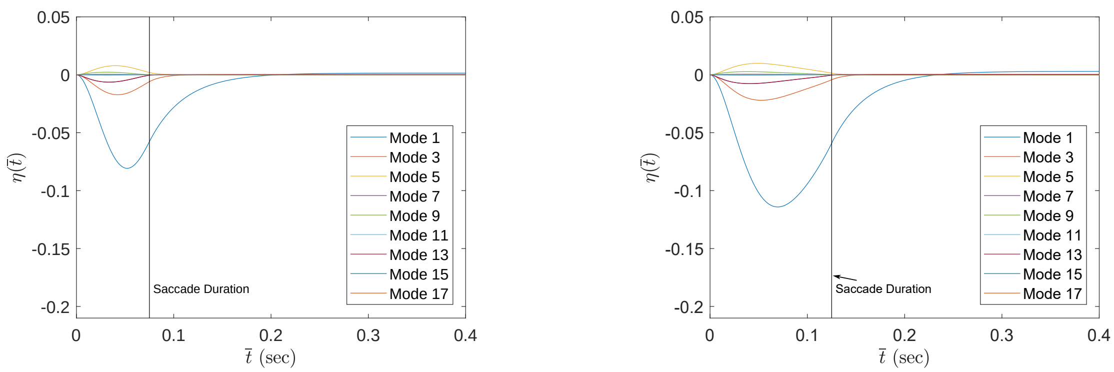

(a) Detachment size: $R_0 - R_d = 0.236$;
Saccade amplitude: 20°

(b) Detachment size: $R_0 - R_d = 0.236$;
Saccade amplitude: 40°

Figure 4.25: Modal contribution as a function of dimensional time for medium detachment.

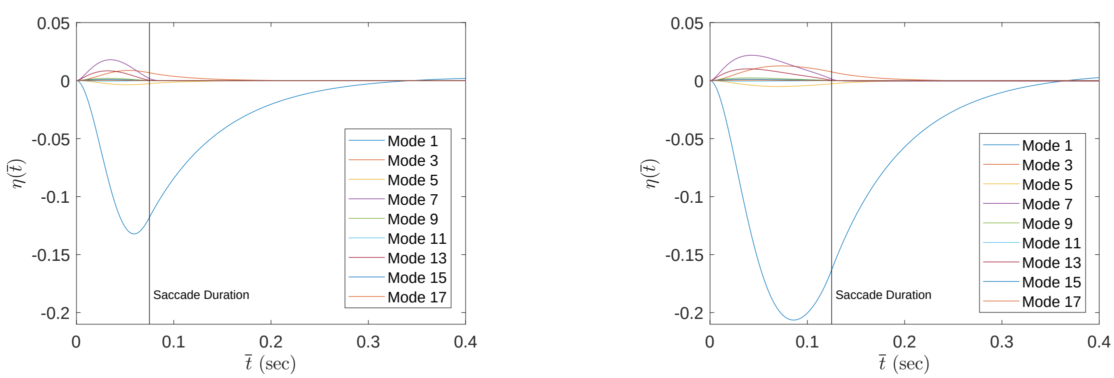

(a) Detachment size: $R_0 - R_d = 0.436$;
Saccade amplitude: 20°

(b) Detachment size: $R_0 - R_d = 0.436$;
Saccade amplitude: 40°

Figure 4.26: Modal contribution as a function of dimensional time for large detachment.

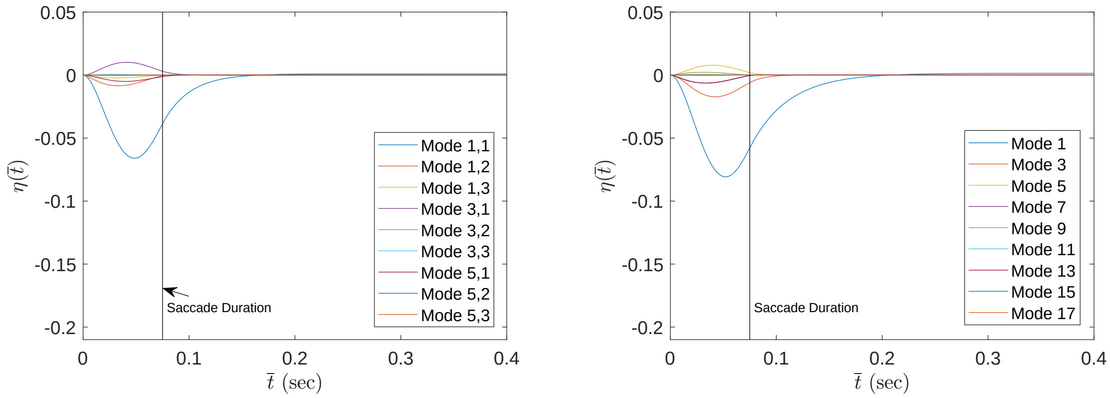

(a) Constrained 2D Model (b) Full 2D Model

Figure 4.27: Comparison of the modal contribution between the two models for a 20° saccade with detachment size $R_0 - Rd = 0.236$.

4.2.4 Vitreous Response Fields

The radial and circumferential components of the displacement response, $u(r, \phi, t)$ and $v(r, \phi, t)$, respectively, of the partially detached vitreous body subject to saccadic motion are given by Equations (4.28a) and (4.28b). The response of an eye with vitreous detachment size $R_0 - R_d = 0.236$ subject to a 20° saccade is presented, and compared to that of the constrained 2D model. Figure 4.28b shows the maximum displacement field during the saccade, which occurs at an instant just before the saccade is at its peak acceleration. For the 20° saccade shown, this corresponds to $\bar{t} = 0.051$ sec. It can be seen that the dominant motion is in the circumferential direction, as the response is one order of magnitude larger than the radial direction. This validates the original hypothesis of the constrained 2D model. However, it can be seen when comparing the response to that of the constrained 2D model, shown in Figure 4.28a, that the circumferential displacement response of the full 2D model is significantly larger in Region S_2. This is a consequence of the presence of artificial constraining forces in the constrained 2D model necessary to prohibit radial motion. Not only does the radial motion vanish in the constrained 2D model, but the circumferential response is underestimated, as well. Figure 4.28b most closely resembles Mode 1, as this is the dominant mode during motion.

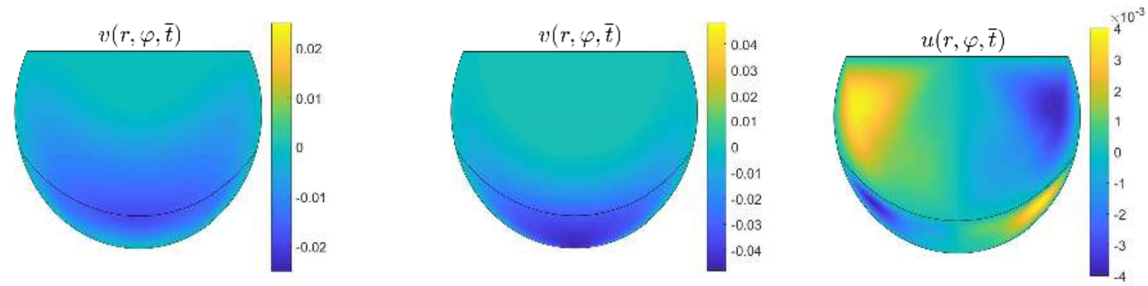

(a) Constrained 2D model (b) Full 2D Model

Figure 4.28: Comparison of maximum displacement of the vitreous during a 20° saccade with detachment size $R_0 - R_d = 0.236$ for the constrained 2D model to the full 2D model.

Figures 4.29, 4.30, and 4.31 compare the stress fields of the full 2D model to the constrained 2D model (both excluding the uniform stress due to the IOP), at the time of peak response and at the end of the saccade. The effect of the artificial constraining force in the constrained 2D model is even more apparent here. The total normal stresses, $\sigma_{\phi\phi}^{(T)}$ and $\sigma_{rr}^{(T)}$, are quite different between the two models. Figures 4.29b and 4.30b show that in the full 2D model the normal stress peaks at the detachment points a and b, as compared to the constrained 2D model where normal stresses peak at the vitreous base, as shown in Figures 4.29a and 4.30a. This result is similar to the 2011 numerical study by Repetto et al. [42], which observed maximum values of deviatoric stress near detachment points a and b. The magnitude of maximum normal stress is also slightly larger in the full 2D model, though the location of the stress differs. However, at the end of the saccade, the full 2D model actually yields lower stress than the constrained 2D model, as seen by comparing Figures 4.29d and 4.30d to Figures 4.29c and 4.30c, respectively. This suggests that the response dampens more quickly for the full 2D model.

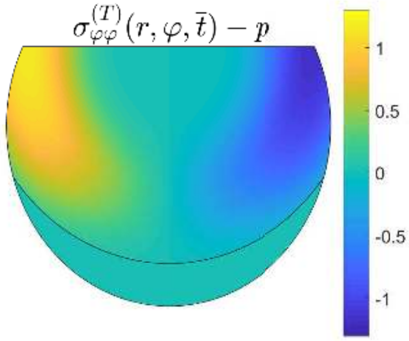

(a) **Constrained 2D model.** Maximum normal stress, $\sigma_{\phi\phi}$, occurs at $\bar{t} = 0.051$ sec.

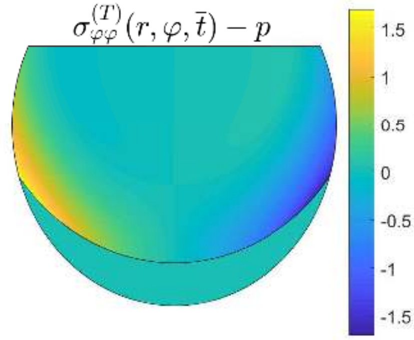

(b) **Full 2D model.** Maximum normal stress, $\sigma_{\phi\phi}$, occurs at $\bar{t} = 0.051$ sec.

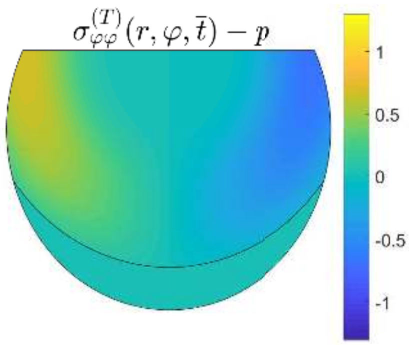

(c) **Constrained 2D model.** Normal stress, $\sigma_{\phi\phi}$, at the end of the saccade: $\bar{t}_s = 0.075$ sec.

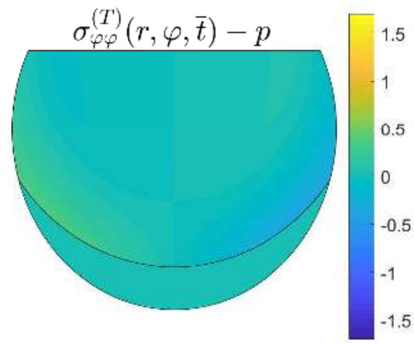

(d) **Full 2D model.** Normal stress, $\sigma_{\phi\phi}$, at the end of the saccade: $\bar{t}_s = 0.075$ sec.

Figure 4.29: Comparison of maximum normal stress, $\sigma_{\phi\phi}$, during a 20° saccade with detachment size, $R_0 - R_d = 0.236$ for the constrained 2D model to the full 2D model.

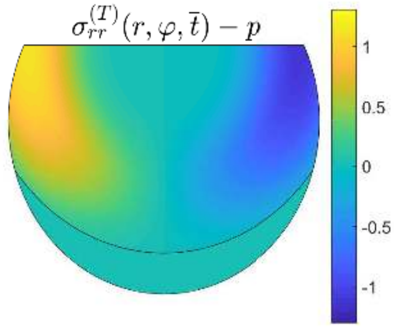

(a) **Constrained 2D model.** Maximum normal stress, σ_{rr}, occurs at $\bar{t} = 0.051$ sec.

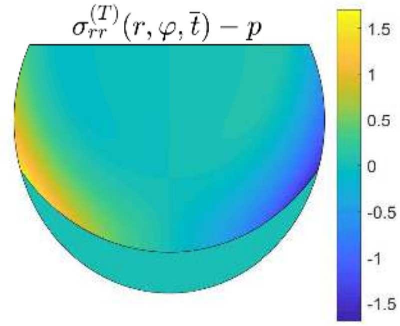

(b) **Full 2D model.** Maximum normal stress, σ_{rr}, occurs at $\bar{t} = 0.051$ sec.

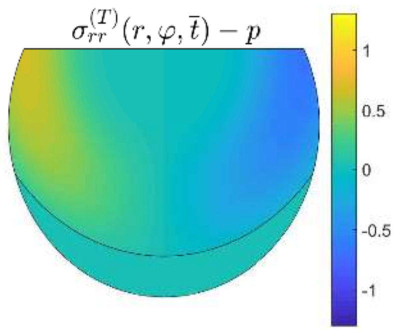

(c) **Constrained 2D model.** Normal stress, σ_{rr}, at the end of the saccade: $\bar{t}_s = 0.075$ sec.

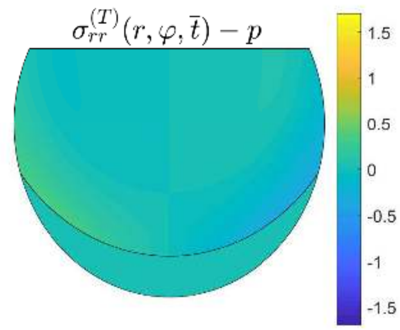

(d) **Full 2D model.** Normal stress, σ_{rr}, at the end of the saccade: $\bar{t}_s = 0.075$ sec.

Figure 4.30: Comparison of normal stress, σ_{rr}, during a 20° saccade with detachment size, $R_0 - R_d = 0.236$ for the constrained 2D model to the full 2D model.

Figure 4.31 compares shear stress between the two models. Once again, the same behavior is seen as for the normal stresses where the peak value of the shear stress is slightly larger for the full 2D model, but is lower at the end of the saccade. However, what is very interesting is that the constrained model predicted that there is a large amount of shear stress in the interior part of the vitreous that is not predicted by the full 2D model shown in Figure 4.31b. This additional shear stress is therefore a consequence of the constraint on the radial motion in the constrained 2D model. It is once again observed that, for both of the models, the peak shear stress occurs along C_4—the boundary between Region S_1 and Region S_2.

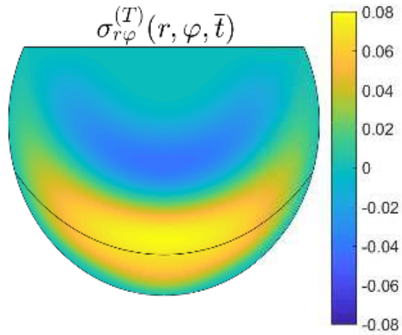

(a) **Constrained 2D model.** Maximum shear stress, $\sigma_{r\phi}$, occurs at $\bar{t} = 0.051$ sec.

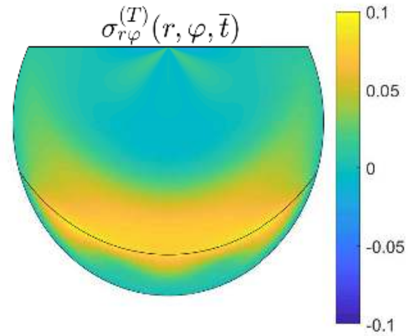

(b) **Full 2D model.** Maximum shear stress, $\sigma_{r\phi}$, occurs at $\bar{t} = 0.051$ sec.

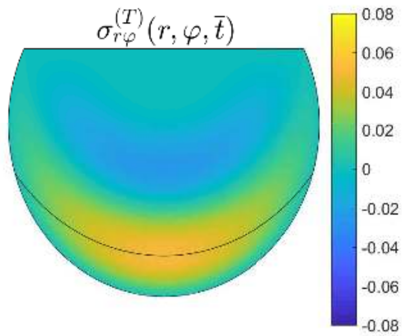

(c) **Constrained 2D model.** Shear stress, $\sigma_{r\phi}$, at the end of the saccade: $\bar{t}_s = 0.075$ sec.

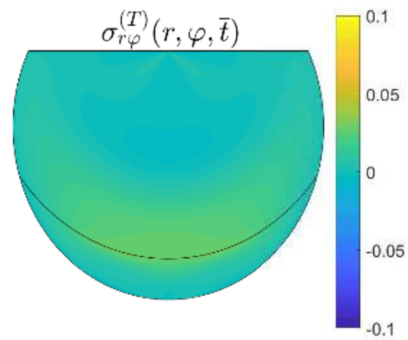

(d) **Full 2D model.** Shear stress, $\sigma_{r\phi}$, at the end of the saccade: $\bar{t}_s = 0.075$ sec.

Figure 4.31: Comparison of shear stress, $\sigma_{r\phi}$, during a 20° saccade with detachment size, $R_0 - R_d = 0.236$ for the constrained 2D model to the full 2D model.

The maximum resultant stress fields for detachment size, $R_0 - R_d = 0.236$ are plotted in Figures 4.32 – 4.35 for increasing amplitude of the saccade. Stresses $\sigma_{\phi\phi}^{(T)}$, $\sigma_{rr}^{(T)}$, and $\sigma_{r\phi}^{(T)}$ all increase as the saccade amplitude increases, as was seen with the constrained 2D model of Chapter 3. The general shape of the resultant stress fields remains the same for the current model, just with increasing magnitude proportional to the saccade amplitude.

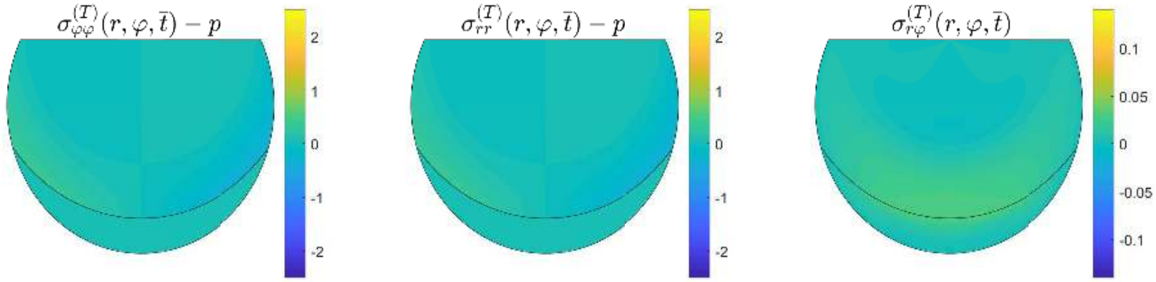

Figure 4.32: Maximum stress fields during a saccade of amplitude 10° with detachment size, $R_0 - R_d = 0.236$ as predicted by the full 2D model.

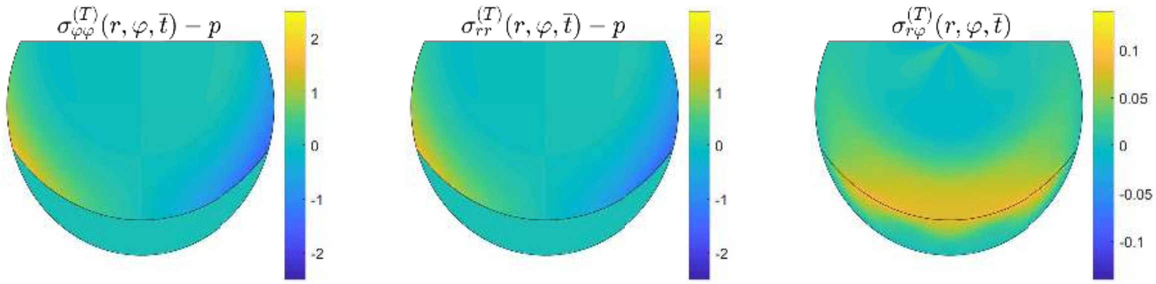

Figure 4.33: Maximum stress fields during a saccade of amplitude 20° with detachment size, $R_0 - R_d = 0.236$ as predicted by the full 2D model.

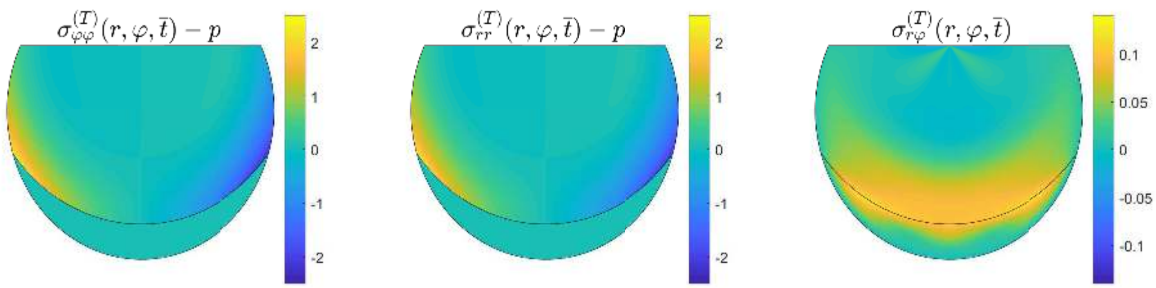

Figure 4.34: Maximum stress fields during a saccade of amplitude 30° with detachment size, $R_0 - R_d = 0.236$ as predicted by the full 2D model.

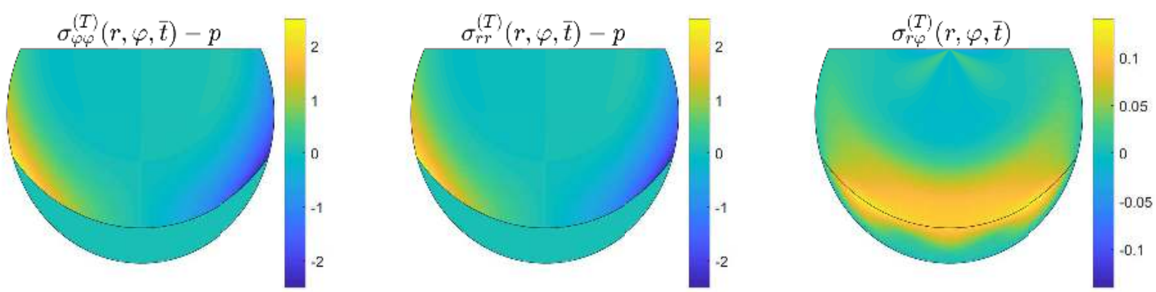

Figure 4.35: Maximum stress fields during a saccade of amplitude 40° with detachment size, $R_0 - R_d = 0.236$ as predicted by the full 2D model.

4.2.5 Detachment Progression

The pathology of the vitreo-retinal detachment boundary is governed by the transversality condition given by Equations (2.37) and (2.38), which locates boundaries a and b that correspond to configurations of the evolving ocular system that satisfy the dynamic conditions. For the full 2D model, after substitution of boundary conditions, along with the current selection of material properties, the transversality condition reduces to

$$\begin{aligned}\mathcal{G}\{R_d;a,b\} = &\left[\frac{G_1(1-\nu_1)}{(1-2\nu_1)}\frac{1}{r}\left(\frac{\partial v_1}{\partial\phi}+\mu_1\frac{\partial^2 v_1}{\partial t\partial\phi}\right)\frac{1}{r}\frac{\partial v_1}{\partial\phi}-\sigma_{nt}^{(T;1)}\frac{\partial u_1^{(t)}}{\partial s}+\sigma_{nt}^{(T;2)}\frac{\partial u_2^{(t)}}{\partial s}\right]\Bigg|_a \\ &+\left[\frac{G_1(1-\nu_1)}{(1-2\nu_1)}\frac{1}{r}\left(\frac{\partial v_1}{\partial\phi}+\mu_1\frac{\partial^2 v_1}{\partial t\partial\phi}\right)\frac{1}{r}\frac{\partial v_1}{\partial\phi}-\sigma_{nt}^{(T;1)}\frac{\partial u_1^{(t)}}{\partial s}+\sigma_{nt}^{(T;2)}\frac{\partial u_2^{(t)}}{\partial s}\right]\Bigg|_b \\ &+\left[\vec{e}_t\cdot-\vec{e}_r\right]\big|_{(a\text{ or }b)}\int_{C_4}\sigma_{rr}^{(T;1)}\frac{\partial u_1}{\partial r}ds = 2\gamma|_a+2\gamma|_b\,.\end{aligned} \tag{4.36}$$

Figure 4.36 compares the energy release rate per unit depth for both models as a function of time for saccades of various amplitudes, for three separate detachment sizes. It can be seen that the same trend exists for both models, where the amount of energy released during a saccade increases with detachment size. The energy release rate for all detachment sizes is shown as a function of detachment size in Figure 4.37. The energy release rate for the full 2D model is an order of magnitude larger than that of the constrained 2D model. There are two reasons for this disparity. Firstly, when looking at the two equations that govern energy release rate, it can be seen that the stresses at detachment boundaries a and b are a driving factor. As was previously observed, the full 2D model predicts much higher stress at a and b. Secondly, the transversality condition for the full 2D model given by (4.36), has an extra term that is not included in the transversality condition for the constrained 2D model given by Equation (3.30). This term represents the jump in energy across detached boundary C_4. This term is not included in the constrained 2D model because, as seen in Equation (4.36), it depends on the displacement in the radial direction, which vanishes as a result of the constraint. It is these two factors that cause the energy release rate to be much higher during a saccade for the full 2D model.

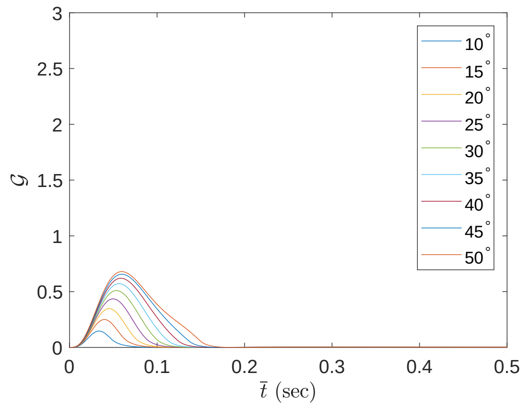

(a) **Constrained 2D model.**
Detachment size, $R_0 - R_d = 0.036$.

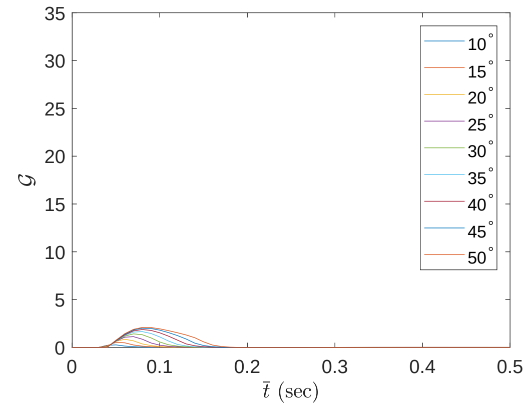

(b) **Full 2D model.**
Detachment size, $R_0 - R_d = 0.036$.

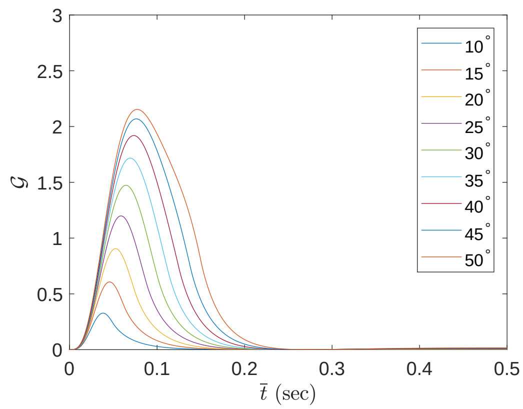

(c) **Constrained 2D model.**
Detachment size, $R_0 - R_d = 0.236$.

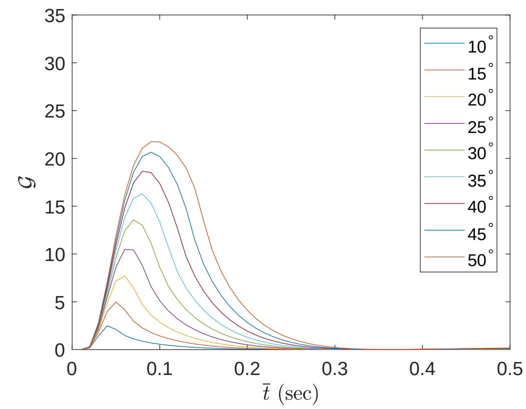

(d) **Full 2D model.**
Detachment size, $R_0 - R_d = 0.236$.

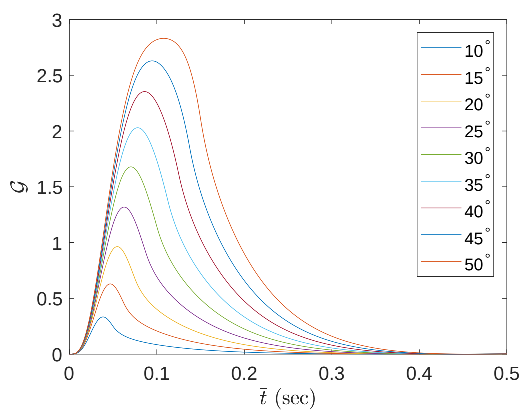

(e) **Constrained 2D model.**
Detachment size, $R_0 - R_d = 0.436$.

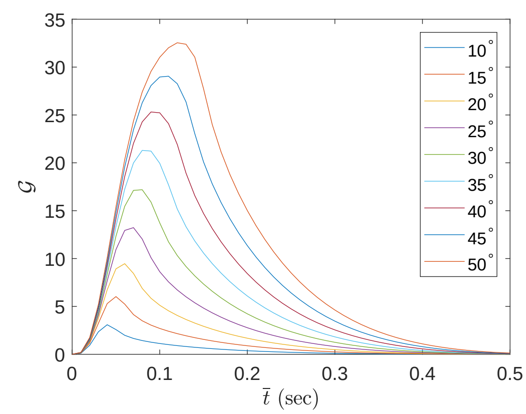

(f) **Full 2D model.**
Detachment size, $R_0 - R_d = 0.436$.

Figure 4.36: Comparison of energy release rate per unit depth as a function of time between the constrained 2D model and the full 2D model for small, medium, and large detachment size.

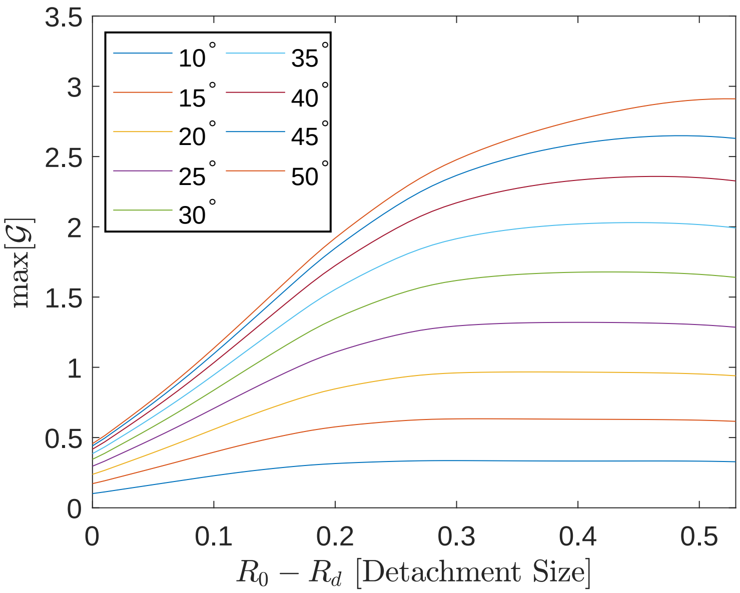

(a) Constrained 2D model.

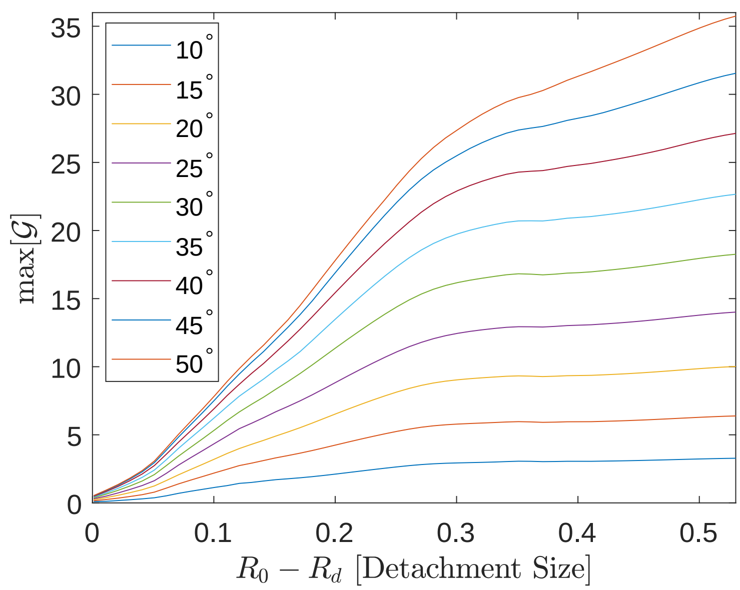

(b) Full 2D model

Figure 4.37: Comparison of the maximum energy release rate per unit depth as a function of detachment size between the two models for saccades of nine different amplitudes.

Figure 4.38 compares the threshold paths of the two models for the evolution of the propagating detachment boundaries. Again, these are plots of the critical saccade amplitude per unit bond energy, $\widetilde{A}_{cr}$, as a function of detachment size, where

$$\widetilde{A}_{cr} = \frac{A_{cr}}{2\gamma|_a + 2\gamma|_b}, \tag{4.37}$$

and A_{cr} is the critical saccade amplitude—the amplitude required to precipitate detachment. Figure 4.38 shows that for the full 2D model, the critical saccade amplitude is always lower than that of the constrained 2D model. The threshold path for the full 2D model decreases monotonically. This implies that, for any initial detachment size, if a saccade is large enough to cause further detachment, the detachment will grow continuously (unstably) until it reaches a point of abnormally strong adhesion between the vitreous cortex and the sensory retina. This differs from what is predicted by the constrained 2D model where detachment was seen to be stable (does not grow continuously) for large sized detachments.

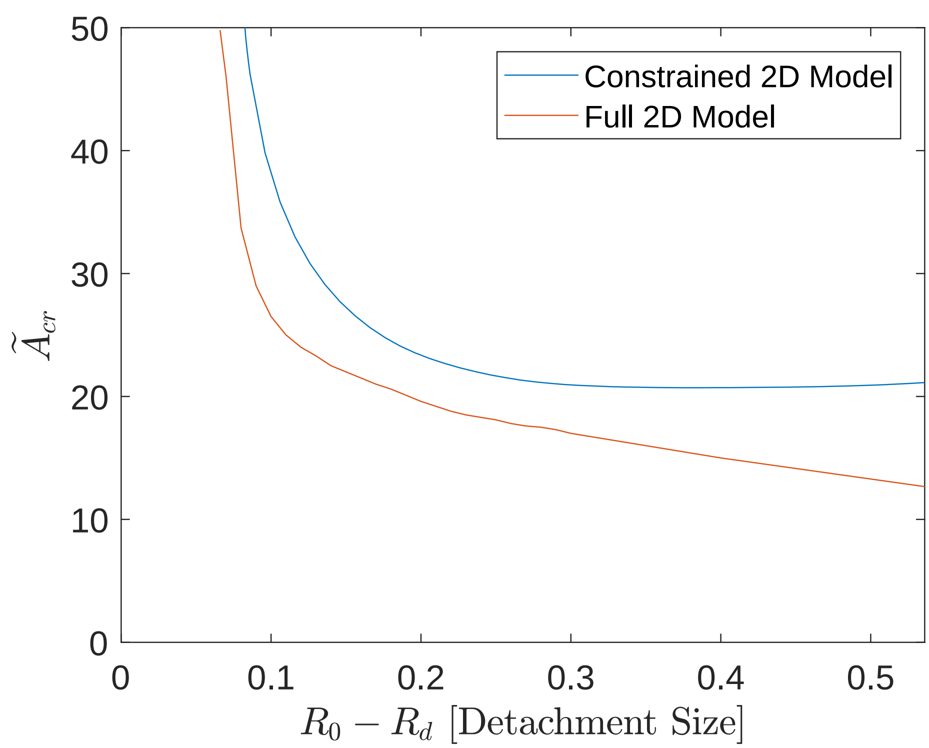

Figure 4.38: Comparison of the critical saccade amplitude per unit bond energy as a function of detachment size between the two models.

4.2.6 Parameter Study

Due to the large variance in the reported values of the shear modulus of the human vitreous, in addition to the aforementioned difficulties associated with measuring this property in vivo, a parameter study on the influence of the shear modulus on the behavior of the system is presented. The results are again compared to those derived for the constrained 2D model of Chapter 3.

For the full 2D model used here, the natural frequencies are determined as the square roots of the eigenvalues determined by Equation (4.22), the eigenvalue problem associated with the Rayleigh-Ritz Method. Though it is not as explicitly clear to see as the frequency equation for the full 2D model given by Equation (3.20), there is once again a dependence upon both detachment size and shear modulus. The influence of shear modulus for the full 2D model, as compared to the constrained 2D model, is demonstrated in Figure 4.39. Figures 4.39b, 4.39d, and 4.39f show that, for the full 2D model, the natural frequencies increase with shear modulus, as anticipated. The same qualitative shape is maintained for each of the three "branches“ that emerge , regardless of the value of the shear modulus. The dependence on shear modulus is very similar to that seen in Figures 4.39a, 4.39c, and 4.39e for the constrained 2D model. The magnitudes of the frequencies are very similar for each value of the shear modulus as well, with the full 2D model producing slightly lower frequencies than the constrained 2D model due to the system being less constrained.

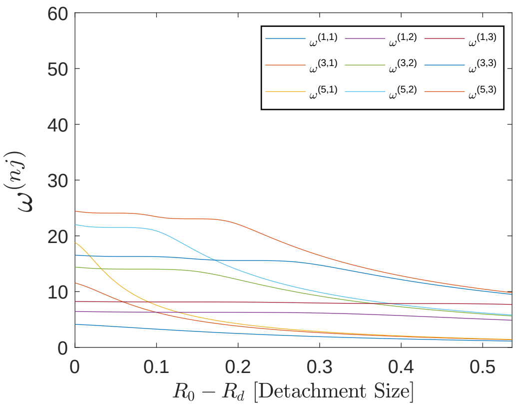

(a) **Constrained 2D model.** $G_1 = G_2 = 0.5$.

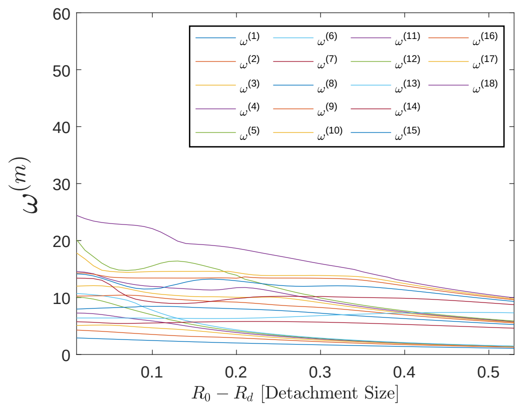

(b) **Full 2D model.** $G_1 = G_2 = 0.5$.

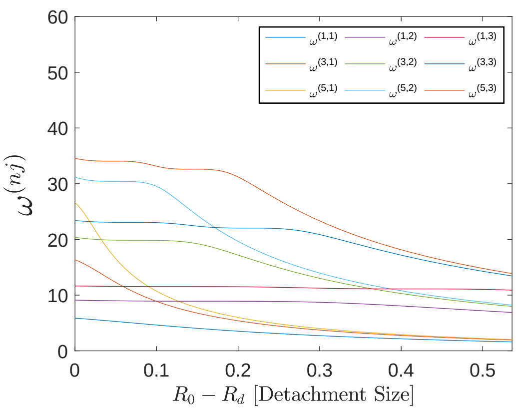

(c) **Constrained 2D model.** $G_1 = G_2 = 1.0$.

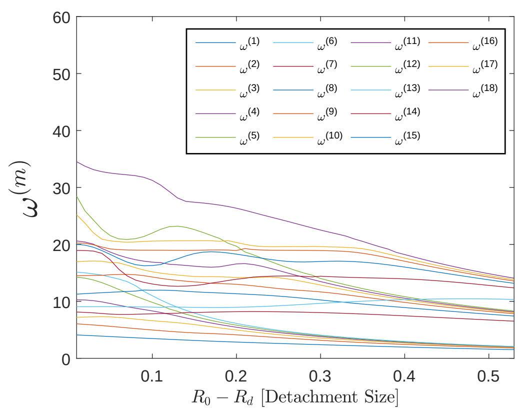

(d) **Full 2D model.** $G_1 = G_2 = 1.0$.

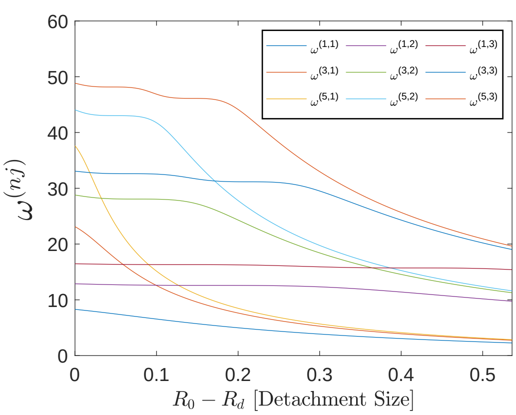

(e) **Constrained 2D model.** $G_1 = G_2 = 2.0$.

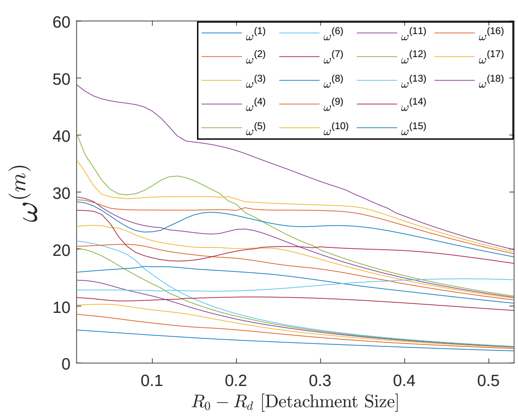

(f) **Full 2D model.** $G_1 = G_2 = 2.0$.

Figure 4.39: Comparison of natural frequencies for different values of shear modulus for the two models.

The effect the shear modulus has on the stress distribution throughout the vitreous is presented in Figures 4.40 – 4.42. These figures, once again, also compare the results to those of the constrained 2D model. It is seen that changing the value of the shear modulus only changes the magnitude of the normal and shear stresses, but not the distribution of these stresses throughout the vitreous. It is observed that a larger value of the shear modulus corresponds to larger magnitudes of stress. It has already been noted that the full 2D model results in significantly larger values of stress at the detachment points a and b. This parameter study shows that varying the shear modulus drastically changes the magnitude of stress at the detachment points, even more so than for the constrained 2D model.

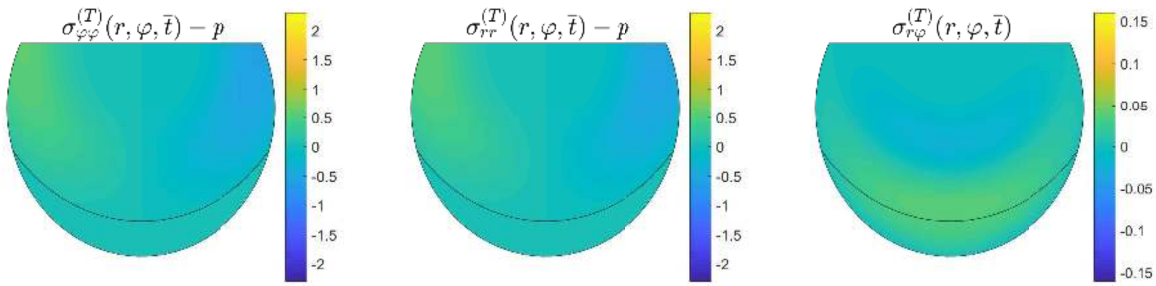

(a) Constrained 2D model

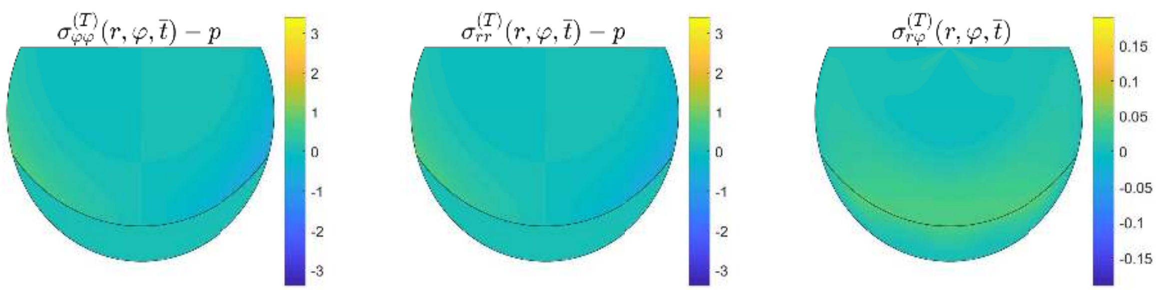

(b) Full 2D model

Figure 4.40: Comparison of maximum stress fields during a saccade of amplitude 20° with detachment size, $R_0 - R_d = 0.236$ where $G_1 = G_2 = 0.5$ for the two models.

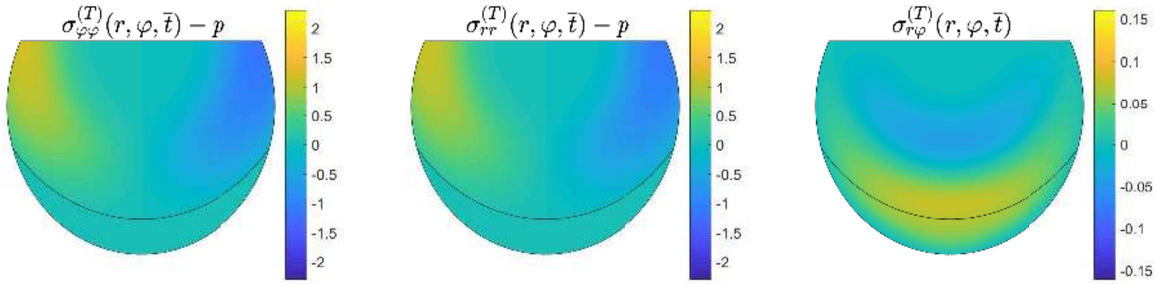

(a) Constrained 2D model

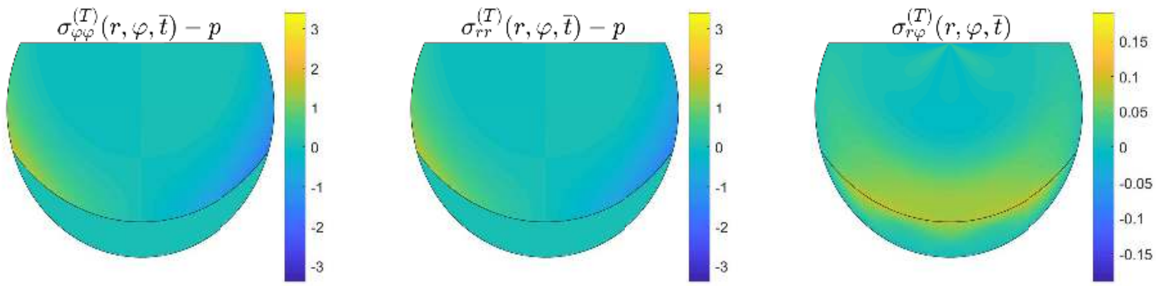

(b) Full 2D model

Figure 4.41: Comparison of maximum stress fields during a saccade of amplitude 20° with detachment size, $R_0 - R_d = 0.236$ where $G_1 = G_2 = 1.0$ for the two models.

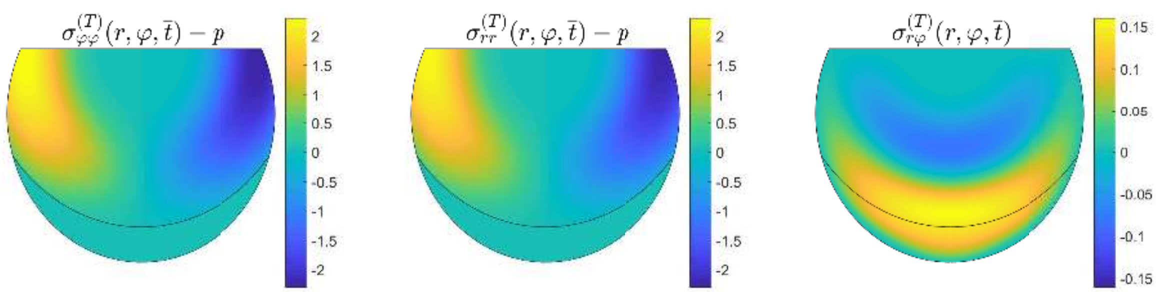

(a) Constrained 2D model

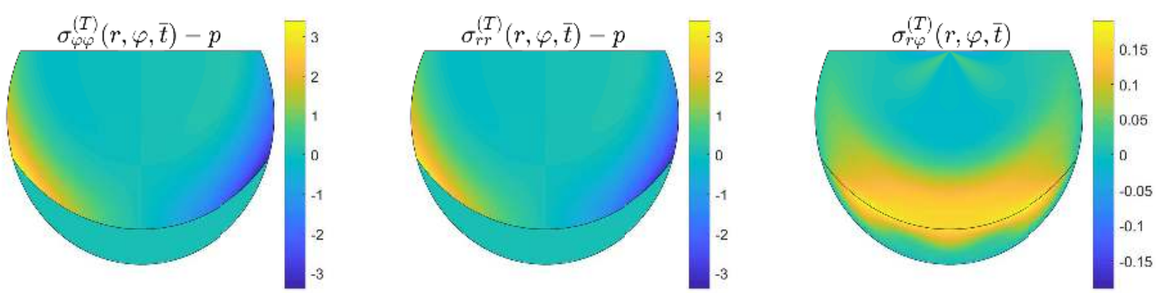

(b) Full 2D model

Figure 4.42: Comparison of maximum stress fields during a saccade of amplitude 20° with detachment size, $R_0 - R_d = 0.236$ where $G_1 = G_2 = 2.0$ for the two models.

The magnitude of stress at the detachment points plays a significant role in predicting the evolution of the detachment boundary during saccadic motion, as seen by the transversality condition given by Equation (4.36). Figure 4.43 compares the maximum energy release rate as a function of detachment size for both models for various values of the shear modulus. Figures 4.43b, 4.43d, and 4.43f show the significant effect that the shear modulus plays on the maximum energy release rate for the full 2D model. The maximum energy release rate increases as the shear modulus increases, but to a much larger degree than was predicted by the 2D constrained model. It can be noted that, unlike for the constrained 2D model, for the the full 2D model the energy release rate curves always increase monotonically. This result is important, and can be seen more clearly by the threshold curves presented in Figure 4.44. For the full 2D model, the detachment is catastrophic for all values of the shear modulus. Finally, it is seen that as the shear modulus increases, the critical saccade amplitude (per unit bond energy) for detachment progression is lowered.

The implications of the parameter study of the shear modulus are clear. As the shear modulus increases, the system response is qualitatively the same. However, stress at the detachment boundary is largely a function of the shear modulus. With an increase in the shear modulus, it is observed that stress increases, and thus the energy release rate increases, and therefore catastrophic vitreo-retinal detachment occurs at saccades of lower amplitudes.

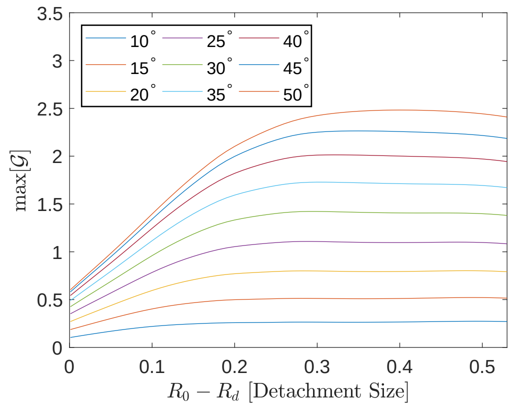

(a) **Constrained 2D model.** $G_1 = G_2 = 0.5$.

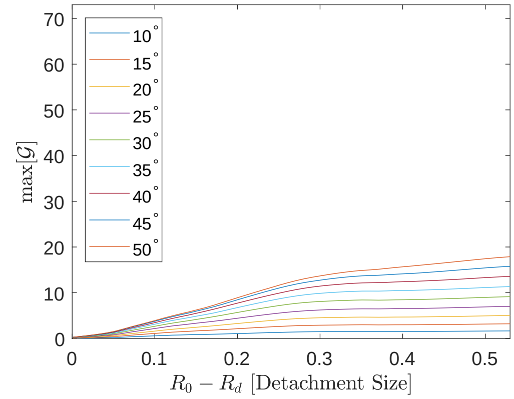

(b) **Full 2D model.** $G_1 = G_2 = 0.5$.

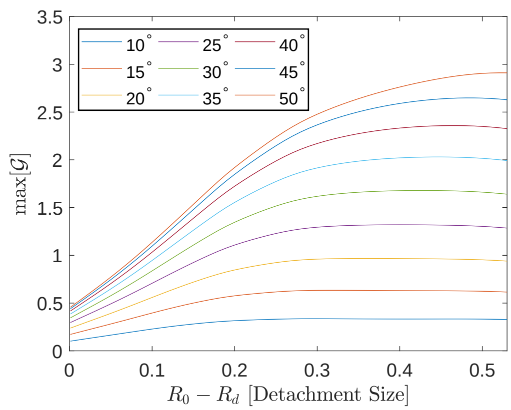

(c) **Constrained 2D model.** $G_1 = G_2 = 1.0$.

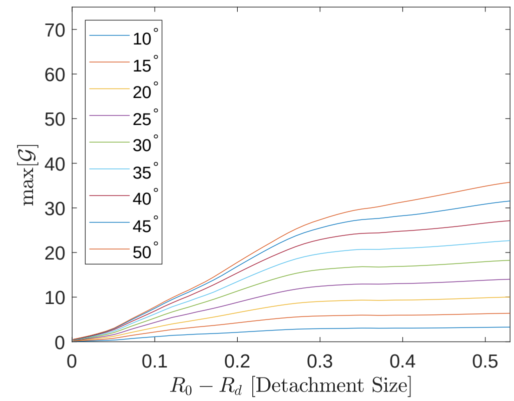

(d) **Full 2D model.** $G_1 = G_2 = 1.0$.

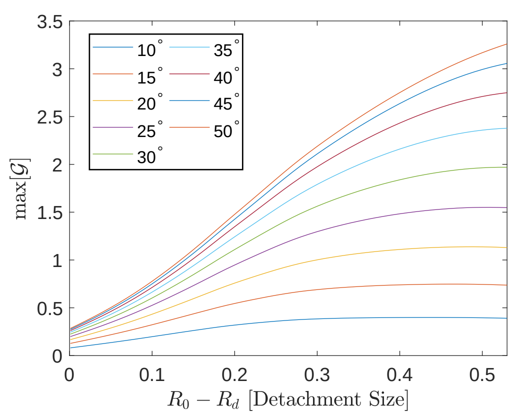

(e) **Constrained 2D model.** $G_1 = G_2 = 2.0$.

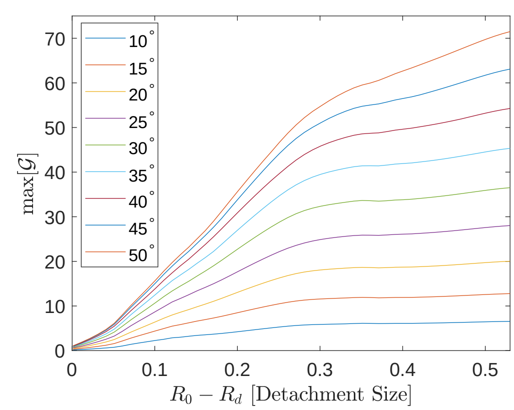

(f) **Full 2D model.** $G_1 = G_2 = 2.0$.

Figure 4.43: Comparison of energy release rate per unit depth as a function of detachment size for three different values of shear modulus for the two models.

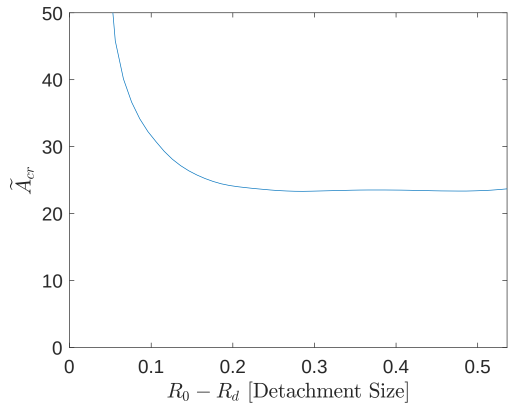

(a) **Constrained 2D model.** $G_1 = G_2 = 0.5$.

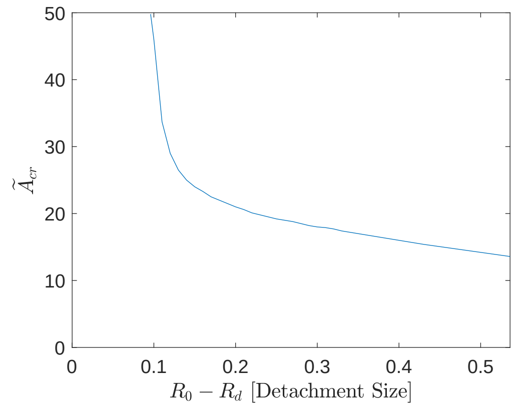

(b) **Full 2D model.** $G_1 = G_2 = 0.5$.

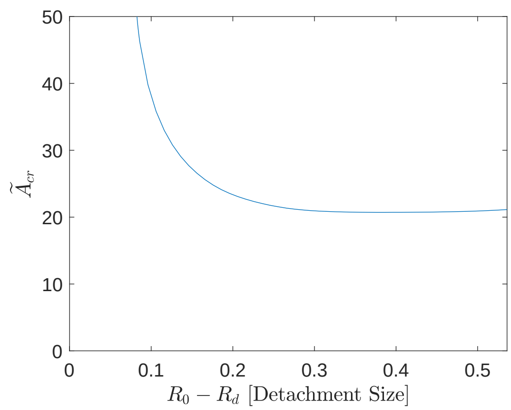

(c) **Constrained 2D model.** $G_1 = G_2 = 1.0$.

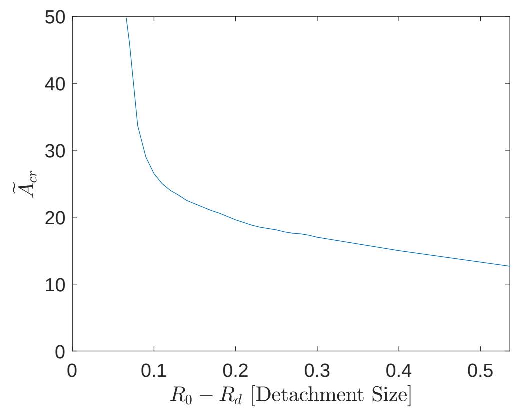

(d) **Full 2D model.** $G_1 = G_2 = 1.0$.

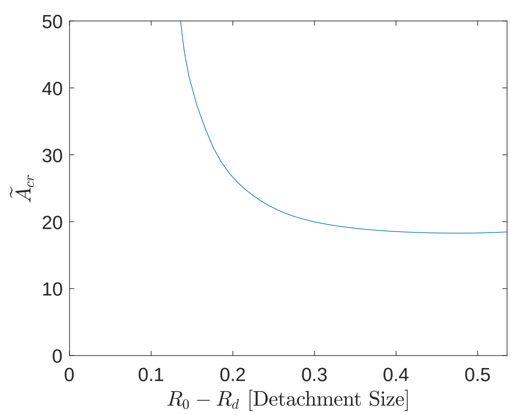

(e) **Constrained 2D model.** $G_1 = G_2 = 2.0$.

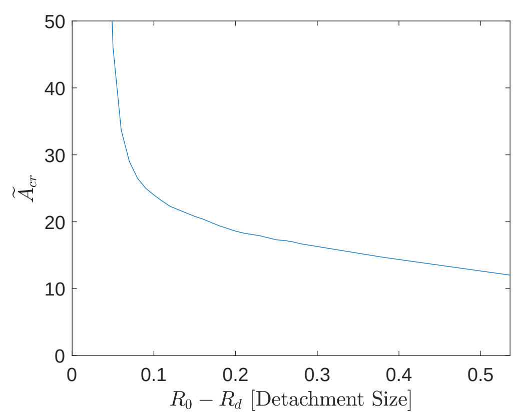

(f) **Full 2D model.** $G_1 = G_2 = 2.0$.

Figure 4.44: Comparison of critical saccade amplitude per unit bond energy as a function of detachment size for different values of shear modulus for the two models.

4.3 Conclusions

The analysis of the full 2D model is now complete. This model improves upon the constrained 2D model. It is demonstrated that consideration of radial motion of the vitreous is necessary to more accurately determine the pathology of the detaching vitreous when subjected to saccadic motion. Results show the stress distribution during a saccade to be different, with a larger concentration of stress at detachment points a and b. This is significant, as the stress at points a and b, and along surface C_4, factor largely into predicting the pathology of vitreo-retinal detachment. It was observed that the constrained 2D model underestimated the energy release rate during a saccade, and therefore predicted detachment at a higher critical saccade amplitude. The full 2D model predicts catastrophic detachment in all scenarios, whereas the constrained 2D model predicts a small range of stable detachment. Therefore, the full 2D model is more conservative, as it predicts detachment from a lower amplitude saccade.

Chapter 5

Concluding Remarks

Two 2D models were developed for the partially detached vitreous body when subjected to saccadic movements. The first model restricted the vitreous from moving in the radial direction, while this constraint was relaxed in the second model. Corresponding governing equations of motion, boundary and matching conditions, and a transversality condition were derived using a variational formulation. For the constrained 2D model, a closed form analytical solution was developed using modal analysis. For the full 2D model, a semi-analytical solution was developed by employing the Rayleigh-Ritz method in conjunction with modal analysis.

Numerical simulations were presented for both models and compared to one another. It was observed that the constrained 2D model was not the conservative model that was anticipated, but rather that this model underestimated the effects that saccadic motion had on the stress distribution throughout the vitreous, as well as the behavior of the detachment of the vitreo-retinal interface. Simulations from the full 2D model showed that while the radial motion of the vitreous is indeed an order of magnitude less than the circumferential motion, constraining the vitreous in this way largely affected the magnitude of the stress distribution throughout the vitreous, and severely underestimated the energy release rate during detachment. In addition, the full 2D model determined that detachment due to saccadic motion would always be catastrophic, whereby once initially detached, the interface would continue to detach until it reached a point of abnormal adhesion between the vitreous and retina. While this was observed for most detachment sizes in the constrained 2D model, for very large detachment sizes, it was observed that further detachment was stable, and would not grow continuously.

A parameter study was performed to determine the influence of the shear modulus on the results, as this material property is very difficult to measure, and changes largely with age and health factors. It was concluded that, for both models, the value of the shear modulus affects the quantitative results for displacement, stress, and detachment behavior. However, the studies showed that, qualitatively, all behavior was the same. The stress fields were of the same form, and the threshold paths concluded the same type of detachment behavior.

Prior to this work, only bio-chemical processes have been considered for understanding the progression of vitreous detachment. In the current study, the effects of saccadic eye movements on the progression of vitreous detachment in the human eye is analyzed from a mechanical perspective. By doing so, this work supports the hypothesis that saccadic movements can cause the spreading of PVD.

In determining a criterion for vitreous detachment progression, a model of the vitreous body during saccadic motion was developed. From this, the stress distribution inside the vitreous body and along the retinal walls was determined. The current study agrees qualitatively in large part with other experimental, computational, and analytical studies of the vitreous when subjected to saccadic motion. Furthermore, prior analytical studies of the vitreous subject to saccadic motion considered viscous fluids, and neglected the contribution due to the solid portion of the vitreous gel. This analytical study considers both viscous and elastic solid contributions, which has only been considered in computational studies. However, the use of modal analysis in the current solution procedure yields the natural modes of the vitreous body, and thus provides much greater insight into the fundamental behavior of the gel-like vitreous.

The use of modal analysis is also beneficial for future work. Different loading situations can be considered using the same model. The model can be amended to study the effects of micro-saccades or extremely large saccades that usually coincide with head movement. This model can also be amended to study the effects on PVD progression of impulsive or shock loading due to blunt trauma to the head. Furthermore, the time-dependent stress distribution along the retinal walls determined by this study can be used in a future study of the progression of retinal detachment when subjected to saccadic motion.

This work serves as a significant contribution towards the understanding of the fundamental behavior of the extremely complicated system that is the human eye. With greater knowledge and understanding of the complexities of the eye, we can work towards having ever greater preventative eye care, as well as improve surgical procedures and reduce eye related health and vision issues.

References

[1] Akiba J. (1993) Prevalence of posterior vitreous detachment in high myopia. *Ophthalmology*, **100(9)**, 1384-1388.

[2] Bahill A.T., Brockenbrough A., and Troost B.T. (1981) Variability and development of a normative data base for saccadic eye movements. *Investigative Ophthalmology & Visual Science*. **21**, 116-125.

[3] Balazs E.A.(1961) Molecular morphology of the vitreous body. In *Structure of the Eye*, Smelser G.K. (ed). Academic Press Inc., New York.

[4] Baloh R.W., Sills A.W., Kumley W.E., and Honrubia V. (1975) Quantitative measurement of saccadic amplitude, duration, and velocity. *Neurology*. **25**, 1065-1070.

[5] Becker W. (1989) Metrics. In *The neurobiology of saccadic eye movements*, Wurtz R.H., Goldberg M.E. (eds). Elsevier Science Publishers BV (Biomedical Division), Amsterdam.

[6] Benaroya H. and Nagurka M.L. (2010) *Mechanical Vibration: Analysis, Uncertainties, and Control - Third Edition*. CRC Press, Boca Raton, FL.

[7] Bill A. and Sperber G.O. (1990) Control of retinal and choroidal blood flow. *Eye*, **4**, 319-325.

[8] Bishop P.N., Crossman M.V., McLeod D., and Ayad S. (1994) Extraction and characterisation of the tissue forms of collagen types II and IX from bovine vitreous. *Biochemistry Journal*, **299**, 497505.

[9] Bishop P.N. (2000) Structural macromolecules and supramolecular organisation of the vitreous gel. *Progress in Retinal and Eye Research*, **19**, 323344.

[10] Boettner E.A. and Wolter J.R. (1962) Transmission of the ocular media. *Investigative Ophthalmology*, **1**, 776.

[11] Boghen D., Troost B.T., Daroff R.B., Dell'Osso L.F., and Birkett J.E. (1974) Velocity characteristics of of normal human saccades. *Investigative Ophthalmology*. **13**, 619-623.

[12] Bonfiglio A., Lagazzo A., Repetto R., and Stocchino A. (2015) An experimental model of vitreous motion induced by eye rotations. *Eye and Vision*, **2(10)**, doi:10.1186/s40662-015-0020-8.

[13] Bos K.J., Holmes D.F., Kadler K.E., McLeod D., Morris N.P., and Bishop P.N. (2001) Axial structure of the heterotypic collagen fibrils of vitreous humour and cartilage. *Journal of Molecular Biology*, **306**, 10111022.

[14] Bottega W.J. (1983) A growth law for propagation of arbitrary shaped delaminations in layered plates. *International Journal of Solids and Structures*, **11**, 1009-1017.

[15] Bottega W.J. (2015) *Engineering Vibrations - Second Edition.* CRC Press, Boca Raton, FL.

[16] Bottega W.J., Bishay P.L., Prenner J.L. and Fine H.F. (2013) On the mechanics of a detaching retina. *Mathematical Medicine and Biology*, **30**, 287-310.

[17] David T., Smye S., James T., and Dabbs T. (1997) Time-dependent stress and displacement of the eye wall tissue of the human eye. *Medical Engineering & Physics*, **19(2)**, 131-139.

[18] David T., Smye S., Dabbs T., and James T. (1998) A model for the fluid motion of vitreous humour of the human eye during saccadic movement. *Physics in Medicine and Biology*, **43**, 1385-1399.

[19] Eisner G. (1973) *Biomicroscopy of the peripheral fundus.* Springer-Verlag, New York.

[20] Foos R.Y. and Wheeler N.C. (1982) Vitreoretinal juncture: synchysis senilis and posterior vitreous detachment. *Ophthalmology*, **89(12)**, 1502-1512.

[21] Foulds W.S. (1987) Is your vitreous really necessary? The role of the vitreous in the eye with particular reference to retinal attachment, detachment and the mod of action of vitreous substitutes. *Eye*, **1**, 641-664.

[22] Ge P., Bottega W.J., Prenner J.L., and Fine H.F. (2016) On the influence of an equatorial cerclage on closure of posterior retinal detachment. *Mathematical Medicine and Biology*, **33(4)**, 417-433.

[23] Ge P., Bottega W.J., Prenner J.L., and Fine H.F. (2017) On the behavior of an eye encircled by a scleral buckle. *Journal of Mathematical Biology*, **74(1-2)**, 313-332.

[24] Gloor B.P. (1981) The vitreous. In Moses R.A., Hart W.M. eds. *Adler's physiology of the eye: clinical applications.* C.V. Mosby, St. Louis.

[25] Griffith A.A. (1921) The phenomena of rupture and flow in solids. *Philosophical Transactions of the Royal Society A*, **221**, 163-198.

[26] Halfter W., Winzen U., Bishop P.N., and Eller A. (2006) Regulation of eye size by the retinal basement membrane and vitreous body. *Investigative Ophthalmology and Visual Science*, **47** 35863594.

[27] Hogan M.J., Alvarado J.A., and Weddel J.E. (1971) *Histology of the human eye: An atlas and textbook.* W.B. Saunders, Philadelphia PA.

[28] Holekamp N.M., Shui Y.B., and Beebe D.C. (2005) Vitrectomy surgery increases oxygen exposure to the lens: a possible mechanism for nuclear cataract formation. *American Journal of Ophthalmology*, **139** 302310.

[29] Ilanko S., Monterrubio L., and Mochida Y. (2014) *The Rayleigh-Ritz Method for Structural Analysis.* Wiley, Hoboken, NJ.

[30] Inchingolo P. and Spanio M. (1985) On the identification and analysis of saccadic eye movements - a quantitative study of the processing procedures. *IEEE Transactions of Biomedical Engineering.* **BME-32**, 683-695.

[31] Kakehashi A., Kado M., Akiba J. and Hirokwa H. (1997) Variations of posterior vitreous detachment. *British Journal of Ophthalmology*, **81**, 527-532.

[32] Kita M. and Marmor M. (1992) Retinal adhesive force in living rabbit, cat, and monkey eyes. normative data and enhancement by mannitol and acetazolamide. *Investigative Ophthalmology and Visual Science*, **33(6)**, 1879-1882.

[33] Lakawicz J.M., Bottega W.J., Prenner J.L. and Fine H.F. (2015) An analysis of the mechanical behaviour of a detaching retina. *Mathematical Medicine and Biology*, **32(2)**, 137-161.

[34] Lee B., Litt M., and Buchsbaum G. (1993) Rheology of the vitreous body. Part I: Viscoelasticity of human vitreous. *Biorheology*, **29(5-6)**, 521-533.

[35] Lee B., Litt M., and Buchsbaum G. (1994) Rheology of the vitreous body: Part 2. Viscoelasticity of bovine and porcine vitreous. *Biorheology*, **34(4)**, 327-338.

[36] Le Goff M.M. and Bishop P.N. (2008) Adult vitreous structure and postnatal changes *Eye*, **22**, 1214-1222.

[37] Meskauskas J., Repetto R., and Siggers J.H. (2012) Shape change of the vitreous chamber influences retinal detachment and reattachment processes: is mechanical stress during eye rotations a factor? *Investigative Ophthalmology & Visual Science*, **53(10)**, 6271-6281.

[38] Modarreszadeh A. and Abouali O. (2014) Numerical simulation for unsteady motions of the human vitreous humor as a viscoelastic substance in linear and non-linear regimes. *Journal of Non-Newtonian Fluid Mechanics*, **204**, 22-31.

[39] Nickerson C.S., Park J., Kornfield J.A. and Karageozian H. (2008) Rheological properties of the vitreous and the role of hyaluronic acid. *Journal of Biomechanics*, **41**, 1840-1846.

[40] Repetto R., Ghigo I., Seminara G., and Ciurlo C. (2004) A simple hydro-elastic model of the dynamics of a vitreous membrane. *Journal of Fluid Mechanics*, **503**, 1-14.

[41] Repetto R., Stocchino A., and Cafferata C. (2005) Experimental investigation of vitreous humour motion within a human eye model. *Physics in Medicine and Biology*, **50**, 4729-4743.

[42] Repetto R., Tatone A., Testa A., and Colangeli E. (2011) Traction on the retina induced by saccadic eye movements in the presence of posterior vitreous detachment. *Biomechanics and Modeling in Mechanobiology*, **10(2)**, 191-202.

[43] Robinson D.A. (1964) The mechanics of human saccadic eye movement. *Journal of Physiology*, **174**, 245-264.

[44] Sebag J. (1987) Ageing of the vitreous. *Eye*, **1(2)**, 254-262.

[45] Sebag J. (1989) *The Vitreous - Structure, Function, and Pathobiology*. Springer-Verlag Inc., New York.

[46] Snead M.P., Snead D.R.J., Richards A.J., Harrison J.B., Poulson A.V., Morris A.H.C., Sheard R.M., and Scott J.D. (2002) Clinical, histological and ultrastructural studies of the posterior hyaloid membrane. *Eye*, **16**, 447-453.

[47] Snowden J.M. and Swann D.A. (1980) Vitreous structure. V. The morphology and thermal stability of vitreous collagen fibers and comparison to articular cartilage (type II) collagen. *Investigative Ophthalmology & Visual Science*, **19(6)**, 610-618.

[48] Swindle K.E., Hamilton P.D., and Ravi N. (2008) In situ formation of hydrogels as vitreous substitutes: Viscoelastic comparison to porcine vitreous. *Journal of Biomedical Materials Research Part A*, **87A**, 656-665.

[49] Wilkerson C.P. and Rice T.A. (1997) *Michels Retinal Detachment, Second Edition.* C.V. Mosby, St. Louis.

[50] Zimberlin J.A., McManus J.J., and Crosby A.J. (2010) Cavitation rheology of the vitreous: mechanical properties of biological tissue. *Soft Matter*, **6**, 3632-3635.

[51] Zimmerman R.L. (1980) In vivo measurements of the viscoelasticity of the human vitreous humor. *Biophysics Journal*, **29(3)**, 539-544.

Appendix A

Constants as Determined by the Rayleigh-Ritz Method

The following tables display the constants determined by application of the Rayleigh-Ritz method which determine the relative contribution of each trial function towards each mode of the full 2D solution. The constants are determined as the eigenvectors of Equation (4.22). Tables are presented for three separate detachment sizes: $R_0 - R_d = 0.036$, $R_0 - R_d = 0.236$, and $R_0 - R_d = 0.436$.

	Mode Number																	
Constant	1	2	3	4	5	6	7	8	9	10	11	12	13	14	15	16	17	18
$C_v^{(m;1,1)}$	1	-2.66E-14	8.57E-02	6.35E-15	-6.70E-02	-4.37E-13	-3.31E-01	1.44E-13	1.79E-02	-1.39E-13	1.41E-03	-6.06E-15	2.23E-01	-4.19E-13	7.58E-02	-6.33E-14	-8.94E-03	-1.11E-13
$C_v^{(m;2,1)}$	-4.88E-14	-1	2.19E-14	2.10E-01	1.02E-12	9.77E-02	-7.50E-14	-2.02E-01	7.66E-12	8.89E-03	3.43E-13	5.30E-02	9.91E-13	3.80E-01	8.65E-14	1.68E-02	-2.76E-13	-8.38E-02
$C_v^{(m;3,1)}$	7.99E-02	-2.47E-14	1	-2.32E-13	3.90E-01	-1.60E-12	4.88E-01	-1.97E-13	-1.38E-02	3.80E-13	1.69E-03	-9.95E-14	2.39E-03	-9.57E-13	5.77E-01	7.92E-13	1.89E-02	-2.01E-13
$C_v^{(m;4,1)}$	-4.25E-15	-1.42E-01	-7.96E-14	-1	-4.72E-13	-3.61E-01	-6.65E-14	-9.88E-02	-3.86E-13	1.44E-01	-2.32E-13	-4.03E-02	-2.06E-15	-2.11E-03	6.68E-13	5.10E-01	-3.10E-12	-6.67E-02
$C_v^{(m;5,1)}$	-2.54E-02	-2.71E-14	2.63E-01	-2.10E-13	-1	7.79E-12	5.43E-02	1.77E-13	-1.54E-03	8.29E-12	1.03E-01	6.47E-14	4.90E-03	1.72E-12	-3.41E-01	1.10E-13	5.33E-01	-1.04E-13
$C_v^{(m;6,1)}$	5.32E-15	5.39E-02	-2.00E-13	-2.53E-01	1.45E-12	6.65E-01	-4.72E-14	-7.27E-02	2.52E-12	1.16E-01	9.59E-12	-1.58E-01	-4.83E-14	1.06E-01	-2.25E-12	6.90E-01	-9.09E-12	6.58E-02
$C_v^{(m;1,2)}$	-2.48E-01	2.56E-14	6.45E-01	6.02E-14	1.08E-01	-1.99E-13	-1	-1.33E-13	4.43E-02	3.56E-13	-1.31E-02	7.57E-14	-1.67E-01	-5.00E-13	-1.05E-02	1.08E-13	3.53E-02	3.21E-13
$C_v^{(m;2,2)}$	6.37E-15	1.96E-01	-6.97E-14	1.30E-01	-1.12E-12	4.51E-02	-9.22E-15	-1	-5.30E-12	1.01E-02	-7.01E-13	-8.18E-02	1.34E-13	-2.62E-01	-4.61E-13	-7.75E-02	3.41E-13	7.30E-02
$C_v^{(m;3,2)}$	1.35E-02	-1.78E-14	-9.71E-03	8.73E-14	5.64E-02	2.71E-12	-1.85E-02	-3.36E-14	-1	-3.54E-13	-2.44E-02	-1.63E-14	-4.97E-02	1.38E-11	-5.09E-01	1.29E-12	-3.46E-02	-1.82E-13
$C_v^{(m;4,2)}$	-1.57E-15	-3.68E-02	-1.09E-14	-1.92E-01	-5.33E-14	1.86E-02	-3.32E-14	-7.43E-02	-5.89E-13	1	1.27E-13	-5.11E-02	5.37E-15	-2.72E-02	-8.90E-14	-3.62E-01	-1.67E-11	-2.55E-01
$C_v^{(m;5,2)}$	-1.96E-02	-1.10E-14	1.10E-01	1.91E-13	-3.49E-01	-4.80E-12	2.36E-02	1.60E-13	-1.02E-01	-8.62E-12	1	-3.27E-12	2.14E-02	1.72E-12	2.69E-01	-2.89E-12	-4.91E-01	1.18E-14
$C_v^{(m;6,2)}$	1.75E-15	4.02E-02	-2.33E-14	-1.47E-01	1.80E-13	2.01E-01	-6.08E-15	-2.11E-02	1.24E-12	-1.12E-01	1.98E-12	1	-2.11E-14	6.50E-02	1.60E-12	-1.39E-01	2.05E-12	3.63E-01
$C_v^{(m;1,3)}$	-2.18E-01	3.31E-13	7.35E-02	-3.21E-13	8.83E-02	1.64E-12	-9.23E-02	7.32E-13	-8.70E-02	-1.73E-13	-2.99E-02	4.01E-13	1	-9.26E-13	-1.47E-01	1.66E-13	-6.03E-03	1.50E-13
$C_v^{(m;2,3)}$	-4.53E-16	3.23E-01	6.42E-14	2.58E-02	1.75E-12	-2.25E-01	4.31E-14	-2.12E-01	1.97E-11	3.49E-02	-7.46E-13	-1.58E-01	5.70E-13	1	1.65E-12	-6.80E-02	-9.98E-14	1.77E-01
$C_v^{(m;3,3)}$	-3.24E-02	-1.41E-14	-3.88E-01	1.41E-13	2.98E-02	-2.02E-12	-2.14E-01	8.93E-14	-5.04E-01	-2.04E-12	1.60E-02	-1.63E-13	-2.51E-02	6.20E-12	1	-1.02E-12	-1.24E-01	3.46E-13
$C_v^{(m;4,3)}$	1.85E-16	6.87E-02	6.59E-14	3.85E-01	-1.81E-13	-1.25E-01	8.32E-15	-2.08E-02	-2.17E-13	1.52E-01	2.40E-12	2.86E-01	1.26E-14	-1.33E-02	-3.55E-14	1	-4.85E-12	1.79E-02
$C_v^{(m;5,3)}$	3.78E-03	1.03E-14	-1.17E-01	5.13E-14	2.42E-01	-3.38E-12	-2.32E-02	-1.08E-14	-1.09E-01	1.55E-11	6.00E-01	-1.50E-12	1.84E-02	9.77E-13	2.79E-01	2.91E-12	1	1.35E-13
$C_v^{(m;6,3)}$	-2.34E-16	-1.51E-02	1.52E-14	8.50E-02	-3.73E-14	-1.32E-02	1.87E-15	4.66E-02	-1.23E-13	2.10E-02	-1.77E-12	-3.19E-01	-5.41E-15	-5.55E-03	4.28E-13	1.04E-01	-2.45E-15	9.76E-01
$C_u^{(m;1,1)}$	-6.31E-16	-8.55E-02	-1.09E-14	7.16E-02	-2.83E-14	1	-1.05E-14	-1.53E-01	-6.79E-13	7.40E-02	-4.11E-13	-1.40E-01	1.14E-13	-3.77E-02	1.40E-11	-1.04E-02	-1.14E-12	-6.13E-02
$C_u^{(m;2,1)}$	-1.57E-01	5.51E-14	-1.34E-01	-2.97E-14	-1.90E-01	-4.14E-12	-1.46E-02	2.05E-13	4.13E-01	6.90E-13	-9.70E-02	3.79E-13	1.58E-01	-5.93E-12	5.93E-01	1.28E-12	2.53E-02	1.03E-12
$C_u^{(m;3,1)}$	-8.47E-15	-1.91E-01	-1.54E-14	-1.25E-01	-5.03E-13	-6.24E-01	-3.35E-14	-3.13E-01	-2.54E-12	-4.76E-01	6.89E-13	1.93E-01	2.04E-13	-1.25E-01	-4.80E-12	5.28E-02	7.64E-12	-2.49E-01
$C_u^{(m;4,1)}$	4.70E-02	-2.76E-15	-2.58E-01	-1.70E-14	2.67E-01	3.38E-12	-1.14E-01	-1.05E-13	6.77E-01	-2.13E-12	4.56E-01	-1.45E-12	-4.98E-02	-9.41E-12	-3.34E-01	-1.18E-12	-1.03E-01	4.64E-13
$C_u^{(m;5,1)}$	2.77E-15	4.80E-02	-4.58E-14	-3.94E-01	3.15E-13	5.50E-01	-2.56E-14	9.97E-03	1.66E-12	-6.17E-01	-2.76E-12	-5.07E-01	-8.43E-14	8.96E-02	4.70E-12	-1.13E-01	1.19E-11	-2.56E-01
$C_u^{(m;6,1)}$	-1.44E-02	1.61E-14	-1.34E-02	-8.28E-14	5.10E-01	5.76E-12	2.08E-02	-1.23E-13	-8.16E-02	-3.58E-12	5.94E-01	-1.84E-12	1.25E-02	2.15E-13	-5.75E-01	-6.28E-12	-1.70E-01	6.08E-13
$C_u^{(m;1,2)}$	2.83E-15	6.61E-02	2.79E-15	-1.98E-02	8.69E-14	-6.57E-04	4.18E-15	-3.53E-02	1.51E-12	4.57E-02	-9.61E-13	-4.08E-01	1.54E-14	7.73E-02	7.96E-13	-4.21E-02	-5.39E-13	-1.71E-01
$C_u^{(m;2,2)}$	8.61E-02	-4.19E-14	2.70E-02	5.23E-15	3.22E-02	-2.20E-13	1.41E-01	-1.09E-13	4.34E-02	1.25E-12	-9.57E-02	1.03E-12	-9.67E-02	-3.80E-13	-5.93E-02	6.06E-13	7.86E-02	2.91E-12
$C_u^{(m;3,2)}$	3.84E-15	1.48E-01	1.29E-14	1.08E-01	2.36E-13	-1.80E-02	1.97E-14	-4.57E-02	2.95E-12	-1.98E-01	1.24E-12	4.28E-01	2.25E-14	1.48E-01	2.50E-13	1.33E-01	2.85E-12	-1
$C_u^{(m;4,2)}$	-2.38E-02	1.12E-14	2.14E-01	-4.45E-14	-1.11E-01	6.76E-13	4.69E-02	3.22E-14	1.78E-02	-2.94E-12	3.66E-01	-1.96E-12	4.26E-02	-1.08E-13	-1.76E-01	-5.29E-13	-1.77E-01	1.45E-12
$C_u^{(m;5,2)}$	-1.44E-15	-3.72E-02	3.39E-14	2.23E-01	-2.07E-13	-8.33E-02	1.09E-14	4.73E-02	-1.50E-12	-1.76E-01	-2.77E-12	-7.45E-01	1.73E-15	-7.78E-02	-4.61E-13	1.56E-01	3.51E-12	-4.80E-01
$C_u^{(m;6,2)}$	9.44E-03	-1.51E-14	-1.86E-02	3.35E-14	-2.23E-01	-2.22E-13	4.08E-03	4.78E-14	-1.52E-02	-4.08E-12	3.35E-01	-1.99E-12	-2.19E-02	5.96E-13	8.03E-02	-9.63E-13	-2.47E-01	1.63E-12
$C_u^{(m;1,3)}$	-3.62E-16	-3.81E-02	3.29E-15	8.23E-03	-4.36E-14	1.03E-02	-3.56E-15	4.43E-02	-7.78E-13	-2.43E-03	2.43E-13	2.00E-02	-1.99E-14	-4.11E-02	-2.05E-13	2.65E-02	-1.79E-13	-4.94E-02
$C_u^{(m;2,3)}$	-1.95E-02	-7.89E-15	-3.16E-02	3.30E-14	-2.06E-02	7.32E-16	-8.12E-02	-8.32E-15	-6.94E-02	-7.39E-13	-6.62E-03	5.01E-14	-3.71E-02	1.01E-12	6.89E-02	-2.36E-13	-4.48E-02	1.73E-13
$C_u^{(m;3,3)}$	-1.92E-15	-8.67E-02	-9.01E-15	-7.88E-02	-9.37E-14	2.23E-02	-8.67E-15	8.23E-02	-1.47E-12	1.48E-03	-6.00E-13	-5.41E-02	-3.77E-14	-7.46E-02	-1.79E-14	-1.04E-01	2.85E-13	-6.96E-02
$C_u^{(m;4,3)}$	1.71E-04	3.85E-15	-1.36E-01	3.58E-14	6.63E-02	-7.36E-13	-3.73E-02	1.22E-14	-1.25E-01	1.89E-12	2.12E-02	-6.30E-14	8.92E-03	1.50E-12	1.56E-01	3.74E-13	1.18E-01	2.18E-13
$C_u^{(m;5,3)}$	8.80E-16	1.80E-02	-2.29E-14	-1.30E-01	1.00E-13	2.42E-02	-4.96E-15	-4.41E-02	7.54E-13	1.67E-02	6.01E-13	1.06E-01	1.03E-14	3.92E-02	-5.59E-14	-1.42E-01	-3.63E-13	-1.33E-01
$C_u^{(m;6,3)}$	1.91E-03	2.96E-15	1.31E-02	1.27E-15	9.94E-02	-8.17E-13	6.79E-04	-2.80E-14	3.49E-02	3.24E-12	-3.56E-03	1.11E-13	-4.88E-03	-6.02E-13	2.33E-02	1.01E-12	2.00E-01	-5.65E-14
$C_u^{(m;1,4)}$	7.28E-16	1.00E-02	-3.99E-15	-7.16E-03	-8.92E-14	6.34E-03	-6.20E-16	-2.95E-02	-6.29E-13	-1.03E-02	-1.19E-13	-9.21E-03	-1.52E-14	-3.17E-02	2.00E-14	-1.51E-02	2.31E-13	1.64E-02
$C_u^{(m;2,4)}$	-5.25E-03	2.18E-14	3.57E-02	-3.32E-14	2.55E-02	-2.11E-13	2.79E-02	4.00E-14	6.85E-02	5.52E-13	2.74E-02	-2.74E-14	7.05E-02	-1.12E-12	3.39E-03	1.01E-13	3.64E-02	-3.39E-14
$C_u^{(m;3,4)}$	1.68E-15	3.41E-02	-1.86E-16	6.68E-02	-1.32E-13	1.75E-02	1.09E-15	-5.87E-02	-1.12E-12	6.48E-02	4.55E-13	4.73E-02	-2.63E-14	-5.75E-02	-1.69E-13	7.85E-02	-1.40E-12	-4.81E-02
$C_u^{(m;4,4)}$	6.06E-03	-9.16E-15	9.02E-02	-3.65E-14	-6.52E-02	7.98E-13	3.65E-02	-2.53E-14	1.30E-01	-1.77E-12	-1.36E-01	4.18E-13	-2.38E-02	-1.59E-12	-6.55E-02	-4.02E-13	-1.16E-01	-7.33E-14
$C_u^{(m;5,4)}$	-7.36E-16	3.90E-05	2.68E-14	1.16E-01	-2.17E-14	-3.85E-02	4.99E-15	2.99E-02	2.41E-13	8.71E-02	-4.06E-13	4.35E-03	1.47E-14	1.21E-02	1.47E-13	8.91E-02	-1.37E-12	2.26E-01
$C_u^{(m;6,4)}$	-5.06E-03	2.37E-15	6.52E-03	-2.01E-14	-9.09E-02	1.24E-12	-5.32E-03	2.34E-14	-2.07E-02	-2.42E-12	-1.73E-01	6.08E-13	1.11E-02	4.32E-13	-7.60E-02	-4.18E-13	-1.59E-01	-2.67E-13

Table A.1: Trial function constants for small detachment size: $R_0 - R_d = 0.036$.

Constant	Mode Number																	
	1	2	3	4	5	6	7	8	9	10	11	12	13	14	15	16	17	18
$C_v^{(m;1,1)}$	-1	6.40E-14	-5.17E-02	9.69E-14	2.06E-02	1.13E-13	4.60E-02	-2.71E-15	1.26E-02	-3.29E-14	1.17E-02	9.00E-15	-1.21E-01	-7.55E-14	3.54E-03	9.18E-16	3.75E-03	1.43E-15
$C_v^{(m;2,1)}$	1.44E-14	-1	-2.22E-13	7.13E-02	1.57E-13	3.60E-02	-9.83E-15	-1.10E-01	-6.81E-14	-8.23E-03	-1.21E-13	-9.25E-03	-2.41E-14	1.96E-02	-1.04E-14	-5.15E-03	4.70E-14	-7.10E-03
$C_v^{(m;3,1)}$	-4.77E-02	-1.08E-13	1	2.04E-13	-6.17E-02	2.41E-12	1.07E-02	-1.00E-13	1.22E-01	-2.04E-14	-1.73E-03	3.94E-13	-3.49E-02	3.56E-16	-3.36E-03	-6.30E-15	-4.18E-03	-1.52E-14
$C_v^{(m;4,1)}$	-6.88E-14	-7.19E-02	7.43E-14	-1	-5.49E-12	-1.07E-01	-5.83E-15	-2.68E-02	-8.05E-14	-7.30E-02	-9.36E-14	4.19E-03	-6.16E-14	2.21E-03	1.72E-15	-1.79E-02	6.94E-16	2.61E-03
$C_v^{(m;5,1)}$	1.57E-02	-1.29E-13	6.20E-02	-5.07E-12	1	9.72E-13	2.53E-03	-7.43E-14	2.12E-02	5.81E-13	-2.53E-02	-8.65E-14	1.69E-02	8.49E-14	3.19E-03	5.00E-13	-1.53E-02	-4.71E-12
$C_v^{(m;6,1)}$	5.29E-14	2.78E-02	-1.73E-12	-1.09E-01	-1.35E-12	1	-1.65E-14	4.64E-03	7.40E-14	-1.74E-02	3.03E-13	3.04E-03	-4.15E-14	-1.03E-02	5.96E-15	-7.59E-03	-1.13E-13	4.28E-03
$C_v^{(m;1,2)}$	-2.94E-02	2.53E-15	2.83E-03	-1.07E-14	3.73E-03	7.97E-15	-1	-4.73E-14	5.67E-02	-9.70E-14	2.81E-02	-4.02E-14	-6.67E-02	9.91E-14	2.93E-04	-3.53E-14	-5.24E-03	1.17E-13
$C_v^{(m;2,2)}$	-1.22E-15	-7.90E-02	5.13E-15	-8.01E-03	-4.68E-14	-5.54E-03	-3.26E-14	1	5.52E-13	-1.42E-01	-1.69E-12	-9.10E-02	3.36E-14	-3.02E-01	1.82E-13	-1.88E-02	3.99E-14	-2.59E-02
$C_v^{(m;3,2)}$	-1.47E-02	-6.15E-15	5.75E-02	-2.23E-14	4.07E-03	1.58E-13	-2.02E-02	3.23E-13	-1	5.64E-13	-2.06E-01	1.34E-11	6.50E-02	9.06E-14	-1.19E-01	2.28E-14	-2.37E-02	3.72E-14
$C_v^{(m;4,2)}$	-2.38E-15	-1.34E-02	-1.43E-14	-3.22E-02	-2.04E-13	4.69E-03	-1.40E-14	1.01E-01	1.97E-13	1	5.45E-12	3.12E-01	-7.31E-15	3.62E-02	5.85E-15	-2.67E-02	-3.14E-14	1.14E-02
$C_v^{(m;5,2)}$	5.66E-03	-3.39E-15	8.15E-03	-7.48E-14	1.55E-02	3.00E-15	4.87E-03	7.63E-14	-1.33E-01	-2.14E-12	1	-1.11E-11	-1.94E-02	-3.21E-13	-3.78E-03	7.58E-14	-3.82E-02	5.50E-14
$C_v^{(m;6,2)}$	-1.51E-15	7.15E-03	-8.14E-15	-9.07E-03	-8.60E-14	3.13E-03	4.54E-14	-3.84E-02	3.78E-13	2.46E-01	-1.34E-11	-1	2.44E-14	2.20E-02	-2.00E-14	2.30E-02	-2.01E-13	1.18E-02
$C_v^{(m;1,3)}$	1.06E-01	-7.09E-15	-1.76E-02	-7.62E-14	1.48E-02	-6.23E-14	3.90E-02	1.19E-13	-1.29E-01	1.31E-13	-5.34E-02	1.68E-13	-1	1.30E-13	-2.97E-02	-2.03E-14	-3.07E-02	-3.17E-14
$C_v^{(m;2,3)}$	-2.24E-15	1.22E-02	-7.74E-15	2.07E-03	6.05E-15	6.65E-03	2.60E-14	1.76E-01	1.08E-13	-1.12E-01	-2.07E-13	-2.84E-02	4.88E-14	1	6.45E-14	3.38E-02	3.76E-14	3.28E-02
$C_v^{(m;3,3)}$	-1.22E-02	-3.70E-15	3.84E-02	-1.30E-14	2.20E-03	1.04E-13	-2.12E-02	1.60E-13	-4.70E-01	1.48E-13	2.95E-02	-1.07E-11	4.55E-02	3.88E-15	-1	-2.45E-13	-6.17E-02	-2.18E-13
$C_v^{(m;4,3)}$	-1.88E-15	-1.32E-02	-1.32E-14	-3.08E-02	-1.96E-13	4.45E-03	-5.20E-15	6.91E-02	1.24E-13	3.63E-01	7.00E-13	-4.65E-02	-3.45E-15	1.32E-02	-3.32E-13	1	-4.28E-13	1.48E-01
$C_v^{(m;5,3)}$	4.86E-03	-1.70E-15	6.74E-03	-7.06E-14	1.36E-02	2.93E-14	1.56E-03	1.73E-14	-6.14E-02	-1.78E-13	1.51E-01	-2.99E-12	-1.59E-02	-5.17E-14	-6.25E-02	3.74E-13	1	5.60E-13
$C_v^{(m;6,3)}$	-9.92E-16	5.35E-03	-1.20E-14	-7.03E-03	-1.86E-13	2.80E-03	-9.32E-15	-1.68E-02	-5.11E-15	7.45E-02	-3.61E-14	-3.10E-02	-9.20E-15	1.51E-02	1.46E-13	9.40E-02	5.49E-13	-1
$C_u^{(m;1,1)}$	1.17E-15	-2.66E-02	-3.84E-15	3.90E-03	1.61E-14	7.03E-04	-1.17E-15	1.91E-01	1.16E-13	-1.28E-01	-1.45E-12	-1.40E-01	1.50E-14	1.61E-01	-1.23E-13	5.59E-02	3.87E-15	1.69E-02
$C_u^{(m;2,1)}$	-4.69E-16	1.22E-02	2.94E-15	-2.49E-03	-1.05E-14	-6.78E-04	2.08E-15	-2.98E-02	-2.11E-14	1.15E-02	4.77E-14	-5.17E-03	1.01E-15	2.83E-02	3.50E-14	5.67E-02	2.43E-14	4.54E-02
$C_u^{(m;3,1)}$	-1.46E-15	-5.26E-02	-1.13E-14	-1.88E-02	-1.18E-13	1.79E-03	-6.42E-15	3.66E-01	2.79E-13	2.66E-01	1.97E-12	1.02E-01	1.48E-14	2.65E-01	8.20E-14	-4.18E-01	1.59E-13	-8.37E-02
$C_u^{(m;4,1)}$	8.52E-16	2.59E-02	1.46E-15	1.28E-02	7.40E-14	2.01E-03	3.44E-15	-7.47E-02	-5.57E-14	-6.27E-02	-1.04E-13	5.40E-03	7.66E-16	3.89E-02	8.31E-14	-3.23E-01	1.78E-13	-1.61E-01
$C_u^{(m;5,1)}$	-1.84E-15	1.24E-02	-2.89E-15	-2.66E-02	-1.73E-13	4.64E-04	-2.83E-15	-7.86E-02	4.62E-14	5.02E-01	-5.50E-13	-1.99E-01	-3.81E-15	-5.71E-02	1.02E-13	-7.16E-01	1.42E-13	1.19E-01
$C_u^{(m;6,1)}$	9.18E-16	-6.62E-03	1.36E-14	1.97E-02	1.31E-13	-6.83E-03	4.68E-16	1.47E-02	-2.37E-14	-1.21E-01	-2.58E-13	6.68E-03	3.65E-15	-1.74E-02	1.45E-13	-3.77E-01	1.19E-13	2.10E-01
$C_u^{(m;1,2)}$	6.44E-02	-6.84E-16	-3.05E-02	-1.51E-14	1.29E-03	-9.34E-14	1.67E-01	-8.22E-14	3.42E-01	-3.51E-13	1.11E-01	4.10E-12	-9.76E-02	-3.33E-14	-4.90E-01	-3.26E-13	-6.51E-02	-3.41E-14
$C_u^{(m;2,2)}$	-3.25E-02	7.07E-16	1.65E-02	2.30E-14	-4.10E-03	4.64E-14	5.00E-03	5.66E-15	-5.24E-02	8.42E-15	-7.41E-04	-7.26E-14	1.41E-01	-1.45E-14	-2.52E-01	-1.15E-13	-8.21E-02	-1.50E-13
$C_u^{(m;3,2)}$	-1.63E-02	6.99E-15	-4.48E-02	4.72E-14	-7.95E-03	-1.16E-13	-4.68E-02	-1.57E-13	5.22E-01	1.69E-13	-2.49E-01	1.13E-11	4.97E-03	4.69E-14	-8.98E-01	-3.94E-14	2.09E-01	-4.04E-15
$C_u^{(m;4,2)}$	1.01E-02	-4.37E-15	2.31E-02	-5.47E-14	1.01E-02	6.36E-14	-4.48E-03	4.46E-14	-1.32E-01	2.71E-15	2.22E-02	-9.47E-13	-4.62E-02	7.62E-15	-3.45E-01	6.20E-14	2.56E-01	-8.36E-15
$C_u^{(m;5,2)}$	9.03E-03	-1.10E-15	1.29E-02	4.44E-14	-9.52E-03	2.60E-14	2.70E-02	3.79E-14	-1.27E-01	5.10E-13	-3.13E-01	3.36E-12	-2.74E-03	8.52E-14	4.48E-01	2.57E-13	3.96E-01	1.33E-13
$C_u^{(m;6,2)}$	-5.90E-03	-4.70E-17	-6.77E-03	-5.65E-14	1.15E-02	-6.56E-15	1.40E-03	-1.73E-14	4.16E-02	-1.07E-13	6.03E-02	-5.81E-13	2.70E-02	-2.55E-14	8.08E-02	7.31E-14	2.89E-01	1.33E-13
$C_u^{(m;1,3)}$	2.19E-16	-5.88E-03	-9.78E-16	1.15E-03	5.54E-15	1.67E-04	-1.14E-15	6.81E-03	7.66E-16	-4.06E-03	-5.66E-14	-3.07E-03	-2.53E-15	-3.48E-02	4.33E-14	-4.95E-03	6.06E-14	8.24E-04
$C_u^{(m;2,3)}$	-1.83E-16	4.81E-03	1.28E-15	-1.23E-03	-5.50E-15	-2.63E-04	5.29E-16	3.08E-03	-1.36E-15	5.91E-04	2.73E-14	3.21E-04	1.52E-15	3.74E-02	-1.71E-14	7.84E-03	4.20E-14	6.20E-03
$C_u^{(m;3,3)}$	-1.61E-17	-1.21E-02	-3.02E-16	-6.13E-03	-3.57E-14	-1.32E-03	-2.82E-15	1.67E-02	1.35E-14	3.66E-02	1.65E-13	7.96E-03	-3.02E-15	-6.38E-02	-1.34E-14	3.22E-02	5.55E-15	-3.67E-03
$C_u^{(m;4,3)}$	3.73E-16	1.02E-02	-6.51E-16	6.42E-03	3.58E-14	1.70E-03	2.48E-15	-7.97E-04	-2.77E-15	-3.42E-02	-1.72E-13	-9.41E-03	3.31E-15	6.48E-02	7.58E-15	-3.53E-02	3.66E-14	-1.59E-02
$C_u^{(m;5,3)}$	-5.39E-16	3.11E-03	-6.95E-15	-9.47E-03	-5.93E-14	3.67E-03	5.83E-16	1.32E-03	1.20E-14	4.46E-02	-2.32E-15	-7.91E-03	-1.41E-16	2.90E-02	-1.82E-14	7.99E-02	1.67E-14	-4.05E-03
$C_u^{(m;6,3)}$	4.94E-16	-2.63E-03	8.22E-15	9.96E-03	6.46E-14	-4.29E-03	-6.19E-16	-4.87E-03	-1.74E-14	-4.43E-02	4.26E-14	1.16E-02	-6.35E-16	-2.76E-02	-2.85E-15	-4.60E-02	-1.82E-14	3.19E-02
$C_u^{(m;1,4)}$	1.16E-02	-1.48E-16	-7.29E-03	-1.03E-14	1.94E-03	-1.98E-14	-1.96E-02	-2.17E-15	2.12E-02	-2.09E-14	7.02E-03	-2.01E-13	-5.52E-02	2.77E-15	5.27E-04	6.18E-17	2.60E-04	-3.85E-14
$C_u^{(m;2,4)}$	-3.16E-03	-3.08E-16	5.34E-03	7.40E-15	-1.46E-03	1.28E-14	1.36E-02	3.12E-15	-8.86E-03	1.70E-14	-9.67E-03	5.43E-13	-5.07E-03	1.15E-15	1.10E-02	-1.37E-15	-1.09E-02	-6.48E-15
$C_u^{(m;3,4)}$	-3.57E-03	2.02E-15	-1.01E-02	2.60E-14	-4.88E-03	-2.79E-14	9.36E-03	-1.55E-14	4.22E-02	1.68E-14	-1.38E-02	-3.55E-14	1.97E-02	2.20E-15	2.97E-02	-2.20E-15	-2.41E-02	1.00E-14
$C_u^{(m;4,4)}$	1.05E-03	-1.71E-15	9.15E-03	-2.83E-14	5.35E-03	2.63E-14	-4.95E-03	4.36E-15	-1.76E-02	-3.11E-14	1.78E-02	3.19E-13	1.61E-03	-3.18E-15	1.89E-02	2.63E-14	4.69E-02	1.09E-14
$C_u^{(m;5,4)}$	1.96E-03	2.95E-16	2.91E-03	3.06E-14	-6.13E-03	2.01E-15	-6.30E-03	2.63E-15	-9.69E-03	4.25E-14	-2.50E-02	3.97E-13	-1.22E-02	1.05E-14	-2.26E-02	-7.16E-14	-6.14E-02	4.06E-14
$C_u^{(m;6,4)}$	-1.31E-04	-4.97E-16	-2.43E-03	-3.60E-14	7.19E-03	-5.06E-16	3.35E-03	6.89E-16	-2.86E-04	-5.37E-14	3.23E-02	-6.46E-13	-2.59E-03	-7.10E-15	-1.57E-02	4.47E-14	4.75E-02	-2.49E-15

Table A.2: Trial function constants for medium detachment size: $R_0 - R_d = 0.236$.

	Mode Number																	
Constant	1	2	3	4	5	6	7	8	9	10	11	12	13	14	15	16	17	18
$C_v^{(m;1,1)}$	1	2.68E-14	2.32E-02	2.11E-13	6.61E-03	6.39E-15	4.22E-02	8.92E-15	-2.95E-03	1.99E-15	2.76E-03	5.03E-14	-2.02E-03	-1.75E-14	-3.18E-03	1.45E-16	-2.78E-03	2.71E-15
$C_v^{(m;2,1)}$	1.32E-14	-1	1.47E-13	3.78E-02	-1.45E-13	1.84E-02	-1.83E-15	-3.53E-02	-1.12E-14	1.43E-03	-9.94E-15	-2.98E-03	3.71E-14	-2.20E-02	-2.44E-14	8.75E-04	8.43E-14	-1.84E-03
$C_v^{(m;3,1)}$	2.32E-02	-1.10E-13	-1	1.44E-13	-3.45E-02	4.25E-13	4.23E-03	-1.06E-14	-1.64E-02	2.34E-14	-5.32E-04	2.14E-14	1.22E-03	2.10E-15	-1.16E-02	4.79E-15	3.77E-04	2.07E-14
$C_v^{(m;4,1)}$	9.39E-14	-3.88E-02	-1.89E-13	-1	1.42E-12	-6.81E-02	-1.23E-15	-3.88E-03	6.46E-17	7.14E-03	-2.10E-14	4.35E-04	-1.58E-14	-1.96E-03	4.21E-14	5.59E-03	5.40E-15	5.99E-04
$C_v^{(m;5,1)}$	-5.81E-03	-7.40E-14	-3.47E-02	1.39E-12	1	-1.78E-13	-2.74E-04	1.11E-15	-1.37E-03	1.43E-14	-2.05E-03	-4.50E-15	-1.97E-03	1.88E-14	-9.03E-04	4.24E-15	2.39E-03	2.29E-14
$C_v^{(m;6,1)}$	-1.85E-15	1.57E-02	3.30E-13	-6.88E-02	2.86E-13	1	5.04E-16	9.01E-04	-1.95E-15	2.71E-04	-4.04E-16	-6.46E-04	3.28E-15	4.65E-05	-1.33E-14	4.83E-04	2.04E-14	1.11E-04
$C_v^{(m;1,2)}$	3.73E-02	-1.57E-15	-2.47E-03	6.37E-15	-3.43E-04	1.33E-15	-1	1.45E-13	-3.60E-02	1.48E-13	3.14E-02	3.33E-13	-8.84E-02	5.64E-14	-1.61E-02	3.22E-13	-1.33E-02	-1.22E-13
$C_v^{(m;2,2)}$	-2.13E-16	-2.83E-02	2.58E-15	-1.74E-03	4.77E-16	-7.56E-04	7.65E-14	1	-3.65E-14	6.89E-02	1.87E-13	-8.55E-02	2.55E-13	-1.80E-01	-7.58E-14	5.65E-03	-1.44E-13	-1.04E-02
$C_v^{(m;3,2)}$	4.06E-03	-2.18E-15	-1.41E-02	4.56E-15	5.79E-04	5.80E-15	-3.35E-02	4.57E-14	1	-6.32E-14	-1.04E-01	-1.02E-13	-1.66E-02	-7.80E-14	-9.95E-02	-9.95E-14	3.00E-03	4.32E-14
$C_v^{(m;4,2)}$	4.15E-15	-3.79E-03	-1.74E-15	-6.26E-03	6.26E-15	1.16E-04	-4.15E-14	7.73E-02	-8.97E-14	-1	-5.00E-13	2.00E-01	-1.14E-13	-3.51E-02	1.06E-13	6.07E-02	3.15E-13	5.79E-03
$C_v^{(m;5,2)}$	-2.64E-03	-9.79E-16	-1.82E-03	1.29E-15	2.26E-03	2.18E-16	2.13E-02	-9.45E-14	1.02E-01	-4.07E-13	1	5.84E-13	4.03E-02	-1.69E-14	-1.94E-02	1.72E-13	4.03E-02	3.44E-14
$C_v^{(m;6,2)}$	2.40E-15	3.53E-03	-2.49E-15	-1.56E-03	1.74E-14	-3.95E-04	-2.11E-13	-6.26E-02	-5.26E-14	-2.03E-01	4.39E-13	-1	7.39E-13	3.83E-02	2.80E-14	2.30E-02	-5.53E-14	9.18E-03
$C_v^{(m;1,3)}$	1.29E-03	1.61E-15	9.82E-04	1.38E-15	1.67E-03	-1.19E-15	-6.76E-02	-1.01E-13	6.12E-03	4.08E-14	-3.51E-02	7.03E-13	1	2.60E-13	-9.67E-03	5.25E-14	-6.85E-03	1.56E-14
$C_v^{(m;2,3)}$	1.33E-15	-1.93E-02	1.92E-15	-1.15E-03	-1.49E-15	-4.44E-04	5.26E-15	1.33E-01	2.43E-14	-8.16E-03	6.86E-15	2.11E-02	-1.41E-13	1	-1.60E-13	5.78E-02	-2.88E-14	-7.26E-02
$C_v^{(m;3,3)}$	2.56E-03	-1.75E-15	-9.62E-03	4.05E-15	5.17E-04	4.37E-15	-1.05E-02	3.92E-14	6.94E-02	4.43E-14	3.26E-03	3.67E-16	-1.74E-03	1.45E-13	1	-6.46E-14	9.34E-02	1.05E-13
$C_v^{(m;4,3)}$	7.37E-16	-2.43E-03	-4.32E-16	-4.71E-03	6.57E-15	4.60E-04	-6.98E-14	1.52E-02	-3.32E-14	-4.04E-02	6.03E-14	-4.51E-03	1.73E-14	5.89E-02	-2.40E-14	-1	-5.62E-13	2.05E-01
$C_v^{(m;5,3)}$	-1.51E-03	-1.80E-15	-1.29E-03	3.30E-15	2.49E-03	6.32E-16	5.81E-03	-4.53E-14	1.07E-02	-1.10E-13	2.50E-02	5.64E-14	2.41E-03	-9.73E-14	8.70E-02	2.97E-13	-1	-1.38E-12
$C_v^{(m;6,3)}$	4.00E-16	2.35E-03	-8.12E-16	-1.43E-03	2.93E-15	4.10E-04	1.48E-15	-1.34E-02	2.12E-15	-1.29E-02	1.07E-16	-5.56E-03	2.32E-14	-5.21E-02	-1.98E-14	-2.03E-01	1.24E-12	-1
$C_u^{(m;1,1)}$	2.01E-16	-9.62E-03	1.19E-15	2.44E-04	-1.23E-15	-3.32E-04	1.31E-15	6.72E-02	1.09E-15	1.33E-02	2.00E-14	-1.05E-02	1.17E-14	1.50E-01	-5.51E-14	4.03E-02	-2.35E-14	-5.14E-02
$C_u^{(m;2,1)}$	-2.69E-02	1.25E-16	4.62E-03	-7.45E-15	-8.11E-04	-1.58E-15	1.34E-01	-1.32E-14	-6.04E-02	-3.53E-14	2.34E-02	-1.48E-13	-1.53E-01	-9.83E-14	-1.35E-01	-1.09E-13	-4.27E-02	-1.59E-14
$C_u^{(m;3,1)}$	4.14E-16	-1.70E-02	2.74E-15	-8.49E-04	-1.11E-15	1.49E-03	5.21E-15	1.21E-01	-7.74E-15	-5.64E-02	-1.61E-14	2.66E-02	-2.19E-14	2.42E-01	-7.88E-14	-9.90E-02	-1.27E-13	2.84E-02
$C_u^{(m;4,1)}$	9.41E-03	8.02E-16	7.01E-03	3.91E-15	2.49E-03	-3.34E-15	-4.56E-02	4.20E-15	-9.31E-02	4.10E-14	-5.79E-02	2.50E-14	5.25E-02	3.59E-14	-1.78E-01	1.79E-14	8.48E-02	1.20E-13
$C_u^{(m;5,1)}$	3.63E-16	5.87E-03	-3.48E-15	-1.21E-03	2.26E-15	-4.96E-03	-2.13E-14	-3.84E-02	-1.20E-14	-8.89E-02	-1.05E-14	-4.92E-02	4.20E-14	-7.66E-02	3.43E-14	-1.52E-01	8.44E-14	-5.41E-02
$C_u^{(m;6,1)}$	-5.26E-03	3.88E-16	-2.48E-03	2.48E-15	2.11E-03	5.47E-16	2.39E-02	7.71E-15	2.20E-02	2.79E-14	-7.02E-02	-7.49E-14	-3.20E-02	-1.39E-14	4.78E-02	-7.84E-14	1.12E-01	1.82E-13
$C_u^{(m;1,2)}$	4.90E-17	5.18E-03	-8.36E-16	-6.68E-04	1.41E-15	-2.60E-04	-2.50E-15	-1.67E-02	-1.21E-15	-1.02E-03	-1.32E-15	-4.61E-04	4.76E-15	-3.17E-02	2.74E-15	-6.49E-03	-1.06E-14	3.57E-03
$C_u^{(m;2,2)}$	9.80E-03	-3.33E-16	-4.40E-03	1.80E-15	-7.87E-04	2.26E-15	-2.15E-02	8.16E-15	9.49E-03	3.49E-15	1.87E-03	-1.64E-14	-3.59E-02	-9.77E-15	3.84E-02	-1.40E-14	1.28E-02	1.83E-14
$C_u^{(m;3,2)}$	-5.88E-16	9.73E-03	-4.39E-16	3.47E-03	-3.70E-15	7.55E-04	1.20E-15	-3.29E-02	5.78E-16	3.52E-03	-7.08E-15	2.18E-03	1.90E-15	-6.71E-02	9.56E-15	3.65E-02	4.22E-14	-1.62E-02
$C_u^{(m;4,2)}$	-3.67E-03	-1.17E-15	-6.60E-03	4.19E-15	2.79E-03	2.19E-15	8.55E-03	-1.16E-15	1.79E-02	-3.53E-15	-2.41E-03	4.39E-15	1.16E-02	8.78E-15	6.50E-02	5.79E-15	-4.09E-02	-5.62E-14
$C_u^{(m;5,2)}$	-3.84E-16	-3.56E-03	7.74E-16	4.81E-03	-7.58E-15	-1.94E-03	4.19E-15	1.26E-02	2.30E-15	8.37E-03	4.05E-15	-5.91E-03	1.11E-15	2.71E-02	-4.87E-15	7.04E-02	-3.06E-14	3.57E-02
$C_u^{(m;6,2)}$	2.36E-03	1.17E-16	2.28E-03	4.77E-15	3.35E-03	-1.53E-15	-5.94E-03	-2.05E-15	-7.12E-03	-5.91E-15	3.55E-03	3.14E-15	-5.73E-03	-1.17E-14	-1.98E-02	1.97E-14	-6.03E-02	-8.47E-14
$C_u^{(m;1,3)}$	-1.22E-16	-2.37E-03	4.44E-16	3.17E-04	-7.55E-16	1.13E-04	6.01E-16	8.95E-03	-2.16E-16	1.63E-03	2.88E-15	-1.16E-03	-1.15E-15	9.98E-03	-3.02E-15	1.62E-03	-4.12E-15	-1.22E-03
$C_u^{(m;2,3)}$	-3.45E-03	2.18E-16	2.14E-03	-5.94E-16	4.00E-04	-1.06E-15	3.29E-03	-6.25E-15	-8.27E-03	-4.01E-16	1.00E-03	2.35E-14	3.46E-02	3.96E-16	-9.34E-03	-2.94E-15	-7.91E-04	3.49E-15
$C_u^{(m;3,3)}$	3.59E-16	-4.41E-03	9.93E-17	-1.69E-03	2.00E-15	-3.59E-04	8.44E-16	1.65E-02	-7.73E-16	-6.46E-03	-1.90E-15	2.25E-03	-1.26E-15	1.62E-02	-3.17E-15	-2.61E-03	2.42E-15	-2.44E-03
$C_u^{(m;4,3)}$	1.18E-03	4.84E-16	3.25E-03	-2.42E-15	-1.44E-03	-1.06E-15	-4.62E-04	1.24E-15	-1.27E-02	2.17E-15	-4.67E-03	-1.20E-14	-1.44E-02	-5.04E-15	-1.18E-02	4.01E-16	-2.92E-03	-4.91E-15
$C_u^{(m;5,3)}$	2.21E-16	1.60E-03	-1.78E-16	-2.56E-03	4.18E-15	1.14E-03	-2.41E-15	-5.51E-03	-1.19E-15	-1.02E-02	-2.77E-15	-3.21E-03	2.85E-15	-5.51E-03	2.42E-15	-3.82E-03	-6.16E-15	7.58E-03
$C_u^{(m;6,3)}$	-7.33E-04	6.44E-17	-1.19E-03	-2.66E-15	-2.00E-03	8.65E-16	1.69E-05	3.93E-16	3.80E-03	2.83E-15	-7.49E-03	2.08E-15	9.21E-03	4.98E-15	4.84E-03	-3.26E-15	-4.91E-04	-1.97E-16
$C_u^{(m;1,4)}$	-4.94E-17	2.12E-03	-4.28E-16	-3.87E-04	6.85E-16	-1.56E-04	-5.13E-16	-6.46E-03	-2.57E-16	-1.35E-03	-1.55E-15	8.15E-04	-1.17E-15	-5.31E-03	1.52E-15	-2.27E-03	-1.45E-15	1.47E-03
$C_u^{(m;2,4)}$	2.28E-03	-2.05E-16	-2.37E-03	2.65E-16	-4.97E-04	1.11E-15	-6.21E-04	2.74E-15	7.71E-03	4.23E-16	-1.28E-03	-1.32E-14	-1.79E-02	-4.97E-15	1.32E-02	-4.98E-15	4.19E-03	6.23E-15
$C_u^{(m;3,4)}$	-2.18E-16	4.00E-03	-5.61E-17	2.06E-03	-2.36E-15	5.00E-04	1.94E-16	-1.29E-02	1.43E-15	6.25E-03	3.06E-16	-1.79E-03	3.91E-17	-1.12E-02	3.99E-15	1.24E-02	1.47E-14	-5.00E-03
$C_u^{(m;4,4)}$	-7.57E-04	-5.80E-16	-3.52E-03	2.95E-15	1.82E-03	1.12E-15	-1.07E-04	-7.64E-16	1.25E-02	-3.09E-15	4.88E-03	7.49E-15	6.81E-03	2.20E-15	2.03E-02	2.93E-15	-1.11E-02	-1.53E-14
$C_u^{(m;5,4)}$	-2.93E-16	-1.41E-03	1.88E-16	2.94E-03	-4.76E-15	-1.43E-03	2.94E-15	4.41E-03	1.66E-15	1.10E-02	1.98E-15	3.27E-03	-2.51E-15	4.04E-03	-1.83E-15	2.04E-02	-7.63E-15	7.67E-03
$C_u^{(m;6,4)}$	4.50E-04	-3.11E-17	1.20E-03	3.01E-15	2.29E-03	-9.27E-16	2.14E-04	-2.91E-16	-3.73E-03	-5.43E-15	8.47E-03	3.29E-15	-3.74E-03	2.05E-15	-6.21E-03	3.74E-15	-1.61E-02	-2.16E-14

Table A.3: Trial function constants for large detachment size: $R_0 - R_d = 0.436$.